

KATHOLIEKE UNIVERSITEIT LEUVEN
FACULTEIT TOEGEPASTE WETENSCHAPPEN
DEPARTEMENT ELEKTROTECHNIEK
Kasteelpark Arenberg 10, 3001 Leuven (Heverlee)

ANALYSIS AND IMPROVEMENT OF QUANTIFICATION ALGORITHMS FOR MAGNETIC RESONANCE SPECTROSCOPY

Promotoren:
Prof. dr. ir. S. Van Huffel
Prof. dr. P. Van Hecke

Proefschrift voorgedragen tot
het behalen van het doctoraat
in de toegepaste wetenschappen

door

Pieter PELS

Januari 2005



KATHOLIEKE UNIVERSITEIT LEUVEN
FACULTEIT TOEGEPASTE WETENSCHAPPEN
DEPARTEMENT ELEKTROTECHNIEK
Kasteelpark Arenberg 10, 3001 Leuven (Heverlee)

ANALYSIS AND IMPROVEMENT OF QUANTIFICATION ALGORITHMS FOR MAGNETIC RESONANCE SPECTROSCOPY

Jury:
Prof. dr. ir. L. Froyen, voorzitter
Prof. dr. ir. S. Van Huffel, promotor
Prof. dr. P. Van Hecke, co-promotor (Faculteit Geneeskunde)
Prof. dr. L. Buydens (RU Nijmegen)
Prof. dr. R. Oyen (Faculteit Geneeskunde)
Prof. dr. ir. R. Pintelon (ELEC, VUB)
Prof. dr. ir. D. Vandermeulen
Prof. dr. ir. J. Vandewalle

Proefschrift voorgedragen tot
het behalen van het doctoraat
in de toegepaste wetenschappen

door

Pieter PELS

U.D.C. 543.422.25 Januari 2005

© Katholieke Universiteit Leuven – Faculteit Toegepaste Wetenschappen
Arenbergkasteel, B-3001 Heverlee (Belgium)

Alle rechten voorbehouden. Niets uit deze uitgave mag vermenigvuldigd en/of openbaar gemaakt worden door middel van druk, fotocopie, microfilm, elektronisch of op welke andere wijze ook zonder voorafgaande schriftelijke toestemming van de uitgever.

All rights reserved. No part of the publication may be reproduced in any form by print, photoprint, microfilm or any other means without written permission from the publisher.

D/2005/7515/9

ISBN 90-5682-575-5

Voorwoord

Aan het einde van mijn doctoraat, en aan het begin van dit doctoraatsproefschrift zou ik graag de mensen bedanken die het mogelijk gemaakt hebben dit werk te presenteren.

Sabine, als promotor van mijn doctoraat zou ik je willen bedanken om mij de kans te geven in de Biomed onderzoeksgroep mijn doctoraat voor te bereiden. Gedurende deze periode bleef je mij steunen, ook in donkere dagen van wetenschappelijk onderzoek. Paul, als co-promotor heb ik veel geleerd van je ervaren, nuchtere kijk op de dingen en ik vond je energie dikwijls begeesterend. Ook als er weer eens een dataset nodig was kon je die steeds bezorgen. Bedankt.

De juryleden prof. dr. ir. L. Froyen (KUL), prof. dr. L. Buydens (Radboud Universiteit Nijmegen), prof. dr. R. Oyen (KUL), prof. dr. ir. R. Pintelon (ELEC, VUB), prof. dr. ir. D. Vandermeulen (KUL) en prof. dr. ir. J. Vandewalle (KUL) wil ik bedanken voor het beoordelen van mijn manuscript en voor de gegeven tips en suggesties.

Ik zou graag prof. dr. Oyen bedanken voor de mogelijkheid om prostaatspectroscopie in een klinische omgeving in de praktijk te testen.

Wie een nieuwe wereld verkent, heeft ervaren gidsen nodig. Ik zou daarom Leentje Vanhamme en René in't Zandt willen bedanken, die me elk introduceerden in een ander aspect van spectroscopie. Leentje stond altijd klaar wanneer ik vragen had over signalen, filters en algoritmes en ik ben niet vergeten hoe we uren zochten naar fouten in de algoritmes. René heeft me de weg gewezen in de verschillende aspecten van de werking van de MR scanner en de verschillende valkuilen die daarbij te pas komen. Een deel van mijn werk heb ik ook aan jouw voorbereidende werk te danken. Bedankt.

I want to thank everybody at the Radiology department of the University of California, San Francisco for our fruitfull collaboration. Esin Ozturk, it was really a pleasure working with you. Sarah Nelson, John Kurhanewicz and Mark Swanson, thank you for making it possible to stay in your group for 2 months. I am looking forward to work together again when I will join your group as a

post-doctoral researcher.

Dank aan Diana Sima en Bart De Neuter voor de productieve samenwerking bij verschillende projecten.

Zonder geld geen brood op de plank (en ook geen wetenschappelijk onderzoek). Ik zou daarom graag het Instituut voor de aanmoediging van Innovatie door Wetenschap en Technologie in Vlaanderen (IWT-Vlaanderen) willen danken voor de financiële ondersteuning.

Naast de vele wetenschappelijke discussies waren mijn collega's van de Biomed groep een onuitputbare bron van technische adviezen, administratieve weetjes en collegialiteit. Speciaal zou ik mijn verschillende bureau-genoten willen vermelden door wie er steeds in een gezellige sfeer kon gewerkt worden: René, Leen, Philippe, Geert, Wim, Jean-Michel, Andy, Arjan, Bart en Teresa. Daarnaast werden dankzij Ida, Lut en Ilse alle administratieve en financiële zaken vlot afgehandeld. Jullie werk wordt ten zeerste gewaardeerd.

Dat doctoreren op bepaalde momenten belastend kan zijn, zullen weinigen ontkennen. Het is daarom ook dat ik hier alle mensen die mij naast het doctoraat hielpen ontspannen zou willen bedanken: alle leden van de fritclub, de sportievelingen van KMNS Footbalos en al mijn andere vrienden en vriendinnen, bedankt voor al die memorabele momenten!

Als laatste zou ik mijn ouders en zus willen bedanken. Jullie zijn het in de eerste plaats die ervoor gezorgd hebben dat ik sta waar ik nu sta. Bedankt voor alle wijze raad, motiverende woorden en onvoorwaardelijke steun.

Abstract

Magnetic Resonance Spectroscopy (MRS) is a technique used in fundamental research and in clinical environments. During recent years, clinical application of MRS gained importance, especially as a non-invasive tool for diagnosis and therapy monitoring of brain and prostate tumours. The most important asset of MRS is its ability to determine the concentration of chemical substances non-invasively. To extract relevant signal parameters, MRS data have to be quantified. This usually doesn't prove to be straightforward since *in vivo* MRS signals are characterized by poor signal-to-noise ratios, overlapping peaks, acquisition related artefacts and the presence of disturbing components (e.g. residual water in proton spectra). The work presented in this thesis aims to improve the quantification in different applications of MRS *in vivo*.

To obtain the signal parameters related to MRS data, different approaches were suggested in the past. Black-box methods, don't require user interaction, but deliver statistically suboptimal parameter estimates. Interactive methods, such as AMARES, fit a model function to the MRS data by optimizing parameter estimates using a non-linear least squares minimization method. Incorporating information about mutual parameter relations (so called *prior knowledge*) results in more accurate parameter estimates. This principle, initially used to constrain parameters within the spectrum of one volume element (voxel), was extended to the quantification of multivoxel (CSI or MRSI) data, incorporating prior knowledge between different voxels. Multivoxel processing was shown to improve the parameter estimation, depending on the prior knowledge used. The need for automated processing protocols emerges, when large CSI datasets are to be processed. An aspect of automating CSI processing is the choice of the number of resonances to model. Because the number of spectral components can vary through a CSI, choosing a fixed number of resonances could introduce errors in the parameter estimation. By investigating the influence of under- and overmodeling, it was shown that only slight undermodeling had a negative effect on estimation accuracy.

MRSI can be used as diagnostic tool in prostate cancer. The performance of two quantification methods was compared in diagnosing prostate cancer. To

this end, simulated, *in vitro* and *in vivo* MRS prostate data were quantified in both time and frequency domain and the accuracy of the outcomes of both methods were compared. It was found that a Time Domain Fitting algorithm (based on AMARES) and a Frequency Domain Analysis method performed equally well, with a slightly better performance of the Time Domain Fitting algorithm on well resolved spectra.

A method optimized for the quantification of short echo time MRS data is presented. Short echo time spectra require a special approach to deal with the baseline and the high complexity of the spectral patterns. To use as much prior knowledge as possible, a database of measured metabolite model spectra is used. A two-step method is suggested which increases robustness of the quantification.

To bring advanced signal processing algorithms to the clinical environment, a GUI was developed to display both Magnetic Resonance Images and MRSI data. The GUI incorporated preprocessing and time domain quantification using AMARES.

Korte Inhoud

Magnetische Resonantie Spectroscopie (MRS) is een techniek die zowel in fundamenteel onderzoek als in een klinische omgeving gebruikt wordt. De laatste jaren wordt in de klinische omgeving meer en meer beroep gedaan op MRS, vooral als een niet-invasief hulpmiddel bij de diagnose en therapie opvolging van brein en prostaat tumoren. Het sterke punt van MRS is dat de techniek het mogelijk maakt concentraties van chemische stoffen in het lichaam te bepalen op een niet-invasieve wijze. Om de relevante signaal parameters te bepalen moeten de MRS data gekwantificeerd worden. Dit wordt echter bemoeilijkt door de aard van de *in vivo* MRS signalen: zij worden dikwijls gekenmerkt door lage signaal-ruis verhoudingen, overlappende pieken en artefacten gerelateerd aan de opname van de signalen. Daarbij komt nog dat dikwijls verstorende componenten aanwezig zijn (bvb. niet volledig onderdrukte waterresonanties bij proton spectra). Het werk gepresenteerd in deze thesis poogt de kwantificatie van *in vivo* MRS data in verschillende toepassingen te verbeteren.

Om de signaal parameters van een MRS signaal te bepalen werden in het verleden verschillende technieken voorgesteld. Zwarte-doos methodes vereisen geen interactie met de gebruiker maar leveren statistisch sub-optimale parameterschattingen. Interactieve methodes zoals AMARES modeleren het MRS signaal door een niet lineair kleinste kwadraten minimalisatieprobleem op te lossen. Het in rekening brengen van informatie over relaties tussen verschillende signaal parameters (voorkennis) leidt tot nauwkeurigere parameterschattingen. Dit principe, waarbij oorspronkelijk voorkennis opgelegd werd op parameters behorende tot het spectrum van 1 volume element (voxel), werd uitgebreid naar de kwantificatie van multivoxel (CSI of MRSI) data. Hierbij wordt voorkennis tussen parameters behorende bij spectra uit verschillende voxels opgelegd. Er werd aangetoond dat multivoxelverwerking nauwkeurigere parameter schattingen opleverde, afhankelijk van de gebruikte voorkennis. Wanneer grote CSI datasets verwerkt moeten worden is het nodig om de kwantificatie te automatiseren. Aangezien er een verschillend aantal pieken kan voorkomen in verschillende voxels, is het mogelijk dat de keuze om een constant aantal pieken te modelleren leidt tot fouten in de parameterschatting. De invloed van onder- en overmodellering werd onderzocht en er werd aangetoond dat enkel een lichte

ondermodellering een negatief effect op de nauwkeurigheid van de schatting tot gevolg had.

MRSI kan gebruikt worden om de diagnose van prostaat kanker te ondersteunen. Twee kwantificatie methodes werden vergeleken in hun nauwkeurigheid om prostaatkanker te voorspellen. Hiervoor werden gesimuleerde, *in vitro* en *in vivo* prostaat spectroscopie data gekwantificeerd met een Tijds Domein Fitting algoritme (TDF) en een Frequentie Domein Analyse algoritme (FDA). Beide methodes vertoonden een vergelijkbare nauwkeurigheid, met een iets betere performantie van de Tijds Domein Fitting methode wanneer goed gescheiden spectra geanalyseerd werden.

Een methode geoptimaliseerd voor de verwerking van korte echo tijd MRS data wordt voorgesteld. Korte echo tijd spectra vereisen een speciale aanpak in de kwantificatie door de aanwezigheid van een basislijn en door de complexe structuur van de spectra. Om zoveel mogelijk voorkennis te gebruiken tijdens de kwantificatie wordt gebruik gemaakt van een databank met opgemeten model spectra. Een twee-staps algoritme wordt voorgesteld dat leidt tot een verhoogde robuustheid van de kwantificatie.

Om geavanceerde signaalverwerkingsalgoritmes beschikbaar te maken in een klinische omgeving werd een Grafische Gebruikersinterface ontworpen waarmee MR beelden en MR spectroscopie data kunnen gevisualiseerd worden. De interface omvat verscheidene voorbewerkingsmethodes waaronder een water filter en het kwantificatie algoritme AMARES.

Glossary

Used Symbols and Notation

B_0	static magnetic field
B_{eff}	effective magnetic field
T_1	relaxation constant
T_2	relaxation constant
σ	shielding constant (Chapter 1)
a_k	amplitude of resonance k
d_k	damping of resonance k
f_k	frequency of resonance k
ϕ_k	phase of resonance k
$y(\cdot)$	measured data
$\overline{y}(\cdot)$	model function
t_n	n^{th} point of time vector
K	model order
$Re(\cdot)$	real part
$\boldsymbol{\alpha}$	parameter vector
c_k	complex amplitude of resonance k
$\boldsymbol{\Gamma}$	nonlinear part of model function
h_m	m^{th} FIR filter coefficient
M	FIR filter length
z_k	signal pole k
p_k	forward prediction coefficient k
$p(\cdot)$	polynomial function
$\mathbf{H}$	Hankel matrix
$\mathbf{H}_{\text{lp}}$	linear prediction Hankel matrix
S	number of signals in costfunction
$\boldsymbol{\theta}$	parameter vector
$\hat{\boldsymbol{\theta}}$	unbiased estimator of $\boldsymbol{\theta}$
$\mathbf{P}$	covariance matrix
$\mathbf{F}$	Fisher information matrix
$\mathbf{k}$	k-space vector

$\mathbf{x}$	x-space vector
$D_k(\cdot,\cdot)$	k-space representation of CSI
$D_x(\cdot,\cdot)$	x-space representation of CSI
$\mathbf{J}$	Jacobian matrix
b_l	coefficient of spline l
$B_l(\cdot)$	time domain representation of cubic spline l
D_p	difference operator of pth order
λ	regularization factor
M_k	model spectrum k
Δa_k	correction on amplitude of model spectrum k
Δd_k	correction on damping of model spectrum k
Δf_k	correction on frequency of model spectrum k
$\Delta \phi_k$	correction on phase of model spectrum k

Acronyms and Abbreviations

AMARES	Advanced Method for Accurate, Robust and Efficient Spectral fitting
AQSES	Accurate Quantification of Short Echo time Spectra
AQSES_4	AQSES using only 4 landmarks
ARMSE	Absolute Root Mean Square Error
ATP	Adenosine triphosphate
BASING	BAnd Selective INversion with Gradient dephasing
BPH	Benign Prostate Hyperplasia
CCP/C	(Creatine + Choline + Polyamines) / Citrate
CHESS	CHEmical Shift Selective
Cho	Choline
Cit	Citrate
CPU	Central Processing Unit
cc	cubical centimeter
Cr	Creatine
CR(B)	Cramer-Rao (Bound)
CSI	Chemical Shift Image
DFT	Discrete Fourier Transformation
ECC	Eddy Current Correction
FDA	Frequency Domain Analysis
FFT	Fast Fourier Transform
FID	Free Induction Decay
GABA	γ-aminobutyric acid
GAMMA	General Approach to Magnetic resonance Mathematical Analysis
GE	General Electric
GIF	Graphics Interchange Format

Gln	Glutamine
Glu	Glutamate
GUI	Graphical User Interface
H(L)SVD	Hankel (Lanczos) Singular Value Decomposition
HTLS	Hankel Total Least Squares
Ins	myo-Inositol
jMRUI	JAVA Magnetic Resonance User Interface
Lac	Lactate
LS	Least Squares
ML	Maximum Likelihood
MR	Magnetic Resonance
MRI	Magnetic Resonance Imaging
MRS	Magnetic Resonance Spectroscopy
MRSI	Magnetic Resonance Spectroscopic Imaging
NAA	N-acetyl-aspartate
NEX	Number of EXcitations
NLLS	Non Linear Least Squares
PIN	Prostatic Intraepithelial Neoplesia
PRESS	Point RESolved Spectroscopy
PRISMA	PRIor knowledge based modeling of Spectroscopic MAgnetic resonance applications
PSA	Prostate Specific Antigen
QUALITY	QUAntification improvement by converting LIneshapes to the Lorentzian TYpe
QUEST	QUantitation based on QUantum ESTimation
RF	Radio Frequent
RMSE	Root Mean Square Error
RRMSE	Relative Root Mean Square Error
SNR	Signal-to-Noise Ratio
STEAM	STimulated Echo Acquisition Mode
SVD	Singular Value Decomposition
SVS	Singel Voxel Spectroscopy
T	Tesla
TDF	Time Domain Fitting
TE	Echo Time
TR	Repetition Time
TRUS	Trans Rectal Ultra Sound
TSNR	Total Signal-to-Noise Ratio
UCSF	University of California, San Francisco
VARPRO	VARiable PROjection

Contents

Voorwoord **i**

Abstract **iii**

Korte Inhoud **v**

Glossary **vii**

Contents **xi**

Samenvatting **1**

1 Introduction **15**

1.1 Introducing Magnetic Resonance 15

1.1.1 Basic Principles 16

1.1.2 Magnetic Resonance Spectroscopic Imaging 18

1.2 Data Preprocessing 21

1.3 Data Quantification 24

1.3.1 Prior Knowledge 25

1.3.2 Frequency Domain Methods 28

1.3.3 Time Domain Methods 29

1.4 Relevance of MRS in clinical applications 38

1.4.1 Brain MRS 38
1.4.2 Prostate MRS 40
1.5 Chapter by chapter overview 42
1.6 Conclusion 43

2 Comparing Time Domain Fitting With Frequency Domain Analysis on prostate MRSI Data 45

2.1 Introduction 45
2.2 Methods 46
2.2.1 Simulations 46
2.2.2 Phantom and *in vivo* Data Acquisition 49
2.2.3 Phantom and *in vivo* MRSI data reconstruction 50
2.2.4 Time domain processing 50
2.2.5 Frequency Domain Analysis 53
2.3 Results 54
2.3.1 Simulations 54
2.3.2 Phantom 54
2.3.3 *In vivo* Data 57
2.3.4 Case study 58
2.4 Discussion 61
2.4.1 Simulations 61
2.4.2 Phantom data 61
2.4.3 *In vivo* data 62
2.4.4 Case Study 62
2.4.5 TDF versus FDA 62
2.5 Clinical Application 63
2.6 A JAVA GUI for prostate CSI processing 64

2.7 Conclusion 66

3 Multivoxel Time Domain Fitting **73**

3.1 Introduction 73

3.2 Extension of AMARES$_f$ to multivoxel processing 74

3.3 Cramér-Rao Bounds 75

3.3.1 Prior knowledge for multivoxel processing 76

3.4 Monte Carlo Simulations 78

3.4.1 Monte Carlo simulations of a brain CSI from a healthy volunteer 78

3.4.2 Monte Carlo simulations on a CSI from a brain tumour 80

3.5 Results 82

3.5.1 Multivoxel processing 82

3.5.2 Model Order 85

3.5.3 Controlled Monte Carlo experiment on the lactate-fat region 87

3.6 *In vivo* CSI 90

3.7 Discussion and Conclusion 91

4 Short Echo Time Quantification: a 2-step approach **95**

4.1 Introduction 95

4.1.1 Metabolite Quantification 96

4.1.2 Baseline 97

4.2 Methods 98

4.2.1 Short Echo Time Quantification Using AQSES 98

4.2.2 Acquisition of model spectra database 98

4.2.3 Quantification 100

4.2.4 Applying AQSES to simulated signals 103

4.2.5 Applying AQSES to *in vivo* signals 105
4.3 Results 106
4.3.1 Monte Carlo simulations I : 4 landmarks 106
4.3.2 Monte Carlo simulations II: frequency and damping shift 108
4.3.3 $AQSES_{2step}$ 109
4.3.4 Baseline Modeling: preliminary results 114
4.3.5 *In vivo* metabolite quantification 116
4.4 Conclusion 118

5 Conclusions and Further Research 121
5.1 Conclusions 121
5.2 Further Research 123

Bibliography 125

List of publications 137

Curriculum Vitae 141

Samenvatting

Analyse en verbetering van kwantificatie algoritmes voor magnetische resonantie spectroscopie

Hoofdstuk 1 : Inleiding

Magnetische Resonantie (MR) is een techniek die het mogelijk maakt om inwendige anatomische beelden te maken van het menselijk lichaam. Daarnaast is het mogelijk om met MR informatie te bekomen over de verdeling van bepaalde chemische stoffen (metabolieten) in het menselijk lichaam. Deze techniek wordt Magnetische Resonantie Spectroscopie genoemd.

Het principe van MR steunt op het feit dat elk atoom een bepaald magnetisch moment of *spin* heeft. Voor waterstof zijn er twee mogelijke toestanden: spin up en spin down. Wanneer een verzameling atomen (bvb. het menselijk lichaam) in een constant magnetisch veld B_0 wordt gebracht, dan zullen de spins van de atomen uitgelijnd worden: spin up zal zich richten volgens het magnetisch veld, terwijl spin down zich tegengesteld aan het magnetisch veld zal richten. Door een radiofrequent (RF) fluctuerend magnetisch veld aan te leggen zal het systeem van spins geëxciteerd worden. Wanneer het veld uitgeschakeld wordt zal het systeem relaxeren naar zijn evenwichtstoestand, waarbij magnetische golven worden uitgezonden met dezelfde frequentie als de golven gebruikt voor de excitatie. Deze magnetische golven kunnen gedetecteerd worden en genereren het MR signaal. Dit signaal wordt het Vrij Inductie Verval (VIV) genoemd

en wordt gekenmerkt door twee verschillende relaxatieconstanten: T_1 en T_2, dewelke de relaxatie karakteriseren volgens respectievelijk de richting van het statische magnetisch veld en volgens het veld loodrecht op B_0. De tijd die verloopt tussen de excitatie puls en het opmeten van de VIV wordt de echotijd genoemd (ET).

In het VIV zijn de verschillende metabolieten aanwezig met een verschillende frequentie, waardoor ze onderscheiden kunnen worden. Om een bepaald volume element of voxel te selecteren, wordt voor de excitatie een combinatie van andere RF pulsen toegevoegd zoals bijvoorbeeld de veel gebruikte PRESS en STEAM sequentie.

Twee verschillende types spectroscopie sequenties kunnen onderscheiden worden. Oorspronkelijk werd slechts uit 1 voxel een VIV opgemeten. Hiermee wordt echter geen informatie verkregen over de ruimtelijke verdeling van de metabolieten. Een methode die wel de mogelijkheid biedt om de ruimtelijke verdeling van de metabolieten op te meten is Magnetische Resonantie Spectroscopische Beeldvorming (MRSB). Deze sequentie meet een CSI (Chemical Shift Image) op, dewelke bestaat uit verschillende VIV's, gerangschikt in een rooster. Op deze wijze is het mogelijk de metabolische toestand op verschillende plaatsen te analyseren. Het rooster kan 2 of 3 dimensionaal zijn met typische dimensies 16×16 ($\times$ 16) of 32×32 ($\times$ 32). De data worden opgenomen in het tijdsdomein maar worden gevisualiseerd in het frequentiedomein na een Fourier Transformatie.

Om de relevante informatie uit de signalen de verkrijgen zijn twee verschillende stappen nodig: een voorverwerkingsstap en een kwantificatiestap. Tijdens de voorverwerking wordt het signaal ontdaan van alle storende componenten. Tijdens de kwantificatie worden de signaalparameters bepaald, waaronder de concentratie gerelateerde amplitude.

Voorverwerking

Met behulp van MRS is het mogelijk om de concentraties van verschillende stoffen te bepalen. Dit wordt echter dikwijls bemoeilijkt door de aanwezigheid van acquisitie gerelateerde artefacten en door de intrinsieke lage intensiteit van de metabolietsignalen. Daarom is voorverwerking van de data nodig. Verschillende voorverwerkingsmethodes trachten de data te bewerken zodat de kwantificatie nauwkeuriger wordt. De belangrijkste voorverwerkingsstap is het filteren van aanwezig water.

Het opgemeten metabolietsignaal is intrinsiek zwak, de concentraties van de metabolieten zijn immers tot 1000 keer kleiner dan de concentratie van water. Daarom is het noodzakelijk het watersignaal te onderdrukken tijdens de acquisitie of naderhand bij de voorverwerking het water weg te filteren. Tijdens de acquisitie kan gebruik gemaakt worden van bijvoorbeeld de water onder-

drukkende CHESS of BASING puls sequenties. Dikwijls is de onderdrukking tijdens de acquisitie echter niet voldoende om overblijvende water componenten te verwijderen. In een voorverwerkingsstap kunnen dan de resterende water componenten weggefilterd worden met een HSVD filter of door de toepassing van een FIR filter. Andere voorverwerkingsmethodes kunnen ofwel de resolutie, ofwel de signaal-ruis verhouding van de spectra opdrijven, maar dit slechts ten koste van elkaar. Verder is het mogelijk te corrigeren voor wervelstroom geïnduceerde faseverschuivingen of voor een verstoorde lijnvorm, maar dit enkel als een water signaal opgemeten werd. Bij signalen opgemeten met een korte echtotijd kan een basislijncorrectie nodig zijn. De basislijn is een onderliggende resonantie met een veel bredere piek dan de overige metabolieten en wordt veroorzaakt door macromoleculen met een grotere demping. Omdat de exacte bijdrage tot het spectrum niet bekend is, is het moeilijk om deze basislijn te verwijderen.

Kwantificatie

Met kwantificatie wordt het bepalen van de signaalparameters bedoeld. Het VIV signaal kan theoretisch gemodelleerd worden door een som van K exponentieel gedempte sinusoïden:

$$\bar{y}(t_n) = \sum_{k=1}^{K} a_k e^{j\phi_k} e^{(-d_k + j2\pi f_k)t_n}$$

waarbij a_k de amplitude is, f_k de frequentie, d_k de demping en ϕ_k de fase van de k^{de} spectrale component; t_n is de tijdsvector. Er wordt verondersteld dat de ruis aanwezig in de signalen witte circulaire ruis is.

In vivo data zijn dikwijls van lage kwaliteit, en vertonen dikwijls sterk overlappende pieken. Het is dan ook niet voor de hand liggend om de verschillende parameters te schatten. De schatting van de signaalparameters kan echter nauwkeuriger gemaakt worden wanneer gebruik gemaakt wordt van *voorkennis*. Bepaalde signaalparameters zijn immers gerelateerd: zo kan bijvoorbeeld met kwantum-mechanische berekeningen aangetoond worden dat voor sommige molecuulspectra amplitudes en dempingen gerelateerd zijn. Anderzijds kan ook verondersteld worden dat de dempingen van de verschillende metabolieten gelijk zijn, omdat ze zich in hetzelfde magnetische veld bevinden. Gebruik van voorkennis maakt de parameterschattingen nauwkeuriger.

De meest eenvoudige kwantificatiemethodes zijn niet-parametrisch. Dit wil zeggen dat er geen parametrisch model gebruikt word om de data te kwantificeren. In het frequentiedomein kan bijvoorbeeld een schatting van de amplitude van de verschillende metabolieten bekomen door de oppervlakte onder de piek te integreren. Langs de andere kant staan de parametrische methodes dewelke een geparametriseerde modelfunctie gebruiken om het spectrum te modelleren.

Om de modelparameters te bepalen wordt het verschil tussen de modelfunctie en het opgemeten signaal geminimaliseerd met behulp van een niet lineaire kleinste kwadraten algoritme. Een derde methode maakt gebruik van opgemeten model spectra om het opgemeten spectrum te benaderen als een lineaire combinatie van deze model spectra.

De kwantificatie kan gebeuren in het tijdsdomein of in het frequentiedomein.

In het tijdsdomein onderscheiden we twee klassen van kwantificatiemethoden: zwarte-doos methodes en interactieve methodes. De interactieve methodes minimaliseren het kwadratische verschil tussen modelfunctie en de data, en leiden tot een maximale waarschijnlijkheidsoplossing voor de modelparameters. Om het niet lineaire kleinste kwadratenprobleem op te lossen met behulp van variabele projectie functionaal wordt de modelfunctie opgesplitst in een lineair en niet lineair gedeelte. Eerst worden de niet lineaire parameters bepaald, waarna een oplossing voor de lineaire parameters wordt gezocht. Een dergelijk globaal optimalisatieprobleem convergeert niet noodzakelijk naar het globale minimum van de kostfunctie. Daarom worden startwaarden opgegeven, wat meteen ook verklaart waarom deze methodes *interactief* genoemd worden. Voor elk signaal is het immers nodig de startwaarden te bepalen. Oorspronkelijk werd het variabele projectie algoritme VARPRO gebruikt. Dit algoritme werd echter verder uitgebreid tot het AMARES algoritme, wat het mogelijk maakt voor de gebruiker om voorkennis mee te geven. De mogelijkheid om verschillende modelfuncties en uitgebreide voorkennis te gebruiken maakt de interactieve kwantificatiemethodes een aantrekkelijke keuze voor het kwantificeren van lage signaal-ruis spectra.

Een ander voordeel van AMARES is dat het op een handige manier kan gecombineerd worden met een FIR filter, dewelke residueel water wegfiltert. Het voordeel van de combinatie van AMARES met het FIR filter is dat de effecten van de filter op de metabolieten in rekening gebracht kunnen worden tijdens de kwantificatie. Wanneer AMARES en een FIR filter worden gecombineerd, dan wordt de volgende kostfunctie geminimaliseerd:

$$\sum_{n=1}^{N-M} \left| y_n^{fil} - \sum_{k=1}^{K} \bar{h} b_k x_k(n) \right|^2$$

hieruit blijkt dat de filtercoefficienten $\bar{h}$ en b_k mee opgenomen worden in de modelfunctie.

Naast de interactieve methodes bestaan ook de zwarte-doos methodes. Deze methodes vereisen geen gebruikersinteractie, wat meteen ook de naam verklaart. Voordeel van deze methodes is dat de resultaten gebruikersonafhankelijk zijn, een groot nadeel is echter dat er geen voorkennis kan opgelegd worden en dat de parameterschatttingen statistisch suboptimaal zijn. Twee zwarte

doos methodes zijn bijvoorbeeld lineaire predictie en deelruimte gebaseerde algoritmes.

MRS wordt in de klinische omgeving toegepast om het metabolisme te observeren op een niet-invasieve wijze. Afwijkingen van de normale metabole toestand wijzen doorgaans op pathologie. MRS van de hersenen wordt gebruikt voor de diagnose van hersentumoren, omdat elk type gekenmerkt wordt door een karakteristiek spectrum. Bij MRS van de hersenen wordt zowel gewerkt met korte als lange echtotijd spectra, waarbij korte echotijd spectra meer informatie bevatten, maar ook moeilijker te kwantificeren zijn. Met behulp van MRSB kan een een metabolietkaart aangemaakt worden dewelke de verdeling van de metabolieten visualiseert. Ook voor de diagnose van prostaatkanker wordt gebruikt gemaakt van MRS(B). Hiervoor wordt de verhouding van de verschillende metabolieten gebruikt als indicator voor de aard van het weefsel.

Hoofdstuk 2: Een vergelijking tussen Tijdsdomein fit algoritme en Frequentie Domein Analyse voor prostaat MRSB data

Omwille van de diagnostische waarde van MRS van de prostaat is het belangrijk optimale kwantificatie methodes te ontwikkelen. In dit hoofdstuk wordt een TijdsDomein modelgebaseerd Fit-algoritme (TDF) vergeleken met een Frequentie Domein Analyse algoritme (FDA), gebaseerd op een integratie in het frequentiedomein. De moeilijkheid bij de kwantificatie van prostaat data ligt in het feit dat de resonanties van creatine, polyamines en choline sterk overlappend zijn. De twee methodes worden vergeleken op het vlak van nauwkeurigheid in het schatten van de klinisch relevante verhouding van amplitudes van de aanwezige metabolieten.

Methodes

Om beide methodes te vergelijken wordt gebruik gemaakt van een Monte Carlosimulatie met gesimuleerde prostaatspectra en worden beide methodes toegepast op *in vitro* data en op *in vivo* data.

Data

Spectra afkomstig uit vijf verschillende weefsels werden gesimuleerd: fantoom oplossing, gezond weefsel, gemengd weefsel, tumor weefsel en agressief tumorweefsel. Citraat werd gemodeleerd door 2 centrale pieken en 2 kleinere zijpieken. Choline, creatine en polyamines werden gemodeleerd door 1 piek, waarbij de polyamines een grotere demping hadden: 8 Hz i.p.v. 2 Hz. Beide methodes werden toegepast en de nauwkeurigheid in het bepalen van de diagnostisch relevante verhouding van (choline+polyamines+creatine) tot citraat. Met behulp van Monte Carlo simulaties werd de relatieve gemiddelde fout, standaard afwijking en vertekening van de verschillende methodes geëvalueeerd voor de

vijf verschillende types spectra.

Een fantoomoplossing die de belangrijkste prostaat metabolieten bevat werd bereid. Van deze oplossing werd een CSI opgemeten, van waaruit 72 spectra werden geselecteerd. Analoog werden 72 spectra uit *in vivo* data geselecteerd. Al deze signalen werden met beide methodes gekwantificeerd en de resultaten werden vergeleken.

Tijdsdomein Fit Algoritme De TDF methode is gebaseerd op AMARES$_f$, waarin een FIR filter is ingebouwd. De meest optimale keuze van modelfunctie bevat geen polyamines. Omdat de polyamines een te grote overlap hebben met creatine en choline worden ze niet opgenomen in de modelfunctie. Het opnemen van de polyamines in de modelfunctie heeft een negatieve invloed op de schatting van de andere signaalparameters zoals ook wordt bevestigd door de berekening van de CR ondergrenzen. Zowel voor de verwerking van de simulatiesignalen als voor de fantoom en *in vivo* signalen werden geen polyamines opgenomen in de modelfunctie. Voor de verwerking van de gesimuleerde data wordt het citraat gemodelleerd met 4 pieken, met de gepaste voorkennis. Voor de fantoom en *in vivo* data werden de buitenste pieken niet opgenomen in de modelfunctie omdat zij niet zichtbaar zijn in het spectrum en dit de kwantificatie nodeloos zou bemoeilijken. De invloed van snel vervallende metabolieten als polyamines kan worden beperkt door de eerste datapunten te verwijderen. Er werd nagegaan wat de invloed hiervan was op de nauwkeurigheid van de parameterschattingen.

Frequentie Domein Analyse Deze methode bepaalt de amplitudes van de metabolieten door welbepaalde gebieden in het spectrum te integreren. De methode omhelst ook een frequentiecorrectie, een fasecorrectie en een automatische verwijdering van de mogelijk aanwezige basislijn. Omdat het voor deze methode onmogelijk is om onderscheid te maken tussen de overlappende pieken van choline, polyamines en creatine werd steeds de som van deze drie als geheel geschat. Omdat de beide methodes toch vergeleken werden in het schatten van de CCP/C verhouding leverde dit geen problemen op.

Resultaten

Met behulp van de gemiddelde fout en vertekening konden de prestaties van beide methodes vergeleken worden voor de 5 types gesimuleerde signalen. Ondanks het feit dat de TDF methode de polyamines niet meenam in de berekening van de CCP/C verhouding, was deze methode toch nauwkeuriger in het schatten van de CCP/C verhouding dan de FDA methode voor alle simulatiesignalen, behalve voor het normale spectrum omdat daar polyamines het sterkst aanwezig waren. De fout die gemaakt werd was voornamelijk te wijten aan een vertekening die voor de TDF methode kan verklaard worden door het ontbreken van de polyamines in de berekende CCP/C verhouding, en voor de FDA methode zou dit verklaard kunnen worden door het feit dat niet de gehele

piek geïntegreerd wordt. Het is ook mogelijk dat door de basislijncorrectie de amplitude van bepaalde pieken kan beïnvloed hebben. De invloed van de polyamines werd optimaal onderdrukt wanneer 9 datapunten verwijderd werden en leverde een verbetering van de relatieve gemiddelde fout op tot 7 %.

De resultaten voor de verwerking van de fantoomdata leverden de volgende correlaties tussen de amplitudeschattingen van beide methodes op: voor choline, creatine en citraat respectievelijk: 0.99, 0.89 en 0.97. De verwerking werd in dit geval wel bemoeilijkt door de aanwezigheid van acquisitie gerelateerde artefacten. In dit geval werd de verhouding CCP/C overschat door beide methoden. Zoals verwacht kon worden door de lagere kwaliteit van *in vivo* data liggen de correlaties hier lager. Voor de schatting van de amplitude van choline, creatine en citraat werden respectievelijk de volgende correlaties gevonden: 0.59, 0.51 en 0.94. Ongeacht het feit dat deze correlaties beduidend lager liggen dan voor de fantoomdata, toch leveren beide methodes vergelijkbare resultaten wanneer met de diagnostische betekenis van de berekende CCP/C verhouding bekijkt. In de klinische praktijk kan bijvoorbeeld een drempelwaarde voor de CCP/C verhouding bepaald worden, dewelke de tumorspectra onderscheidt van de gezonde spectra. Na onderzoek van de spectra van duizenden patienten komt de drempelwaarde van 0.86 voor de CCP/C verhouding als goede keuze naar voor. Beide methodes voorspellen nu een zelfde conditie in 94% van de gevallen, gebaseerd op de hiervoor vermelde drempelwaarde. Naar de diagnose toe zijn beide methodes dus vergelijkbaar.

Algemeen kunnen we besluiten dat beide methodes vergelijkbaar nauwkeurig zijn, maar dat de TDF methode iets nauwkeuriger is wanneer de spectra weinig afwijken van de gebruikte modelfunctie. Dit was het geval voor de simulatiesignalen waarbij enkel witte ruis werd toegevoegd. De TDF methode heeft als voordeel dat het mogelijk is afzonderlijke schattingen voor de amplitudes van creatine, polyamines en choline te bekomen. Anderzijds is de FDA methode minder gevoelig aan afwijkingen van de gekozen lijnvorm, wat de methode meer robuust maakt.

De klinische realiteit is echter veel gecompliceerder dan de hier voorgestelde classificatie met behulp van een drempelwaarde voor de CCP/C waarde. Een onderzoek van de prostaat met mogelijke aanwezigheid van tumor is niet welomlijnd, vermits ook andere pathologieën het metabole patroon kunnen wijzigen. Dikwijls is MRSB van de prostaat een laatste stap wanneer alle andere conventionele diagnosetechnieken geen uitsluitsel brengen over de diagnose. In dergelijke gevallen is de prostaat dikwijls vervuild door bloedingen als gevolg van biopsies, wat de kwaliteit van de spectra doet dalen.

Grafische JAVA gebruikersinterface voor prostaat CSI verwerking

Om spectroscopie deel te laten uitmaken van het klinische diagnostisch in-

strumentarium, is het noodzakelijk dat de opgemeten data eenvoudig kunnen verwerkt en gevisualiseerd worden. Heden ten dage ontbreekt het dikwijls nog aan dergelijke programma's. De standaard verwerkingspakketten die voorzien worden door scannerproducenten zijn dikwijls erg beperkt in voorverwerkings- en kwantificatiemogelijkheden. Daarom werd een grafische gebruikersinterface ontwikkeld dewelke de spectroscopie data kan visualiseren in combinatie met de opgemeten MR beelden. Op deze manier worden de verschillende spectra onmiddelijk ruimtelijk gelocaliseerd. Het programma omvat naast de mogelijkheid om CSI data in te lezen en te visualiseren ook de mogelijkheid tot voorverwerking en kwantificatie van de spectra. Als voorverwerkginsstappen werd de mogelijkheid tot waterfiltering met behulp van HLSVD ingebouwd, alsook de mogelijkheid om het CSI rooster te verschuiven in de ruimte om aldus een betere positionering van het rooster te bekomen. Als kwantificatie algoritme werd AMARES ingebouwd. De CSI wordt automatisch gekwantificeerd en de resultaten gevisualiseerd in een metabolietkaart, zodat een snelle interpretatie van de data mogelijk wordt.

Hoofdstuk 3: Multivoxel Tijdsdomein Fitten

Wanneer MRSB datasets verwerkt worden, moet plots een groot aantal spectra verwerkt worden (bvb. 1024 voor een 32×32 CSI). Deze kwantificatie wordt dus best geautomatiseerd. Om de kwantifatie zo nauwkeurig mogelijk te maken wordt nu voorkennis opgelegd op parameters uit verschillende voxels. Hiervoor werd het algoritme AMARES uitgebreid tot een multivoxel kwantificatie algoritme dat gecombineerd werd met een FIR filter. Een ander aspect van multivoxel kwantificatie is dat de model orde niet voor elk spectrum afzonderlijk bepaald kan worden. Daarom werd de invloed van overmodellering en ondermodellering werd onderzocht.

Wanneer voorkennis tussen parameters uit verschillende voxels wordt opgelegd, dan is de a priori voorkennis niet meer afkomstig uit kwantummechanische berekeningen, maar wordt de voorkennis bepaald door de karakteristieke eigenschappen van een CSI. Zo volgt uit het feit dat het magnetisch veld constant is over de gehele CSI dat de frequentie van de metabolieten constant zal zijn over de gehele CSI. Nu is het mogelijk dat het magneetveld niet volledig homogeen is. Vooraleer deze voorkennis kan opgelegd worden dat de frequenties constant zijn, kan het dus nodig zijn om met behulp van voorverwerking als ECC of een aligneringsalgoritme de spectra uit te lijnen.

Methodes

De invloed van multivoxel kwantificatie en de invloed van de gekozen model orde werd nagegaan met behulp van Monte Carlo simulaties. Drie verschillende simulatiesignalen werden geconstrueerd. Twee CSI's werden gesimuleerd op basis van *in vivo* opgemeten CSI's. Een eerste afkomstig van een gezonde vrijwilliger en bestaande uit 3 gesimuleerde pieken: choline, creatine en NAA;

een tweede simulatie CSI was gebaseerd op een CSI waarin een tumorregio aanwezig was, met daarin 6 gesimuleerde pieken: choline, creatine, NAA, lactaat(doublet) en vet met een grotere lijnbreedte. In beide gesimuleerde signalen werden de frequenties van de metabolieten constant genomen voor alle voxels.

De simulatiesignalen werden dan verwerkt met verschillende methodes. Alle methodes zijn gebaseerd op AMARES$_f$ waarvan een multivoxel kwantificatie versie werd voorgesteld. Hiervoor worden de modelfuncties van de verschillende voxels gecombineerd in 1 kostfunctie. Om de invloed na te gaan van de multivoxel voorkennis werd de CSI verwerkt voxel per voxel, met 5 voxels simultaan en met 10 voxels simultaan. Anderzijds werden de CSI's telkens verwerkt met twee modelfuncties. De CSI met 3 pieken werd gemodelleerd met een modelfunctie met 3 en 5 pieken, waarbij de modelfunctie met 5 pieken een niet aanwezig lactaatdoublet tracht te modelleren. De tumor CSI werd gemodelleerd met 4 en 6 pieken, waarbij de modelfunctie met 6 pieken het spectrum exact modelleert en de modelfunctie met 4 pieken diegene is waarbij het lactaat doublet uit de modelfunctie werd weggelaten.

Resultaten

De simulaties tonen aan dat de frequenties nauwkeuriger geschat worden wanneer 5 of 10 voxels simultaan verwerkt worden. Er kon echter geen verbetering in de schatting van de amplitudes aangetoond worden wanneer enkel voorkennis over de frequenties werd opgelegd. Een verbetering in de nauwkeurigheid van de amplitudeschatting voor multivoxel kwantificatie werd wel aangetoond wanneer als voorkennis vooropgesteld werd dat de fase constant is over de gehele CSI. Uit de simulaties met de verschillende modelfuncties kon worden afgeleid dat overmodellering (dus wanneer lactaat werd gemodelleerd zonder dat dit aanwezig was) geen negatieve invloed had op de nauwkeurigheid van de parameterschattingen van de andere parameters. Wanneer lactaat wel aanwezig was en dit niet werd opgenomen in de modelfunctie, dan had dit wel een negatieve invloed op de nauwkeurigheid van schatting van de overige parameters.

Toepassing van de multivoxel kwantificatiemethode op een *in vivo* CSI bevestigde de resultaten behaald op de simulatiesignalen.

Hoofdstuk 4: Korte Echotijd Kwantificatie: een 2-staps aanpak

Spectra opgenomen met een korte echtotijd (ET $\sim$ 20-30 ms) vereisen een speciale kwantificatie aanpak. Deze spectra worden immers gekenmerkt door een complexe spectrale structuur van de metabolieten en door een verstorende onderliggende basislijn, dewelke moeilijk kan gescheiden worden van het metabolietspectrum.

De metaboliet spectra zijn complex van aard. Ten eerste zijn bij dergelijke korte echotijden de spectra die vertoond worden door bepaalde metabolieten

complexer dan bij lange echotijden. Dit is bijvoorbeeld het geval voor NAA, waarvoor bij lange echotijden kan verondersteld worden dat het uit 1 piek bestaat op 2.1 ppm. Bij korte echotijd verschijnt echter een meer complexe structuur. Anderzijds zijn bij korte echotijd veel meer verschillende metabolieten aanwezig in het spectrum. Bij langere echotijden zijn vele van deze metabolieten reeds volledig uitgedempt en dus niet meer terug te vinden in het spectrum. Deze twee eigenschappen van korte echotijd spectra zorgen ervoor dat er veel overlappende pieken aanwezig zijn, wat de kwantificatie uiteraard bemoeilijkt. Om dit probleem te overkomen wordt getracht zoveel mogelijk gebruik te maken van voorkennis. In de voorgestelde methode wordt dit verwezenlijkt door gebruik te maken van een verzameling modelspectra met gekende concentratie. Er wordt dan een optimale lineaire combinatie van deze modelspectra gezocht om een schatting van de concentraties van de verschillende metabolieten te bekomen. Deze modelspectra kunnen opgemeten fantoomoplossingen zijn, of kunnen gesimuleerd worden door gebruik te maken van kwantummechanische berekeningen. Een derde mogelijkheid bestaat eruit om opgemeten *in vitro* modelspectra te modelleren en deze modellen als ruisloze basisset te gebruiken. De meest gebruikte methode, LCModel, combineert een *in vitro* opgemeten set van modelspectra met een kwantficatie in het frequentiedomein.

Een andere eigenschap van kort echotijdspectra die de kwantificatie verstoort is de aanwezigheid van een basislijn. Deze basislijn is afkomstig van de resonanties van macromoleculen en vetten, dewelke een veel hogere demping hebben en dus een grotere lijnbreedte hebben. De basislijn opnemen in een geparametriseerd model ligt niet voor de hand, omdat geen duidelijke modelfunctie voorhanden is. Men kan trachten de basislijn te verwijderen in een voorverwerkingsstap door bijvoorbeeld een zuivere basislijn op te meten gedurende de acquisitie en deze van het opgemeten signaal af te trekken, of door de opgemeten basislijn mee op te nemen in de databank van modelspectra. Het opmeten van een dergelijke zuivere basislijn is echter niet voordehandliggend, wat maakt dat dikwijls de basislijn benaderd wordt door gebruik te maken van splines of wavelets. Men kan dan kiezen om de basislijn te verwijderen voor de kwantificatie, of het basislijnmodel mee te nemen in de kwantificatie.

Methodes

In dit hoofdstuk wordt een nieuwe methode AQSES_{2step} voorgesteld dewelke gebaseerd is op AQSES. Deze methode is analoog aan de LCModel methode in volgende zin: er wordt gebruik gemaakt van een *in vitro* opgemeten databank van modelspectra om tot een optimale lineaire combinatie van deze modelspectra te komen als benadering van het opgemeten spectrum. Deze methode maakt bijkomend gebruik van het hiervoor reeds geïntroduceerde FIR filter. De gebruikte opgemeten databank van modelspectra bevat 23 metabolieten en 2 opgemeten vetresonanties, teneinde de aanwezige vetpieken te modelleren.

De kwantificatie gebeurt in het tijdsdomein, door een niet lineaire kleinste kwadratenprobleem op te lossen dewelke correcties voor frequenties, dempingen, fases en amplitudes geeft. De modelfunctie die gebruikt wordt is:

$$\bar{y}(t_n) = y_n = \sum_{k=1}^{K} \Delta a_k M_k(t_n) e^{(j\Delta\phi_k)} e^{(-\Delta d_k + j2\pi\Delta f_k)t_n} + \sum_{l=1}^{L} b_l B_l(t_n)$$

waarbij $M_k(t_n)$ het $k$de opgemeten modelspectrum is. De verschillende geschatte correcties worden gegeven door: Δa_k, de amplitudecorrectie; Δd_k, de dempingcorrectie; Δf_k, de frequentiecorrectie en $\Delta\phi_k$ de fasecorrectie. t_n is de tijdsvector. Om de basislijn te modelleren wordt een tijdsdomeinrepresentatie van L kubische B-splines gebruikt: $B_l(t_n)$. De kostfunctie die geminimaliseerd wordt bevat een extra strafterm $p(b_l)$ dewelke voorkomt dat de fit van de basislijn te flexibel wordt. De strafterm wordt gewogen met de regularisatieparameter λ, wat de volgende kostfunctie oplevert:

$$\sum_{n=0}^{N-1} |y_n - \bar{y}_n|^2 + \lambda p(b_l),$$

Een simulatiesignaal werd geconstrueerd gebaseerd op een *in vivo* spectrum opgemeten bij een gezonde vrijwilliger. Dit signaal werd gekwantificeerd met behulp van het AQSES algoritme. De geschatte amplitudecorrecties werden vervolgens gebruikt om een lineaire combinatie van de modelspectra te maken. Een tweede simulatiesignaal werd aangemaakt door kleine (1 Hz) variaties op de frequenties en dempingen van de modelspectra aan te brengen. Een derde simulatiesignaal bevatte naast de gesimuleerde metabolieten ook een gesimuleerde basislijn. Met behulp van Monte Carlo simulaties werd de nauwkeurigheid onderzocht van AQSES_4, waarin enkel 4 *landmarks* gebruikt worden voor de kwantificatie van de signalen, en van AQSES_{25}, waarbij de volledige modelspectra databank gebruikt werd om de signalen te kwantificeren. De 4 landmarks komen overeen met de 4 meest prominente pieken in korte echotijd spectra, namelijk: choline, myo-inositol, creatine en NAA. De methode AQSES_{2step} werd voorgesteld: in een eerste stap worden frequentiecorrecties geschat van de 4 landmarks met behulp van AQSES_4. Deze correcties worden dan gebruikt als startwaarden voor AQSES_{25}.

Als testcase werd de methode AQSES_{2step} toegepast op 50 *in vivo* spectra uit de INTERPRET databank. Verschillende tumortypes waren vertegenwoordigd: glioblastoma's (n=11), medulloblastoma's (n=6), meningioma's (n=10), meningiothelial meningioma's (n=4), astrocytoma's (n=5), metastases (n=7), abscessen (n=3), lymphoma (n=2), Schwanoma (n=2) en adenoma (n=1). De INTERPRET data werden steeds volgens het INTERPRET protocol voorbewerkt: fases worden gecorrigeerd en water werd weggefilterd met een HSVD

filter. De echotijd van de data bedraagt 30 ms en alle spectra werden opgemeten met een PRESS sequentie, wat het mogelijk maakt om deze te analyseren met de voorhanden zijnde modelspectra databank, eveneens opgemeten met behulp van een PRESS sequentie.

Resultaten

De Monte Carlo simulaties op het simulatiesignaal zonder toegevoegde frequentie- en dempingsverschuiving tonen aan dat de AQSES_4 methode nauwkeurigere parameterschattingen oplevert voor realistische signaal-ruisverhoudingen. Deze bevinding werd bevestigd door de Monte Carlo simulaties waarbij een frequentie- en dempingsverschuiving van 1 Hz werd toegevoegd aan het simulatiesignaal. Bij deze Monte Carlo simulaties werd gevonden dat voor alle ruisniveau's AQSES_4 nauwkeurigere parameterschattingen voortbracht dan AQSES_{25}. Dit leidde tot het voorstellen van de methode AQSES_{2step}. Hoewel deze methode niet voor alle metabolieten nauwkeurigere parameterschattingen opleverde toch kon voor bepaalde metabolieten vermeden worden dat er onderlinge verwisselingen gebeurden bij de kwantificatie. Zo werd bijvoorbeeld bij AQSES_{25} de NAA resonantie geschat door de NAAg resonantie, terwijl dit vermeden werd wanneer de AQSES_{2step} gebruikt werd. De 2 stapsmethode is dus voordelig voor het verbeteren van de robuustheid van de kwantificatie. Een soortgelijke verbetering van robuustheid werd geobserveerd voor Lactaat. De Monte Carlo simulaties waarbij een basislijn gesimuleerd werd in het gesimuleerde signaal en waarbij deze basislijn gemodelleerd werd door AQSES_{2step} door de splines leverde geen nauwkeurigere parameterschattingen op wanneer de basislijn mee opgenomen werd in de modelfunctie. Dit kan verklaard worden door het feit dat de regularisatieparameter λ heuristisch gekozen werd en dat hiervoor nog niet automatisch een optimale waarde bepaald wordt.

De *in vivo* data werden met en zonder basislijn model gekwantificeerd, alsook met beperkte voorkennis op de dempingen en met volledige voorkennis voor de dempingen. Met beperkte voorkennis op de dempingen wordt bedoeld dat enkel de dempingen van devolgende metabolieten gelijk zijn aan elkaar: $\Delta d_{Gln} = \Delta d_{Glu}, \Delta d_{GABA} = \Delta d_{Cr}, \Delta d_{PCh} = \Delta d_{GPC}, \Delta d_{NAA} = \Delta d_{NAAG}, \Delta d_{Lipid1} = \Delta d_{Lipid2}$. Als kwaliteitsmaatstaf werden de correlaties en het gemiddelde residue berekend. Wanneer de basislijn mee gemodelleerd werd had dit gemiddeld een hogere correlatie tot gevolg, wat een betere fit aanduidt. Dit is te verwachten aangezien er meerdere variabelen gebruikt worden om het signaal te modelleren. Wanneer de dempingscorrecties voor alle metabolieten gelijkgesteld worden aan elkaar, dan daalt de correlatie en het residue in vergelijking met de situatie waarin beperkte voorkennis op de dempingen was opgelegd. De voorkennis dat alle dempingen gelijk zijn, vermijdt immers dat bepaalde metabolieten brede resonanties die tot de basislijn behoren modelleren. Hoewel de correlatie groter is, toch zullen de geschatte amplitudes misschien minder aanleunen bij de actuele waarden. Belangrijk is hier op te merken dat de methode systematisch faalde bij het modelleren van spectra afkomstig van metastases

waarin vetten prominent aanwezig zijn.

Hoofdstuk 5: Conclusies en Verder Onderzoek

Conclusies

- MRS werd gepresenteerd als techniek waarmee op niet-invasieve wijze metabolieten in kaart kunnen gebracht worden. Er werd een overzicht gegeven van de verschillende voorverwerkings- en kwantificatiemethoden. Frequentie- en tijdsdomein methodes werden besproken, alsook zwartedoos en interactieve methodes.
- Voor de kwantificatie van prostaat MRS data werd aangetoond dat twee methodes, een Tijds Domein Fit algoritme (TDF) en een Frequentie Domein Analyse (FDA) methode, een vergelijkbare nauwkeurigheid hebben in het schatten van de verhouding (creatine+polyamines+choline)/citraat, die een diagnostische waarde heeft. Hiervoor werden beide methodes getest in een Monte Carlo simulatie, en werden ze toegepast op *in vitro* en *in vivo* data. Een Grafische Gebruikers Interface werd voorgesteld waarin prostaat CSI data kunnen worden gevisualiseerd in combinatie met MR beelden. De Gebruikers Interface laat ook toe om CSI data automatisch te kwantificeren met behulp van AMARES. Om een interpretatie van de resultaten mogelijk te maken worden de geschatte amplitudes weergegeven in een metabolietkaart.
- Multivoxel kwantificatie werd voor de eerste maal toegepast op MRSB data. Er werd aangetoond dat afhankelijk van de opgelegde voorkennis, de parameterschatting nauwkeuriger werd wanneer meerdere voxels simultaan verwerkt werden. Toepassing op *in vivo* data toonde aan dat multivoxel kwantificatie ook de robuustheid ten goede kwam. Deze verbeteringen zijn te wijten aan het feit dat multivoxel kwantificatie het toelaat voorkennis op te leggen tussen resonantieparameters behorende tot verschillende voxels. Enkel wanneer voorkennis over de fase werd opgelegd was het mogelijk om een nauwkeurigere schatting van de amplitudes te verkrijgen. Met behulp van Monte Carlo simulaties werd aangetoond dat een beperkte overmodellering geen negatief effect heeft op de parameterschattingen, in tegenstelling tot een beperkte ondermodellering.
- Een 2-staps algoritme voor de kwantificatie van korte echotijd spectra werd gepresenteerd. De 2-staps methode verbetert de robuustheid van de kwantificatie door gebaseerd te zijn op de fit van het spectrum met 4 landmarks en frequentie startwaarden te voorzien voor een tweede volledige kwantificatie. De verbeterde performantie van AQSES_{2step} in vergelijking met AQSES werd aangetoond met Monte Carlo simulaties. Eerste resultaten waarbij de basislijn werd gemodelleerd door splines tonen aan dat een correcte keuze van de regularisatieparameter λ essentieel is voor een accurate kwantificatie.

Verder Onderzoek

- Bij de vergelijking van de TDF en de FDA methode werd enkel de verhouding CCP/C als diagnostische parameter bestudeerd. In realiteit worden echter verschillende bronnen geconsulteerd om een diagnose te vormen. Er dient onderzocht worden of de beide methodes een verschillende bijdrage kunnen leveren wanneer zij gecombineerd worden met andere modaliteiten.

- Heden ten dage verschijnen steeds meer klinische 3 Tesla MR scanners. Vermits spectra opgemeten met deze machines andere eigenschappen hebben, kan het nuttig zijn de vergelijkende studie te herhalen voor spectra afkomstig van 3T machines.

- Een vraag die vanuit de klinische wereld steeds luider klinkt is of MRS van de prostaat ooit deel kan uitmaken van de routine onderzoeken ter diagnose van prostaat kanker. Een antwoord op deze vraag ontbreekt nog.

- In hoofdstuk 3 wordt besproken hoe beperkte overmodellering geen negatief effect heeft op de parameterschattingen. Er zou moeten nagegaan worden of deze conclusie ook opgaat wanneer de modelfunctie een veel grotere model orde heeft dan het gekwantificeerde signaal. Dit is zeker een relevante vraag voor korte echotijd spectra, waarbij veel metabolieten aanwezig kunnen zijn.

- De grootste onderzoeksuitdaging betreffende AQSES_{2step} situeert zich in het vinden van een optimale methode om de regularisatieparameter λ te bepalen. Naast het evalueren van verschillende basislijn modelfuncties, zou ook de invloed van het aantal landmarks in de eerste stap onderzocht kunnen worden.

- Om een methode als AQSES_{2step} te transfereren naar een klinische omgeving moet ze voldoen aan 2 eisen: ten eerste moet ze gemakkelijk te gebruiken zijn, met andere woorden, moet ze ingebouwd worden in een Grafische Gebruikers Omgeving. Ten tweede moet er een schatting van de fout op de gegeven amplitudeschattingen voorzien worden, zodat de betrouwbaarheid van de kwantificatie kan beoordeeld worden. Voortgang werd reeds geboekt op beide punten.

Chapter 1

Introduction

This chapter will introduce the basic aspects of Magnetic Resonance (MR). After a short description of the historical development of Magnetic Resonance, the physical principles behind the technique will be outlined. The different types of data that can be acquired with an MR experiment are discussed next. This introduction then continues with a description of data preprocessing methods, leading to an overview of present quantification algorithms. The relevance of brain and prostate spectroscopy in clinical applications is illustrated. To conclude the introduction, a chapter by chapter overview of this thesis is given.

1.1 Introducing Magnetic Resonance

Nowadays, Magnetic Resonance is a technique used on a daily basis in a clinical environment to generate images from within the human body and to obtain information on the distribution of chemical substances *in vivo*. Worldwide, more than 20.000 MR scanners are installed.

The idea of Magnetic Resonance has been around for some time: the first successful MR experiments were performed in 1946 [7, 81] and were able to reveal the water content from bulk samples. However, a fast development of MR techniques was hindered by a lack of advanced instrumentation. The first studies of proteins and biological molecules in solution only started to emerge after the development of high-field superconducting magnets in the late 1960s. During the following years more biological tissues and samples were studied, which lead to non-invasive studies of human limbs [85] and neonatal brain [11, 126]. Technology improved and first whole-body systems became available. Aside evolutions in MR spectroscopy (MRS), MR Imaging (MRI) started with

the first image of a heterogeneous object by Lauterbur in 1973 [58] and the image of a finger by Mansfield in 1976 [63]. Ever since, MR scanners have continuously improved and have become part of the medical instrumentarium.

1.1.1 Basic Principles

Atomic nuclei have different physical properties that make them unique. For example, the ^{1}H nucleus has a positive unity charge and also is assigned a quantum-mechanical property of *spin* to which a magnetic moment is associated. This can be understood intuitively by imagining the nucleus spinning around its own axis creating a tiny bar magnet along the axis of rotation, as is illustrated in Figure 1.1.

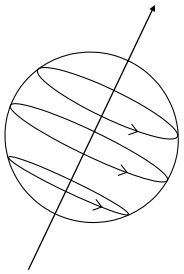

Figure 1.1: Intuitively, the nucleus can be visualized spinning around its own axis, which corresponds with the axis of its magnetic moment.

Due to quantum mechanics two different spin states are possible for the ^{1}H nucleus, *spin up* and *spin down*, which correspond holding states with spin quantum numbers $m = +\frac{1}{2}$ and $m = -\frac{1}{2}$.

When brought in a static magnetic field B_0, the spins will no longer be oriented randomly, but will start to precess around the static magnetic field. However, the different spins will align differently: the magnetic moment of the protons with spin up will align along the magnetic field, whereas the spin down protons will align their magnetic moment inversely to the magnetic field B_0, as is illustrated in Figure 1.2.

The two spin states will have different energies due to the interaction of their magnetic moment with the applied field. This energy difference is proportional to the B_0 field:

$$\Delta E = \gamma \hbar B_0, \hbar = \frac{h}{2\pi}, \tag{1.1}$$

where γ is the gyromagnetic ratio, characteristic to the isotope and h the Planck

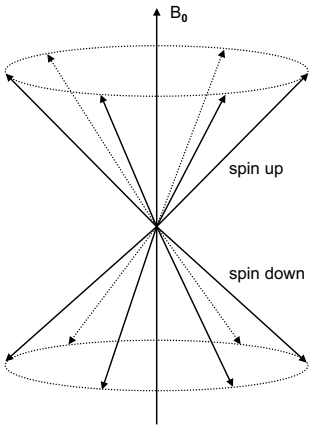

Figure 1.2: Spins precessing around the static magnetic field B_0. The two possible alignments are shown.

constant.

In equilibrium, the distribution between spin up and spin down is described by the Boltzman distribution:

$$\frac{N_-}{N_+} = exp\left(-\frac{\gamma\hbar B_0}{kT}\right), \tag{1.2}$$

where k is the Boltzman constant ($1.381 \times 10^{-23} J/K$) and T the temperature in Kelvin. Because there is a small difference in the populations of both states, there will be a net magnetic field when all spins are combined. The larger the net magnetic field, the larger the difference in populations of both energy levels. By imposing a larger magnetic field, it is possible to increase the net magnetization, which leads to a larger MR signal.

When an oscillating magnetic field is applied to the system of ^{1}H nuclei in a plane perpendicular to the direction of the B_0 field, spins will be excited from the lower to the higher energy state, or from spin down to a spin up state. The frequency of the incoming oscillating field has to correspond with the energy difference between the two states as follows:

$$f_0 = \frac{\gamma B_0}{2\pi}. \tag{1.3}$$

The frequency f_0 is called the Larmor frequency and for a 1.5 T B_0 field this corresponds to a Larmor frequency of 63.86 MHz. High field MR scanners operate at 7 T, which corresponds with a Larmor frequency of about 300 MHz.

Nuclei, other than the ^{1}H nucleus also possess a non-zero spin quantum number and are also eligible for use in MR experiments. Mostly used are ^{1}H, ^{13}C, ^{19}F and ^{31}P. Each of those have different gyromagnetic ratios and will thus resonate at a different Larmor frequency.

When the oscillating magnetic field is turned off, spins will return to their equilibrium state by sending out magnetic waves with the same Larmor frequency. Those magnetic waves are detected by quadrature coils and generate the MR signal, which is called a Free Induction Decay (FID). These relaxation processes are characterized by two relaxation times: T_1, which describes the recovery of the magnetization along the direction of B_0, and T_2, which describes the decay of the magnetization in the plane perpendicular to B_0. In reality, T_2 is never observed due to field inhomogeneities. Instead T_2^* is observed, which is the T_2 with corrections for both effects.

1.1.2 Magnetic Resonance Spectroscopic Imaging

In the previous section, the basic principles of how a basic MR signal is generated are discussed. This paragraph will elucidate how this technique can be used to obtain relevant biochemical information on *in vivo* tissues.

In equation 1.3, the resonance frequency is calculated. However, depending on the molecule and the position in the molecule the ^{1}H nucleus is situated in, the experienced magnetic field will be slightly different from the applied static magnetic field B_0. This is due to screening effects by the orbital motion of the electrons, which produce a small field at the nucleus that is proportional and opposite to B_0. The effective field B_{eff} experienced by a certain nucleus is described as:

$$B_{\text{eff}} = B_0 - \sigma B_0 = (1 - \sigma)B_0 \tag{1.4}$$

The small secondary field, which lowers B_0, is determined by the screening or shielding constant σ. The effect of this screening, and thus of this different B_{eff}, is that nuclei in different molecules or in different locations within a molecule will resonate at different frequencies:

$$f_{\text{eff}} = \frac{\gamma}{2\pi}(1 - \sigma)B_0. \tag{1.5}$$

This effect is called *chemical shift*. Because the magnitude of σ is dependent upon the electronic environment of the nucleus, and therefore nuclei in dif-

ferent environments give rise to signals at different frequencies, the chemical identifying nuclei by their frequencies. From now on the *eff* subscript will be omitted further, only f will be used to denote the chemical shift of a certain metabolite. Frequencies are often expressed in the dimensionless unit parts per million, which expresses the B_{eff} relative to the B_0 field.

The most basic MR experiment thus consists of sending a fluctuating magnetic field (in case of 1.5 T, this is a radio-frequent (RF) pulse) into a sample and to record the FID. The time between the excitation pulse and the acquisition of the FID is called the echo time (TE). The RF pulse is extended with a combination of RF pulses and field gradients for obtaining a signal from a spatially localized area. Mainly, the STEAM (STimulated Echo Acquisition Mode) [35] and PRESS (Point RESolved Spectroscopy) [8] sequences are used for spatially resolved spectroscopy. Both sequences select the volume of interest (VOI) by applying three consecutive 90 and/or 180 pulses combined with field gradients. The PRESS sequence has a higher sensitivity than the STEAM sequence because an echo is acquired, but cannot be used with very short TE. The STEAM sequence can acquire spectra at a very short TE, but has less sensitivity. The area which is excited by the sequence is referred to as the STEAM or PRESS box. The volume of which an FID is acquired is called a voxel.

Nowadays, the basic STEAM and PRESS sequences are combined with other RF pulses and field gradients to enhance the quality and the information content of the spectra. Due to the intrinsic low intensity of the radiated signal, the RF coil used to pick up the signal is mostly put as close to the investigated organ as possible. For an MRS measurement on the brain, the brain is put in a birdcage headcoil, which encloses the head. To acquire prostate spectra and images, an endorectal coil is used, that is positioned against the prostate.

Two different types of spectroscopic sequences can be distinguished: Single Voxel Spectroscopy (SVS) and Chemical Shift Imaging (CSI) (also called Magnetic Resonance Spectroscopic Imaging (MRSI))[9, 66]. SVS measures a single FID from a single voxel. It is often preferable to monitor the metabolic state of different regions. This can be achieved by a CSI sequence, which acquires multiple FIDs from voxels arranged in an array. The array can be two dimensional, or three dimensional typically with dimensions $16 \times 16(\times 16)$ or $32 \times 32(\times 32)$. To acquire a CSI, the recorded FID's have to be encoded according to their spatial position in the CSI grid. Using field gradients during the acquisition of the FID is not possible because this would destroy the chemical shift information. Therefore, spatial encoding is performed prior to acquisition of the FID by switching on field gradients in the spatial directions of the CSI grid. In this way, acquired FIDs will be phase encoded, which can be decoded by a Fourier Transformation from the phase encoded space (also *k space*) to the spatial space. The spatial resolution of spectroscopic imaging is limited due to the intrinsic low SNR ratio of the signals, which requires voxels volumes to

be adequately large. Sizes of CSI voxels are typically in the range of a few cc, with a minimum of around 1 cc for clinical studies. An example of a 16×16 CSI is shown in Figure 1.3.

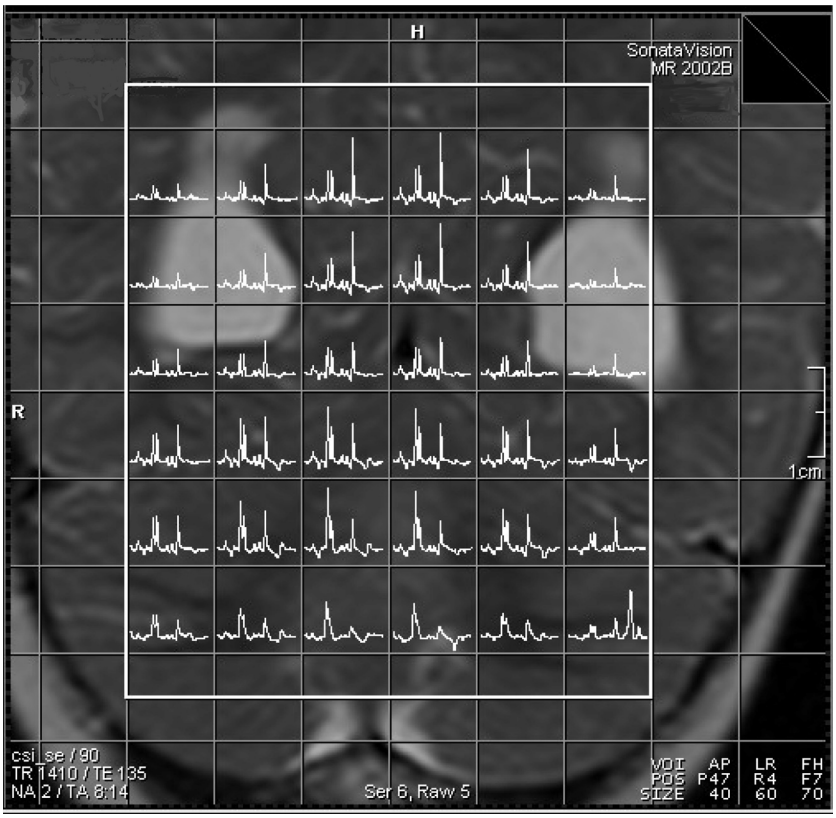

Figure 1.3: An example of a CSI measured in the brain. Only part of the 16×16 CSI is visible and only spectra originating from voxels within the (white) PRESS box are shown.

Different parameters are shaping an MRS sequence. The timing of the different pulses is determined by the echo time (TE) and the repetition time (TR). The shorter the TE, the more metabolic information will be present in the spectra because less metabolites will have decayed. To increase the signal strength, repeated measurements are performed and a number of FID's is acquired with an time interval of TR, which is a compromise between the optimal relaxation of the spins to their initial state and the total measurement time. Typically short (e.g. 35 ms) and long (e.g. 135 ms) echo times are used, combined with a TR of around 2000 ms. A single voxel acquisition with 128 averages takes about four minutes, while a 16×16 CSI with 8 averages and a TE of 700 ms

needs about 20 minutes. The area which is covered by a CSI grid is acquired is called the field of view (FOV).

Magnetic Resonance Imaging techniques are not discussed here but are based on the same principles. The interested reader is referred to [41].

1.2 Data Preprocessing

In this and the following section an overview will be given of existing preprocessing and quantification methods.

The recorded signal FID is acquired in the time domain, but for visualization, data are transformed to the frequency domain using a Fast Fourier Transform (FFT), where the composition of the signal can be easily interpreted. An example of a brain and prostate spectrum will be discussed in detail in the next sections.

In this thesis only proton spectra were used, which makes that only chemical substances (metabolites) containing ^{1}H atoms will be present in the signals. The concentration of water (a molarity around 55 M, or 55 moles/liter), is 1000 to 10000 times larger than the concentration of the metabolites of interest (order of mM) which leads to two problems. There is a hardware acquisition problem related to the dynamic range of the equipment which has to be large enough to acquire the water signal as well as the metabolite resonances simultaneously. Secondly because the water has a much larger concentration, the spectral region of interest can be disturbed by the sidelobes of the much larger water peak. A similar problem arises when lipids are excited by the sequences. Most sequences have incorporated pulses which suppress the water and lipids such as CHESS [84] and BASING [98] sequences.

Using MRS it is possible to estimate the concentrations of the different metabolites. However, extracting the relevant information of the signals is not straightforward. Due to the inherently low intensity of the MRS technique, preprocessing has to be performed to obtain reliable concentration estimates. The data often suffer from several artefacts such as residual water contamination, poor signal to noise ratio (SNR) or frequency shifts, which require appropriate preprocessing of the data. The different preprocessing steps will be discussed in the next paragraphs.

Different preprocessing steps exist to improve the quality of the signals in order to enable a better quantification of the signals.

As was discussed above, spectra are often disturbed by large water and lipid residuals (often called *nuisance peaks*). Because the large peaks hinder the quantification in the time domain as well as in the frequency domain, they

have to be eliminated as much as possible.

Different approaches have been suggested for the removal of nuisance peaks. Two conceptually different groups of methods can be distinguished. The first group creates an estimate of the water peak and subtracts it from the model. The estimate of the water residual can be obtained using different techniques. A first technique [65] performs a low-pass convolution, which suppresses all high frequency spectral components in the spectrum leaving only a water residual estimate in the spectrum. A different approach [105] to obtain an estimate of the residual water uses Hankel Singular Value Decomposition (HSVD) [5], which models the water region by a sum of exponentially damped sinusoids. The model is then subtracted from the spectrum, leaving only the metabolites [114].

The second group eliminates the water region by applying filters or convolution techniques directly to the signal. An example of this approach can be found in [20]. A disadvantage of the filters mentioned above is that the filtered signal includes distorted samples and that there is a loss of energy, due to removed sampling points. To cope with these drawbacks, an advanced automatically designed maximum phase finite impulse response (FIR) filter was also proposed [100]. Because this filter will be combined with quantification algorithms, it will be discussed in more detail in the next chapter.

Some frequently used preprocessing steps will be discussed now.

Zerofilling: raw time domain data can be extended with a set of zeros. This implies that the part of the signal which isn't acquired and which was supposed to have relaxed entirely has zero value. The effect of zerofilling is an increase in resolution, equivalent to an interpolation in the frequency domain, which improves spectral visualisation. However if the signal hasn't decayed to zero at the end of the acquisition, zerofilling will induce a discontinuity resulting in a distorted Lorentzian line.

Filtering or apodization: the time domain data can be multiplied by an appropriate filter or weighting function. Typically an exponential envelope function is used for this purpose. Depending on the parameters of the filter function, the filter will have different effects. When the damping of the filter function is taken to be equal to the exponential decay of the original signal (matched filter), the filter will have the effect of increasing the SNR. This is due to the fact that initial points of the FID, having a larger SNR, get a higher weighting than points at the end of the FID, which contain mainly noise. This kind of filter can also be used to reduce the effect of truncation artefacts. The opposite filter has a negative damping constant and will increase the total decay time. This leads to narrower peaks in the frequency domain, or an increase in resolution, thereby reducing the problem of highly overlapping peaks. It is obvious that using the filter to optimize the SNR will have a negative effect on resolution

and vice versa.

Corrections using a reference signal: During an additional acquisition a water reference signal is acquired which can be used for several purposes.

A first application is to use the water reference for eddy current correction (ECC). Eddy currents are induced by the switching of magnetic field gradients in localized spectroscopy sequences. The eddy currents induce a time-dependent magnetic field which induces an additional phase shift in the FID. By dividing the original signal pointwise by the phase part of the reference signal, influences of the eddy current will be cancelled out, thereby producing an eddy current corrected signal[49].

In a second application the water reference is used to correct for frequency shifts, which can be unwanted, especially in CSI data[26] or in time series [10, 122].

A third application, called QUALITY [28], uses the reference signal to convert irregular lineshapes to Lorentzian lineshapes, which will improve performance of model-based quantification algorithms. Unfortunately, the acquisition of a reference signal itself is also sensitive to errors. Experimental conditions might change between the acquisition of the spectral data and the reference signal, leading to erroneous ECC or frequency shift corrections. Another drawback is that for clinical applications of MRS, the acquisition of additional reference signals can be too time consuming.

After Fourier transform other corrections can be performed to improve the visualization or quantification in the frequency domain.

Phasing: due to the quadrature acquisition (i.e. real and imaginary part of the FID recorded simultaneously), a phase shift might occur. This leads to a mixture of absorption and dispersion modes after Fourier transformation. An example can be seen in Figure 1.4. Using an automatic or manual phase correction, a pure absorption spectrum can be obtained.

Zero order phase corrections are easily incorporated by multiplying the time domain signal with a correcting complex phase factor. First order phase shifts are linearly dependent on the frequency and originate mainly from the delay between the excitation pulse and the first point of the acquisition of the time domain signal. First order phase corrections are more difficult to perform than zero order phase corrections.

Baseline Correction: the baseline of a spectrum can be distorted by broad underlying resonances (such as macromolecules), acquisition or hardware artefacts or by the tail of a badly suppressed water resonance. Any of those baseline shifts, render the quantification of the much smaller metabolites problematic. Certainly when an integration approach is used, the baseline will introduce

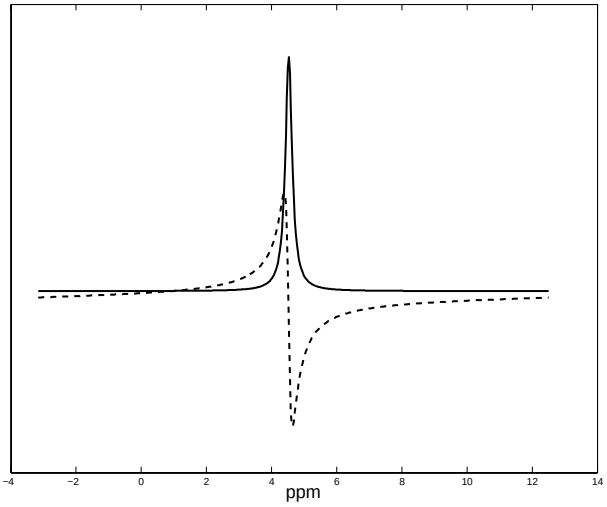

Figure 1.4: Example of a pure absorption spectrum of a single resonance (solid line) and a dephased spectrum, which is a mixture of absorption and dispersion modes (dashed line). The dephased spectrum is 50 degrees out of phase.

a bias to the estimation of the metabolite levels. A correction of the bumpy, rolling baseline is thus needed to enable accurate quantification. The most simple approach of removing the baseline is to estimate the baseline using spline or polynomial functions and to subtract it from the original signal yielding a flat baseline. A major issue is that it is very difficult to assess the contribution of the baseline to the metabolite levels. The baseline which originates from larger less mobile molecules as macromolecules is only visible at short echo time spectra.

1.3 Data Quantification

Because the signals are sampled on the MR scanner, a discrete time domain model is often used to estimate the signals. Theoretically the FID can be modeled by the sum of K exponentially damped sinusoids, where K is the number of expected sinusoids, which is assumed to be known:

$$\bar{y}(t_n) = \sum_{k=1}^{K} a_k e^{j\phi_k} e^{(-d_k + j2\pi f_k)t_n} \tag{1.6}$$

where a_k is the amplitude, f_k the frequency, d_k the damping and ϕ_k the phase of

the kth spectral component ($k = 1, \ldots, K$); $t_n = n\Delta t + t_0$ with Δt the sampling interval, t_0 the time between the effective time origin and the first data point to be included in the analysis. The damping constant d_k of the linear exponential decay is equal to $1/T^*_{2k}$ for the given metabolite k. In this model, the parameter of utmost interest is a_k which represents the amplitude of resonance k. Because the amplitude is proportional to the number of nuclei contributing to that component of the spectrum, it will also be proportional to the concentration of that metabolite. The model describes a Lorentzian lineshape, which models the relaxation in ideal circumstances. The realistic lineshape differs from the theoretical lineshape under the influence of field homogeneity variations, tissue susceptibility changes and eddy currents caused by switching field gradients. Often a Gaussian lineshape with quadratic exponential decay is used. The model function for the Gaussian lineshape is:

$$\bar{y}(t_n) = \sum_{k=1}^{K} a_k e^{j\phi_k} e^{(-d_k t_n + j2\pi f_k)t_n} \tag{1.7}$$

As was discussed before, time domain signals are often transformed to the frequency domain by means of a FFT. Given that the spectrum is phased correctly, pure absorption lines are obtained, which correspond to the real part of $y(f)$. The model function can be written in the frequency domain as well:

$$Re(\bar{y}(f)) = \sum_{k=1}^{K} \frac{a_k d_k}{(d_k^2 + (f - f_k)^2)} \tag{1.8}$$

which describes the sum of K Lorentzian lineshapes. Because the Fourier transform is a linear transformation, the information content in the time domain signal $y(t)$ and the frequency domain signal $y(f)$ is the same. Therefore, the estimation of metabolic concentrations can be done in the frequency domain as well as in the time domain. This will be discussed further on.

Data quantification encompasses all methods deployed to achieve estimates of the signal intensities and thus estimates of the concentrations of the metabolites. This can be done either in the time domain or in the frequency domain.

1.3.1 Prior Knowledge

In vivo spectroscopy data have an intrinsic low signal-to-noise ratio and often different peaks in the spectrum are highly overlapping, thereby making an easy quantification not straightforward. To ensure more robust and accurate quantification often *prior knowledge* is used. The most basic form of prior knowledge is the model function which is used to model the data. Other types

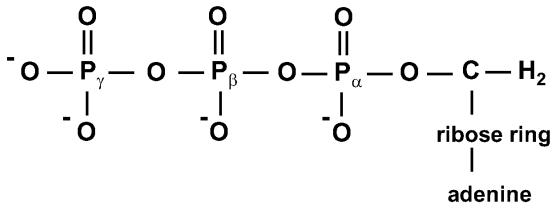

Figure 1.5: the ATP compound molecule structure. Phosphorus atoms are located at three different position within the compound, leading to different shielding for those atoms.

of prior knowledge are the chemical shifts of the metabolites or the possible amplitude ratios.

Some metabolites show a complex spectrum, exhibiting multiple peaks due to the quantummechanical J-coupling. The first application of this kind of prior knowledge was the quantification of the ^{31}P spectra of muscles containing adenosine triphosphate (ATP) signals [110], which exhibit J-coupling. Although not used in this text, it serves as a nice example to illustrate the kind of prior knowledge available from such calculations. The ATP molecule has three different phosphor atoms $\mathrm{P}_\alpha, \mathrm{P}_\beta$ and P_γ in different positions within the molecule and they will thus experience different electric and magnetic fields leading to different shielding values as can be seen in Figure 1.5.

As a consequence the three atoms will resonate at three different frequencies. On top of this, spin-spin coupling between neighbouring phosphor atoms will split the peak of P_α and P_γ into two peaks (a doublet) and the P_β into three peaks (a triplet) as is shown in Fig. 1.6.

Quantummechanical calculations of the J-coupling effects show that the parameters of the ATP spectrum obey the following relations:

- the frequency split caused by the spin-spin interaction is equal for the different multiplets. Or: $f_1 - f_2 = f_3 - f_4 = f_5 - f_6 = f_6 - f_7 = \Delta f$.
- the dampings of all peaks are equal: $d_1 = d_2 = d_3 = \ldots = d_7$
- the doublet peaks of the P_γ and P_α atoms and the central peak of the P_β triplet have equal amplitudes. The outer peaks of the P_β triplet have an amplitude which is half the amplitude of the central peak. In summary: $a_1 = a_2 = a_3 = a_4 = 2a_5 = a_6 = 2a_7$

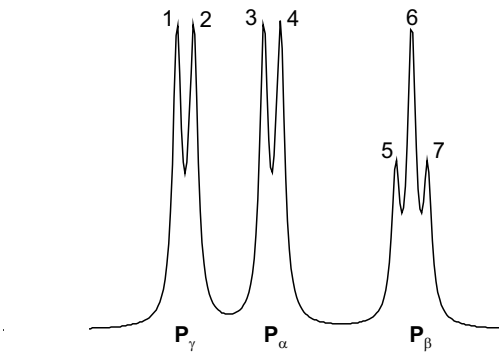

Figure 1.6: Example of the ^{31}P spectrum of ATP. Three groups of resonances can be seen, corresponding to P_α, P_β and P_γ atoms. Due to spin-spin coupling the resonances are split into two doublets and one triplet.

- all peaks have the same phase: $\phi_1 = \phi_2 = \phi_3 = \ldots = \phi_7$.

In ^{1}H spectra, spectral patterns are sometimes quite complex, showing multiple lines and multiplets throughout the spectral range. Calculating the prior knowledge theoretically as can be done for ATP is not always possible. An alternative way to assess parameter relations within a metabolite spectrum is to measure the individual metabolites *in vitro* in the same experimental conditions as the *in vivo* experiment[27]. From these spectra information on multiplet structure, amplitude ratios, frequency shifts and linewidths can be obtained. To take all available prior knowledge of the *in vitro* measured spectra into account, the *in vivo* signals can be modeled as a linear combination of *in vitro* measured signals. A disadvantage of the method is that the basis set of metabolite spectra has to be recorded and that every time experiment parameters are changed this has to be redone. However this problem can be solved by using spectral simulation to simulate metabolite spectra [124, 102]. The known chemical shifts of each singlet or multiplet group together with J-couplings, field strength and pulse sequence and its timing provide the input for the spectral simulation. A combination of prior knowledge extracted from *in vitro* measurements and quantummechanical calculations on the citrate multiplet was used in the quantification of prostate ^{1}H spectra [107, 106, 86, 69, 115]. Using prior knowledge can improve both robustness and accuracy of quantification, but special care has to be taken to assure that the conditions *in vivo* correspond with the conditions for which the prior knowledge is valid. Changes in pH, temperature or other physiological abnormalities might render the prior knowledge incorrect, which might worsen the quantification instead of improving it.

The problem of obtaining estimates of metabolite concentrations can be tackled in the frequency domain as well as in the time domain.

1.3.2 Frequency Domain Methods

Whereas in the time domain the concentration is proportional to the amplitude of the signal, in the frequency domain the concentration will be proportional to the area under the metabolite peak.

This leads us to the most straightforward frequency domain methods, the *non-parametric* quantification methods. An estimate of the area under the peak is obtained by integrating the frequency domain signal. The advantages are that there are no model assumptions needed and that it is very robust. An estimate will be obtained at any time, because no conversion is to be achieved. There are some drawbacks as well. The accuracy of the method is highly depending on proper phasing which can be quite tough to perform. Using automatic phasing can introduce errors in the quantification. Besides the phasing problem, the problem of the integration boundaries has to be tackled. Theoretically, to achieve an estimate of the total signal intensity, the peak should be integrated over the whole frequency domain. In practice this is not feasible due to the overlap of different peaks. So due to the limited integration boundaries, some part of the area will always be missed. This problem is more pronounced for Lorentzian lineshapes which have broader tails than Gaussian lineshapes. More problematic than the error which is made by not integrating the whole frequency domain is a possible lack of resolution, which can make it impossible to resolve two adjacent peaks due to their largely overlapping peaks. Also when water or lipid resonances are still present despite suppression and filtering, they can introduce a baseline shift, which will introduce bias to the estimates.

The *parametric* frequency domain methods are more complicated than the non-parametric ones. The basic principle which is used here is to use a model function to model the spectrum. Mostly a sum of Lorentzian lineshapes is used as model function, as was described in Eq. 1.8. If the model differs from the Lorentzian lineshape (e.g. Gaussian) an analytical model in the frequency domain cannot be calculated (however for Gaussian lineshapes an analytic expression for the real part of the frequency domain function can be calculated). A work-around for this problem is to calculate the model in the time domain and transfer numerically to the frequency domain using a FFT [38, 93]. In the frequency domain model parameters are then estimated using a Non Linear Least Squares (NLLS) algorithm, which will minimize the norm between the spectrum and the model function:

$$\sum_{l=0}^{L} |spectrum_l - model_l|^2 \tag{1.9}$$

where the the sum runs through all the L samples of the spectrum.

From a theoretical point of view this approach is completely equivalent to the minimization problem in the time domain.

A third method proposed by Provencher [79] uses *in vitro* acquired metabolite model spectra as a basis to model the spectrum as a linear combination of those spectra in the frequency domain. The model used can be written in the time domain:

$$S(t_n) = \sum_{k=1}^{S} \Delta a_k M_k(t_n) e^{j\Delta\phi_k} e^{(-\Delta d_k + j2\pi\Delta f_k)t_n} \tag{1.10}$$

Where S is the number of measured metabolite solutions M_k. $\Delta a_k, \Delta d_k, \Delta\phi_k, \Delta f_k$ represent the difference in amplitude, damping, phase and frequency between the acquired metabolite solutions and the signal to be analyzed. Remark that actual quantification is done using the metabolite database in their frequency domain representation. Using a non linear least squares minimization problem a maximum likelihood solution is found. Major advantage is that model imperfections due to acquisition effects are included in the acquired basis functions and that the maximum amount of available prior knowledge is used. Disadvantages of the method is that the basis set of metabolite spectra has to be recorded and that every time the pulse sequence is changed this has to be redone.

Another disadvantage is that it has to be decided beforehand which metabolites will be modelled. In this way estimating unknown resonances is not possible. This method is implemented in the commercially available software package LCModel.

1.3.3 Time Domain Methods

Quantification methods often suppose the noise of the signals to be circular complex white Gaussian noise. By circular is meant that the real and imaginary part of the noise is uncorrelated and that they have the same variance.

Interactive Methods

When the above assumption holds, minimizing the squared difference between the model function and the data yields maximum likelihood (ML) estimates for the model parameters. To solve the nonlinear least squares (NLLS) minimization problem by using a variable projection functional, the model function is split into a linear and a nonlinear part. The functional to be minimized can be written in vector notation:

$$\|\mathbf{y} - \overline{\mathbf{y}}\|^2 \tag{1.11}$$

where $\|\cdot\|$ denotes the Euclidean vector norm and $\mathbf{y} = [y_0, \ldots, y_{N-1}]$ denotes the sampled data points and $\overline{\mathbf{y}} = [\overline{y}_0, \ldots, \overline{y}_{N-1}]$ denotes the model. This functional can be split into a linear and nonlinear part by rewriting Eq. (1.6) as follows:

$$\overline{y}_n = \sum_{k=1}^{K} c_k \gamma_k(\boldsymbol{\alpha}_k, n),\ n = 0, \ldots, N-1 \tag{1.12}$$

were c_k are the complex amplitudes and $\gamma_k(\boldsymbol{\alpha}_k, n)$ are independent functions of the nonlinear parameter vector $\boldsymbol{\alpha}_k$. More specific: $\boldsymbol{\alpha}_k$ equals $[f_k\ d_k\ t_0]$, $c_k = a_k e^{j\phi}$ and $\gamma_k(\boldsymbol{\alpha}_k, n) = e^{(-d_k + j2\pi f_k)n\Delta t}$. Using matrix notation Eq. (1.12) becomes:

$$\overline{\mathbf{y}} = \boldsymbol{\Gamma}\mathbf{c} \tag{1.13}$$

where $\mathbf{c} = [c_1, \ldots, c_K]^T$ and

$$\Gamma = \begin{bmatrix} \gamma_1(\boldsymbol{\alpha}_1, 0) & \cdots & \gamma_K(\boldsymbol{\alpha}_K, 0) \\ \vdots & \ddots & \vdots \\ \gamma_{N-1}(\boldsymbol{\alpha}_1, N-1) & \ldots & \gamma_K(\boldsymbol{\alpha}_K, N-1) \end{bmatrix}$$

is an $N \times K$ matrix of full rank. If the matrix $\boldsymbol{\Gamma}$ would be a known estimation of the linear parameters, $\mathbf{c}$ could be calculated from the linear least squares (LS) problem $\hat{\mathbf{c}} = \boldsymbol{\Gamma}^{\dagger}\mathbf{y}$, where $\boldsymbol{\Gamma}^{\dagger}$ denotes the pseudo-inverse of $\boldsymbol{\Gamma}$, i.e. $\boldsymbol{\Gamma}^{\dagger} = (\boldsymbol{\Gamma}^H\boldsymbol{\Gamma})^{-1}\boldsymbol{\Gamma}^H$ (the superscript H denotes the complex conjugate). The cost function of Eq. (1.11) then becomes:

$$\|\mathbf{y} - \boldsymbol{\Gamma}\boldsymbol{\Gamma}^{\dagger}\mathbf{y}\|^2 \tag{1.14}$$

By rewriting the cost function, the linear parameters are eliminated from the cost function. It was however proven that both cost functions (Eq. (1.11) and Eq. (1.14)) have the same solutions for the nonlinear parameters [36]. Such a solution for the nonlinear parameters can then be used to calculate $\boldsymbol{\Gamma}$ and the linear parameters $\mathbf{c}$ can be found by solving the linear LS problem $\hat{\mathbf{c}} = \boldsymbol{\Gamma}^{\dagger}\mathbf{y}$. Both NLLS problems can be tackled using local or global minimization theory. Global minimization should be used to prevent local solutions to the problem. The disadvantage of global minimization techniques is however that

convergence to a solution cannot be guaranteed. On the other hand, when good starting values are supplied to the local optimization methods, this will result in a global minimum solution in a reasonable time in most cases. Good starting values for the nonlinear parameters as frequency and damping are provided by *peak picking*. By peak picking, rough estimates of dampings and frequencies are obtained from the frequency domain by visual inspection. This step requires user interaction, hence methods based on this principle are called *interactive methods*. Automatic selection of starting values by using black-box methods was suggested as well [77], but for optimal robustness manual peak picking should be preferred.

Initially the variable projection algorithm VARPRO [110] was used, which is based on the Levenberg-Marquardt [73] minimization algorithm. This algorithm was further improved to the AMARES algorithm [115](*A*dvanced *M*ethod for *A*ccurate, *R*obust and *E*fficient *S*pectral fitting), which enables the user to impose more types of prior knowledge on the parameters and also improves VARPRO in terms of robustness and flexibility. Also fitting of echo signals and using non Lorentzian model functions became possible by the introduction of AMARES. Other methods to minimize the cost function were suggested [67, 13] but will not be discussed here.

The ability of the interactive methods to incorporate different model functions as well as different types of prior knowledge make them a favorable choice for quantification of low SNR spectra. Also the fact that the methods deliver ML parameter estimates if noise assumptions hold is an advantage of these methods. Unfortunately, user interaction is required to provide starting values and there is no guarantee of convergence to a global minimum.

Combined FIR filter and AMARES

AMARES offers the possibility to take different kinds of prior knowledge into account during parameter estimation. Therefore the following cost function is minimized for the Lorentzian lineshape:

$$\sum_{n=0}^{N-1} \left| y_n - \sum_{k=1}^{K} a_k e^{j\phi_k} e^{(-d_k + j2\pi f_k)t_n} \right|^2 \tag{1.15}$$

By combining AMARES with an FIR filter, the filter effects can be taken into account in the model function leaving the metabolic peaks intact. This will be elaborated now. An FIR filter is defined by the convolution:

$$y_n^{fil} = \sum_{m=0}^{M-1} h_m y_{n-m}$$

$$n = 0, 1, \ldots, N-1 \tag{1.16}$$

where h_m are the constant filter coefficients. Because the signal is sampled from $t = 0$, the samples for $n < 0$ are not available. The solution to this problem, assuming that the signal is cyclic or that the signal is zero outside the time window, distorts the first $M-1$ samples. Therefore those $M-1$ samples should be discarded when calculating the filtered signal. Let

$$\begin{aligned} x_k(n) &= a_k e^{j\phi_k} e^{(-d_k + j2\pi f_k)t_n} \\ k &= 1, 2, \ldots, K \end{aligned}$$

denote the individual exponentially damped complex sinusoids. Filtering the MRS signal model and discarding the first $M-1$ samples yields

$$\begin{aligned} \overline{y}_n^{fil} &= \sum_{m=0}^{M-1} h_m \overline{y}_{n-m+M-1} \\ &= \sum_{m=0}^{M-1} h_m (x_1(n-m+M-1) \\ &\quad + x_2(n-m+M-1) \\ &\quad + \cdots + x_K(n-m+M-1)) \\ &= \bar{h}b_1 x_1(n) + \bar{h}b_2 x_2(n) + \cdots + \bar{h}b_K x_K(n) \\ &= \sum_{k=1}^{K} \bar{h}b_k x_k(n) \\ n &= 0, 1, \ldots, N-M, \end{aligned} \tag{1.17}$$

where

$$\bar{h} = (h_{M-1} \ldots h_0)$$

and

$$b_k = (1 \quad e^{(-d_k + j2\pi f_k)t_1} \quad \ldots \quad e^{(-d_k + j2\pi f_k)t_{M-1}})^T \tag{1.18}$$

Eq. (1.17) shows that a filter can be constructed which eliminates certain resonances x_k by choosing the filter coefficients in such a way that $\bar{h}b_k \approx 0$. This means that also the tails from the resonances will be filtered out, and not only a certain frequency band around the peak. Eq. (1.18) indicates that filter

coefficients are dependent of signal parameters. To overcome this problem, the filter design scheme is based on the assumption that the water peak consists mainly of one exponentially damped sinusoid of which the parameters can be obtained using the energy distribution of the spectrum. It is important to note that this assumption is merely used to estimate the energy content and the frequency localization of the water peak and does not impose restrictions on the actual model of the water. For details, the reader is referred to [100, 101]. The design of the FIR filter is such that the filter length M is fixed by the filter algorithm and that $M-1$ samples have to be discarded. A maximum-phase filter which minimizes the energy content in the discarded samples is used. The advantage of using an FIR filter approach is that it is faster and more accurate than other HSVD based filter methods and that it can be fully automated [100].

The quantification also benefits from using an FIR filter because the effects of the filter on the signal can be inserted in the model function. To do so the model function after filtering (Eq. (1.17)), is inserted in the cost function of the minimization problem:

$$\sum_{n=1}^{N-M} \left| y_n^{fil} - \sum_{k=1}^{K} \bar{h} b_k x_k(n) \right|^2 \tag{1.19}$$

This method is called AMARES$_f$ and will be used in chapter 2 and extended in chapter 3. The filtering procedure can be interpreted as a prewhitening operation, which justifies the use of the estimation algorithm[100].

Black-box methods

Black-box methods differ from the interactive methods because they don't need any user interaction or starting values. The spectroscopic signals are put into a *black box* and deliver the parameter estimates without user interaction. This removes the user induced parameter variability, but also puts limitations on the possibility of imposing prior knowledge. A second drawback is that these methods deliver statistically suboptimal parameter estimates. Remark that the methods described here also are used for nuisance peak filtering. The principles of two black-box methods will be shortly outlined now: a linear prediction method and a state-space based method.

Linear Prediction Methods

The model of Eq. (1.6) can be rewritten in terms of complex amplitudes c_k and signal poles z_k as follows:

$$\bar{y}_n = \sum_{k=1}^{K} (a_k e^{j\phi_k})(e^{(-d_k + j2\pi f_k)n\Delta t}) = \sum_{k=1}^{K} c_k z_k^n. \tag{1.20}$$

A polynomial of degree K having the signal poles as roots can be formed

$$p(z) = \prod_{k=1}^{K} (z - z_k) = \sum_{i=0}^{K} p_i z^{K-i} \text{ with } (p_0 = 1), \tag{1.21}$$

p_k are the so-called forward prediction coefficients. Using the fact that $p(z_k) = 0$ and $1 \leq k \leq K$, the following holds for all k

$$z_k^m = -\sum_{i=1}^{K} p_i z_k^{m-i},\ m \geq K. \tag{1.22}$$

Combining Eqs. (1.20) and (1.22) gives

$$\begin{aligned} \bar{y}_n &= -\sum_{k=1}^{K} c_k \left(\sum_{i=1}^{K} p_i z_k^{n-i} \right) \\ &= -\sum_{i=1}^{K} p_i \left(\sum_{k=1}^{K} c_k z_k^{n-i} \right) \\ &= -\sum_{i=1}^{K} p_i \bar{y}_{n-i},\ n \geq K \end{aligned} \tag{1.23}$$

The theoretical series $y_n, n = 0, \ldots, N-1$ of Eq. (1.20) can be prolonged by an aribitrary number of points using Eq. (1.23) and this procedure is therefore called forward linear prediction. A similar reasoning as above can be repeated to define backward linear prediction.

To determine the prediction coefficients two different approaches have been proposed. The first is based on autocorrelation coefficients of the data points [51], while the second works on the data points directly. Here only the second option is explored further.

Evaluating Eq. (1.23) for different values of $n = K, \ldots, N-1$ and arranging them in a matrix results in

$$\begin{bmatrix} y_K \\ y_{K+1} \\ \vdots \\ y_{N-1} \end{bmatrix} = - \begin{bmatrix} y_0 & \cdots & y_{K-1} \\ y_1 & \cdots & y_K \\ \vdots & \ddots & \vdots \\ y_{N-K-1} & \cdots & y_{N-2} \end{bmatrix} \begin{bmatrix} p_K \\ p_{K-1} \\ \vdots \\ p_1 \end{bmatrix}$$

or

$$\mathbf{h}_{\mathrm{lp}} = -\mathbf{H}_{\mathrm{lp}}\mathbf{p} \tag{1.24}$$

This equation is in the absence of noise exactly solvable and gives exact linear prediction coefficients $\mathbf{p}$. By rooting the polynomial $p(z)$ specified in Eq. (1.21) the signal poles z_k, $k = 1, \ldots, K$ are obtained from which the frequencies and dampings can easily be computed. The signal poles are filled in in Eq. (1.20) and the exact amplitudes can then be deterimined from this set of equations.

When noise is present, Eq. (1.24) holds only approximately, and no exact solutions can be found.

State Space Methods

The state space method takes another approach. The $y_n, n = 0, \ldots, N-1$ data are ordered in a so-called Hankel matrix as follows:

$$\mathbf{H} = \begin{bmatrix} y_0 & y_1 & \cdots & y_M \\ y_1 & y_2 & \cdots & y_{M+1} \\ \vdots & \vdots & \vdots & \vdots \\ y_{N-M-1} & y_{N-M} & \cdots & y_{N-1} \end{bmatrix}, \text{ with } M \geq K, N - M > K. \tag{1.25}$$

The dimensions of $\mathbf{H}$ are chosen to make the matrix as square as possible to maximize parameter accuracy. To calculate the SVD of $\mathbf{H}$, Kung's *et. al.* method [53] can be used. The matrix $\mathbf{\Sigma}$ of the SVD of $\mathbf{H} = \mathbf{U}\mathbf{\Sigma}\mathbf{V}^H$, contains the singular values $\sigma_1, \ldots, \sigma_p$, with p being the rank of the matrix. The matrix $\mathbf{H}$ is truncated to rank K:

$$\mathbf{H}_K = \mathbf{U}_K\mathbf{\Sigma}_K\mathbf{V}_K^H \tag{1.26}$$

where $\mathbf{U}_K, \mathbf{V}_K$ are the first K columns of $\mathbf{U}, \mathbf{V}$ respectively and $\mathbf{\Sigma}_K$ is the upper-left $K \times K$ submatrix of $\mathbf{\Sigma}$. Using $\mathbf{U}_K$ the following set of equations is formed:

$$\mathbf{U}_K^{\uparrow} \approx \mathbf{U}_{K\downarrow}\mathbf{Q} \tag{1.27}$$

where the up (down) arrow stands for deleting the top (bottom) row respectively. In the method HSVD [5, 53] an estimate of the matrix $\mathbf{Q}$ is obtained by solving Eq. (1.27) in a least squares sense. The eigenvalues of the latter matrix are the estimates $\hat{z}_k, k = 1, \ldots, K$, of the signal poles. In order to compute the phases, the estimates are backsubstituted in the model equations of Eq. (1.6) and fitted to the original data with a LS method. The HSVD method was improved in terms of estimation accuracy by the Hankel Total Least Squares (HTLS) algorithm [111], which computes the Total Least Squares (TLS) solution of Eq. (1.27). The most important and most time consuming step in the HSVD method is the singular value decomposition, where $\mathbf{H}$ is calculated as the product of $\mathbf{U\Sigma V}^H$. The reason for the computational complexity of this step is that all singular values are calculated. However, because the SVD decomposition is afterwards truncated to rank K, only the first K singular values are relevant and have to be computed. Usually, the number of required singular values K is much smaller than the total number of singular values p, leading to many unnecessary calculations. The calculation of the redundant singular values can be omitted if the Lanczos scheme [68, 17] is used, leading to the faster HLSVD algorithm.

In this thesis the HLSVD algorithm will be used for solvent filtering and not for parameter estimation. To remove residual water and lipid resonances, HLSVD is used as a filter: the signal to be filtered is modeled with K peaks using the HLSVD algorithm. The peaks in between the defined filter region are then subtracted from the original signal resulting in a filtered signal.

Time Series

In a time series experiment, where spectra from a fixed location are acquired at different time instances, parameters between the different spectra can be related. However in the discussed methods it is not possible to include this prior knowledge. By extending the cost function multiple spectra can be processed simultaneously and thus prior knowledge between spectra can be imposed. Suppose S signals are going to be processed simultaneously, the nth point of signal s can be written as follows:

$$\bar{y}_{ns} = \sum_{k=1}^{K_s} a_{ks} e^{j\phi_{ks}} e^{(-d_{ks}+j2\pi f_{ks})t_n} \tag{1.28}$$

The additional parameter refers to the sth signal and K_s denotes the number of peaks in the sth signal. When all S signals have to be processed simultaneously, all signals have to be included in the same cost function:

$$\sum_{s=1}^{S}\sum_{n=0}^{N-1}\left|y_{ns}-\sum_{k=1}^{K_s}a_{ks}e^{j\phi_{ks}}e(-d_{ks}+j2\pi f_{ks})t_n\right|^2 \tag{1.29}$$

Because parameters of different signals are present in the same costfunction, prior knowledge between parameters of different signals can be imposed on top of prior knowledge between parameters within one signal. Using such inter-spectral prior knowledge improves accuracy of parameter estimates [117]. Also black-box methods can be extended for processing multiple voxels simultaneously, resulting in the methods HTLSsum [12] and HTLSstack [116].

The accuracy of parameter estimation is limited. There exists a fundamental lower limit on the accuracy of the parameter estimates that can be obtained by any unbiased estimator. This lower bound is called the Cramér-Rao bound (CRB) Suppose that E is the expected value operator and assume that $\hat{\boldsymbol{\theta}}$ is an unbiased estimator of $\boldsymbol{\theta}$.

$$E(\hat{\boldsymbol{\theta}}) = \boldsymbol{\theta}$$

.

The covariance matrix of $\hat{\boldsymbol{\theta}}$ is defined as

$$\mathbf{P} = E\left((\hat{\boldsymbol{\theta}}-\boldsymbol{\theta})(\hat{\boldsymbol{\theta}}-\boldsymbol{\theta})^T\right).$$

It can be shown [99] that under quite general conditions the following holds

$$\mathbf{P} \geq \mathbf{P}_{CR} = \mathbf{F}^{-1} \tag{1.30}$$

where $\mathbf{F}$ is the Fisher information matrix of $\mathbf{P}_{CR}$ the Cramér-Rao matrix. The elements of $\mathbf{F}$ can be worked out explicitely in the case of white Gaussian noise[113]. This leads to the following expression of the CRB for parameter $\boldsymbol{\theta}_j$:

$$\sigma_{\boldsymbol{\theta}_j} \geq \mathrm{CRB}_{\boldsymbol{\theta}_j} = \sqrt{(\sigma^2\mathbf{J}^T\mathbf{J})^{-1}_{jj}} \tag{1.31}$$

where J is the Jacobian matrix, the rows of which are the first derivative vectors of the components of the signal to the model parameters and σ is the noise standard deviation. $\sigma_{\boldsymbol{\theta}_j}$ is the standard deviation of the estimated model function parameter $\boldsymbol{\theta}_j$.

1.4 Relevance of MRS in clinical applications

Magnetic Resonance Spectroscopy can monitor the metabolism *in vivo* of certain body parts in a non-invasive way. Because most pathologies are characterized by an altered metabolic situation, MRS can be used to diagnose the pathology. The first application of MRS was monitoring energy metabolism in skeletal muscle using ^{31}P [23, 24]. Cardiac spectroscopy was later introduced to differentiate pathogenic from normal tissue [123, 72]. ^{31}P and ^{13}C spectroscopy of the liver was also reported to provide information on changes in high energy phosphate and lipid metabolism in response to disease or cancer. First reported on extracted biopsy specimens, the technique is applied *in vivo* as well [45, 39]. Although these applications are interesting , they did not find their way into clinical practice. Two applications did find their way into clinical practice: ^{1}H spectroscopy of brain and prostate. They will be discussed separately.

1.4.1 Brain MRS

A brain spectrum acquired with a long (270 ms) and short echo time (30 ms) is shown in Figure 1.7. The long echo time spectra contains much less peaks than the short echo time spectrum. At the long echo time most metabolites have already relaxed to their equilibrium state. A second difference is that in the short echo time broad resonances underly the metabolites. These broad resonances originate from macro-molecules and the combination of all these is referred to as the baseline. In a long echo time spectrum no baseline is present because macromolecules have damped out at the time of acquisition.

The figure illustrates the advantages and disadvantages of short and long echo time acquisitions. Short echo time signals contain a lot of information, because the spectrum is rich in spectral peaks. Data analysis can however be disturbed by the baseline and overlapping metabolite peaks. Data analysis of long echo time signals is more straightforward but less metabolic information can be retrieved because less peaks are present. Remark that in both figures the resonance of water is already suppressed and filtered out and that only the metabolic region of the spectrum is shown. In a long echo time spectrum typically the metabolites NAA (N-acetyl-aspartate), Cr (creatine), Cho (choline), Ins (myo-inositol) and Glu/Gln (glutamaat/glutamine) will be present. In short echo time spectra, along with the above mentioned peaks, other peaks will be present such as Ala (alanine), GABA (γ-aminobutyric acid), tau (taurine) and several other metabolites.

The brain is specifically suited for measuring high quality spectra: the brain is highly homogeneous, is not subject to movement and has in a healthy brain only lipids at the edges of the brain. Another reason why brain spectroscopy

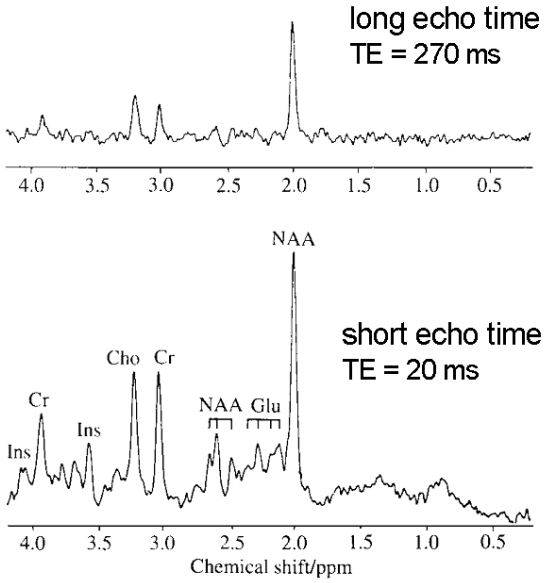

Figure 1.7: Example of a long and short echo time spectrum of the human brain. As can clearly be seen , the short echo time spectrum is much more complex than the long echo time spectrum, which contains much less peaks.

is succesful is that much useful information can be collected. Information on energetic status, biochemical markers and neurotransmitters is present in brain spectroscopy. When a brain disorder is present, changes will appear in the energetic status and in the biochemical markers, and those changes can be detected by MRS. For example, the neuronal marker which has provided the highest diagnostic value has proven to be NAA, which is reduced in stroke, brain tumors, ischemia and degenerative disease. Brain MRS has proven to be useful in a wide range of neurological pathologies. One of the applications where MRS was very useful was in the field of neonatal neurology; both to monitor metabolic changes in the development of the normal child brain, as to identify many neurological disorders [22]. In stroke, ^{1}H MRS has shown differences between normal and acutely infarcted brains: lactate was increased and NAA, creatine and choline levels were decreased in the infarcted areas[31, 57]. Multinuclear MRS has been used to detect and localize metabolic changes associated with seizures [40]. By using the metabolic profile of the epileptogenic lesions, they could be distinguished from other types of lesions.

However the largest application of brain MRS yields the diagnosis, therapy planning and treatment monitoring of brain tumors. Because each type of disease alters the metabolism of the affected cells in a specific way, the spectrum of the lesion will have a characteristic outlook. The idea that different tumor types would have unique metabolic fingerprints was supported by the results of studies of extracts from cultures of various tumor cell lines [34]. Typical alterations in metabolite levels found in cancerous tissue were: NAA and creatine levels are reduced, cholines are increased. Ratios of creatine-to-choline-containing compounds and of NAA-to-cholines are significantly reduced in all tumor types relative to control tissue [14, 64]. Other metabolites were reported to be specific to astrocytomas (lactate) and meningiomas (lactate and alanine)[64] or can be an indicator of the grade of tumor malignancy (lactate in gliomas) [52]. The information provided by MRS is very critical in the diagnosis of brain tumors as was shown in [60]. The study investigated the influence of MRS on diagnosing brain tumors in 16 brain tumor cases. It was found that MRS accurately predicted the pathological nature and clinical outcome in 15 of 16 investigated cases (96%); that it influenced clinical decision making in 12 cases and that it altered surgery planning in 7 patients.

To make MRS part of the diagnostic tools, advanced automatic classification methods were developed. Different approaches led to different success rates. A review on classification methods can be found in [3]. Different methods were applied such as artificial neural networks [76] and support vector machines [30, 62]. Both methods require large sets of previously acquired spectra to train the algorithms. Other methods such as linear discriminant analysis [78] were applied as well.

1.4.2 Prostate MRS

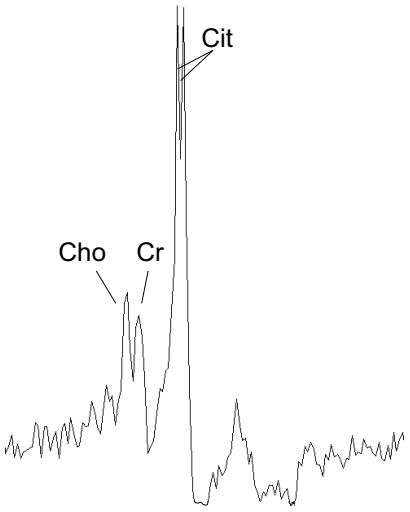

Figure 1.8: Example of healthy ^{1}H prostate spectrum. Three metabolites can be recognized: choline (Cho), creatine (Cr) and the large inner citrate doublet (Cit), the outer doublet of citrate cannot be resolved in this spectrum. The peak heights of choline and creatine to citrate are typical for a healthy prostate spectrum.

The focus of prostate MRS is on prostate cancer, which is very prevalent amongst Western elderly man. Presently the combination of digital rectal examination and prostate-specific antigen (PSA) testing are the principal routine diagnostic procedures. Techniques such as transrectal ultrasound (TRUS) is often combined with histopathological examination of biopsy material. However, taking biopsies involves discomfort for the patient and introduces health risks. Using only imaging techniques as TRUS and MRI the lesion can be visualized, but it is not possible to assess the lesion type: benign (benign prostate hyperplasia, BPH) or malignant (prostate cancer).

Prostate spectra are characterized by the presence of three major metabolites: the singlets of choline and creatine; and the strongly coupled citrate multiplet, which appears as an overlapping doublet of doublets at 1.5T. An example of a healthy prostate spectrum acquired at 1.5T is shown in Figure 1.8

Healthy glandular prostate tissue also demonstrates high levels of polyamines (predominantly spermine), which resonate between choline and creatine, but cannot be completely resolved. Early studies of prostatic biopsy tissue showed

that significant differences exist in the metabolic profile of both tissue types [87]. Within the peripheral zone, regions of prostate cancer demonstrate higher levels of total choline and reduced levels of citrate and polyamines compared to healthy peripheral zone tissues. The increase in choline containing compounds in cancer has been attributed to an increase in cellular proliferation and cell density [21], as well as changes in phospholipid metabolism that result in higher levels of membrane synthesis and degradation products [2, 88]. The decrease in citrate and polyamines in prostate cancer is due to changes in cellular function combined with the replacement of the tissue's characteristic ductal morphology [18].

In vivo spectroscopy of the prostate is however not straightforward because the prostate is not located in a homogeneous environment making shimming not an easy task and the prostate is surrounded by lipids, requiring advanced suppression pulses. Recent studies showed that the assessment of lesion type is feasible *in vivo* [55, 56, 42, 61] by using MRS and an endorectal coil. To be able to estimate the spatial extension of the lesion, MRSI has been used to obtain metabolite maps over the entire prostate gland [55, 109, 54] and was compared with sextant biopsy localization [119]. To make the quantification of the citrate multiplet more easy, the echo time parameter of the pulse sequence is optimized to minimize the outer peaks from the citrate multiplet [121, 108]. Citrate is an J-coupled AB spin system which exhibits a large doublet of inner peaks and a doublet of outer (smaller) peaks.

1.5 Chapter by chapter overview

This thesis deals with several methods to quantify MRS data in an accurate way. After an introduction into the basic MRS principles, an overview of the several preprocessing steps and of frequency and time-domain quantification methods was given. The clinical relevance of MRS in the diagnosis and therapy monitoring of brain and prostate tumours is illustrated.

Chapter 2 concerns the comparison of two different quantification methods: a frequency domain peak integration and a time-domain modeling algorithm. The methods are compared in their performance of the quantification of prostate MRS data. The comparison is done using Monte Carlo simulations of different types of prostate spectra, using phantom and *in vivo* prostate data. The weak and strong points of both methods will be outlined. The way of choosing the model order for the time domain method gets some specific attention. To conclude, a graphical user interface for processing prostate MRSI data is presented.

Chapter 3 introduces a new multivoxel quantification algorithm which was extended with an FIR filter. The algorithm is applied for the first time to MRSI

data. Aspects of prior knowledge for multivoxel processing will be highlighted and the influence of multivoxel processing on the accuracy of the parameter estimation is shown. The difficulty in automated MRSI quantification is the model order which has to be chosen. The influence of overmodeling and undermodeling the spectra will be treated. The increased robustness of the proposed algorithm is shown in the quantification of *in vivo* MRSI data.

The fourth chapter derives a novel 2 step algorithm AQSES$_{2step}$ from the AQSES algorithm, for quantification of short echo time spectra which estimates the spectrum as a linear combination of measured model spectra in which corrections to frequencies, dampings and phases are optimized. The acquisition of the model spectra database is discussed. By investigating the influence of the model order on the performance of AQSES, the 2 step algorithm is justified. The proposed baseline handling using splines was tested using Monte Carlo simulations. To conclude, the proposed method was applied to 50 *in vivo* short echo time spectra.

Chapter 5 summarizes the conclusions and outlines suggestions for further research.

1.6 Conclusion

This chapter introduces MRS as an application of MR. The basic principles of MR and MRS techniques were outlined, together with a description of the acquired MRS spectra. To continue, a brief overview is given of the existing methods of preprocessing the data. Different frequency and time domain quantification algorithms are introduced next. The concept of prior knowledge was illustrated and the relevance of MRS in a clinical environment was shown. To conclude this introduction a chapter by chapter overview of this thesis was provided.

Chapter 2

Comparing Time Domain Fitting With Frequency Domain Analysis on prostate MRSI Data

In this chapter two quantification methods are compared in quantifying prostate spectra. The first method is based on the parametric modeling of the time domain signal, the second is based on a frequency domain peak integration algorithm. After an outline of both methods, they are compared using Monte Carlo simulations, phantom and in-vivo data. Because the determination of the diagnostic ratio of Choline+Creatine+Polyamines to Citrate is crucial in the diagnosis of prostate cancer, the comparison is based on the estimation of this ratio. This chapter will point out strong and weak points of both methods, as well as some time domain method problems related to choosing the model order. To conclude the chapter, a graphical user interface is presented in which the time domain method is implemented.

2.1 Introduction

Because of the diagnostic value of MRS of the prostate, the development of mathematical routines for reconstructing and correcting 3D-MRSI data is important for quantifying the metabolic content of the tissue of interest. Time and frequency domain based methods to extract quantitative information from

spectral data were introduced in the previous chapter. In the time domain approaches, the k-space array of free induction decay (FID) signals are discrete Fourier transformed to reconstruct their spatial distribution. The resulting spatial array of FIDs is then analyzed on a voxel-by-voxel basis using different time domain approaches. Frequency domain processing methods apply both k-space and time domain Fourier transforms to provide a spatial array of spectra which are further analyzed in the frequency domain. Several studies have been conducted to compare different time and frequency domain based approaches for the analysis of ^{13}C spectra from liver [74], ^{31}P spectra from rat tumors [104], and ^{1}H spectra from blood plasma [103], brain [47, 33, 70], and brain simulations [25].

The strongly overlapping choline, creatine, and polyamine peaks and the citrate multiplet observed in prostate ^{1}H spectra pose a new and unique challenge for time and frequency domain fitting methods. In this chapter the results are presented of the comparison of two spectral data processing approaches that have been used for clinical data processing: a time domain fitting (TDF) approach based on the AMARES$_f$ algorithm[115, 100]; and an automated frequency domain analysis (FDA) procedure [71]. These were evaluated in terms of the accuracy of parameter estimates for choline, creatine, and citrate. The analysis included Monte Carlo simulations, empirical data from phantoms, and *in vivo* data from prostate cancer patients.

The results presented here were obtained in a close collaboration with the Department of Radiology of the University of California, San Francisco (UCSF). The group is lead by Prof. Dr. Sarah Nelson and Prof. John Kurhanewicz and is highly specialized in MRS acquisition and processing. The FDA method here described is developed at that laboratory and is used there on a daily basis. Esin Ozturk and Mark Swanson, both at the UCSF, were closely involved in the collaboration.

2.2 Methods

2.2.1 Simulations

Spectra representing a phantom solution, healthy peripheral zone tissue, mixed tumor and healthy peripheral zone tissue, moderately aggressive and very aggressive tumors were simulated using a sum of K decaying exponentials as shown in equation 1.6. The formula is repeated here for clarity:

$$\bar{y}(t_n) = \sum_{k=1}^{K} a_k e^{j\phi_k} e^{(-d_k + j2\pi f_k)t_n} \tag{2.1}$$

($*10^6$)	Cho	polyamines	Cr	Cit(1)	Cit(2)	Cit(3)	Cit(4)
phantom	2.3	0	1.8	0.6	4.4	4.4	0.6
normal	2.3	4.0	1.8	0.6	4.4	4.4	0.6
mixed	3.3	1.0	1.8	0.3	2.4	2.4	0.3
moderate tumor	3.3	1.0	1.6	0.2	1.2	1.2	0.2
aggressive tumor	4.3	0	0.2	0	0.2	0.2	0

Table 2.1: Amplitude values (arbitrary units) of the different type of simulated prostate signals.

where y_{t_n} is the nth point of the simulated signal. Parameters a_k, f_k, d_k and ϕ_k denote the amplitude, frequency, damping and phase of the kth resonance. The dampings and frequencies were selected based upon *in vivo* prostate data acquired at 1.5T.

Citrate was modeled as 2 large center peaks and 2 small side peaks to mimic its spectral appearance at 1.5T and TE = 130 ms. Choline, creatine and polyamines were modeled as single resonances. All peaks had a damping of 2 Hz except for polyamines which had a damping of 8 Hz. The levels of choline, creatine, citrate and polyamine resonances corresponding to each of the five different spectral patterns are shown in Table 2.1. The amplitudes were determined visually to correspond with the typical spectral patterns. Four levels of random white noise with Gaussian distributions were selected to produce SNR of 170, 35, 15.5, and 10 for the choline peak of the simulated normal spectrum. Signal-to-noise ratio was defined as the height of the choline peak divided by the standard deviation of the noise in the frequency domain. Figure 2.1 shows the original noiseless spectra for each of the five different cases, along with the spectra containing the minimum and maximum levels of noise. Two hundred realizations of each noise level were added to each of the five model functions.

The time and frequency domain analysis methods were applied to calculate the ratio of (choline+creatine+polyamines) to citrate (CCP/C). The accuracy of the ratio estimates was compared for the simulations using the calculated relative root mean square error (RMSE) and relative bias, which are defined by:

$$\begin{aligned} \text{Relative RMSE ratio} &= 100\sqrt{\frac{1}{L}\sum_{l=1}^{L}\frac{(\text{ratio}_{ex}-\text{ratio}_l)^2}{\text{ratio}_{ex}^2}} \\ \text{Relative bias} &= 100\frac{\text{ratio}_{ex}-\frac{1}{L}\sum_{l=1}^{L}\text{ratio}_l}{\text{ratio}_{ex}} \end{aligned} \tag{2.2}$$

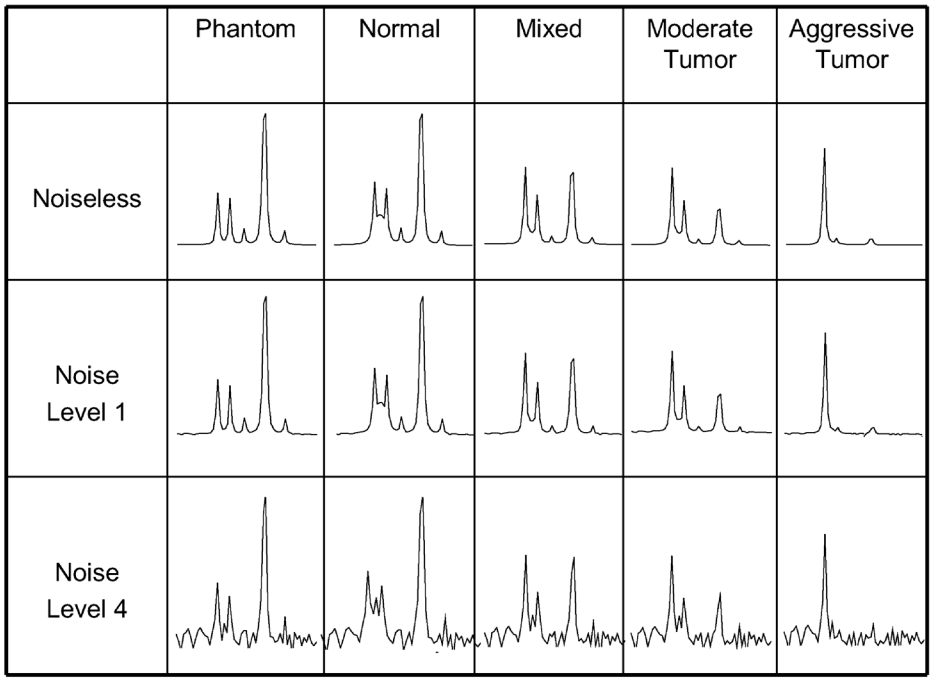

Figure 2.1: The 5 different spectral types used in the Monte Carlo simulations, each shown with no noise added (upper row), the lowest noise level added (middle row) and the highest noise level added (bottom row)

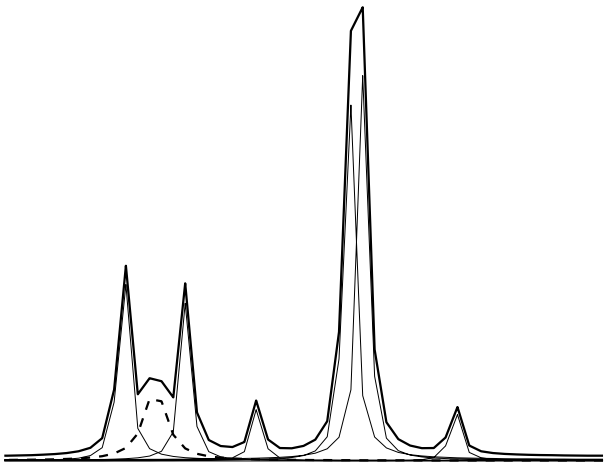

Figure 2.2: A normal tissue simulated spectrum shown in detail: the upper thick line represents the total spectrum, the individual resonances are drawn in thin lines. The resonance of the polyamines, which has a larger linewidth than the other resonances, is drawn dashed. The overlap between choline, creatine and the polyamines can clearly be seen.

where ratio_{ex} is the exact ratio of CCP/C, and ratio_l is the estimate of the ratio for simulation signal l. Monte Carlo analysis was applied to evaluate the relative RMSE, relative bias and standard deviation of the CCP/C ratio estimation for each of the five model functions.

2.2.2 Phantom and *in vivo* Data Acquisition

A phantom solution was prepared to approximate the normal concentrations of the major prostate metabolites choline (4 mM), creatine (30 mM), and citrate (132 mM), and was placed into a 560 ml plastic spherical container. Both phantom and *in vivo* MR studies were performed on a 1.5 T GE Signa clinical MR scanner (GE Medical Systems, Milwaukee, WI) using the body coil for excitation and a combined endorectal/pelvic phased array coil system for signal reception (Medrad, Pittsburg, PA). For phantom studies, the sphere was placed directly on top of the endorectal coil and surrounded by saline bags inside a specially designed box, above and below which the pelvic phased array coils were placed. Informed consent was obtained from nine human subjects prior to undergoing MRI/3D-MRSI staging examinations.

The imaging protocol included a sagittal scout, followed by axial T_1-weighted spin echo images (TR = 600ms, TE = 12 ms, 4 mm thick, 1 mm gap, 2 NEX, FOV = 14 cm, 256 $\times$ 192 matrix) for human subjects, and axial T_2-

weighted fast spin echo images (5000-6000/108 ms effective, 3 mm thick, no gap, 3 NEX, FOV = 14 cm, 256 × 192 matrix) for both human and phantom studies. For phantom studies, a 50 × 30×30 mm (R/L×A/P×S/I) PRESS volume was prescribed using the axial T_2 weighted images and placed as close as possible to the endorectal coil while avoiding the edges of the sphere. For *in vivo* spectroscopy, the PRESS volume selection was prescribed using the axial T_2 weighted images to encompass as much of the prostate as possible while excluding periprostatic lipids and the rectum. Water and lipid suppression were achieved using the BAnd Selective INversion with Gradient dephasing (BASING) technique [98]. Spatially selective saturation pulses were employed to eliminate signals from regions outside the phantom, or from periprostatic lipid contamination and susceptibility-induced artifacts caused by the air-tissue interface of the rectum [98]. The data were acquired using 3D phase encoding on a $16 \times 8 \times 8$ matrix at a nominal spatial resolution of 0.34 cm^3, with TR/TE = 1000/130 ms, and a total acquisition time of 17:08 minutes.

2.2.3 Phantom and *in vivo* MRSI data reconstruction

The phantom and *in vivo* data were first processed using voxel shifting and 3D Fourier transforms to generate arrays of spatially localized time domain signals centered upon the PRESS selected volume. These data were further analyzed with time domain apodization, followed by Fourier transformation and automated phasing to generate 3D arrays of spatially localized spectra that could be directly correlated with the anatomical images.

A total of 72 voxels from within the PRESS box were selected from the phantom data. The arrays of human spectra were compared with the anatomical images and 72 voxels were identified from the peripheral zone and central gland that had good SNR and were free of lipid contamination. Time domain signals corresponding to the phantom and human voxels were extracted to provide test data for the two analysis methods. For one *in vivo* study, a 2D array of data was selected from an *in vivo* MRSI dataset that contained both tumor and normal tissue.

2.2.4 Time domain processing

The MRSI data were transformed from k-space to the spatial domain, leaving the time direction unaffected. To achieve estimates of the amplitudes, frequencies, dampings and phases of the different resonances in the spectra, the signals were modeled in the time domain, with the model function as described in Eq. 1.6. The algorithm AMARES$_f$ [115, 100] was used to find the optimal estimates of the amplitudes, frequencies, dampings and phases of the original. As was shown in section 1.3.3, a FIR filter was included in the minimization process to eliminate any residual water and lipid that could be present in the

signals.

The algorithm allowed the inclusion of prior knowledge on the parameters. The AMARES$_f$ algorithm requires starting values for the estimates of the frequencies, dampings, and overall phase. Starting values for the frequencies were chosen as follows. First, initial estimates of frequency starting values were assessed visually from a reference spectrum. Next, the initial estimates were corrected for frequency shifts using the position of the water resonance from the same spectrum, since the difference in frequency between water and the metabolites of interest remains fairly constant. The starting value of the overall phase was given by the angle of the first complex data point of each signal, and the starting value for the damping was always 2.13 Hz. The algorithm also allowed the definition of upper and lower limits on the estimated parameters. Besides natural constraints, such as the amplitudes and dampings being positive, the boundaries of the frequencies were chosen in between the starting values of the different peaks, so that a peak in the spectrum would not be fitted by a neighboring peak in the model.

Model functions for the simulations

The simulations were required to model all of the peaks present in the spectrum including single peaks corresponding to choline, creatine, and polyamines, and four peaks corresponding to citrate. The following constraints were imposed on the estimated parameters:

- shifts between the estimated frequencies of the citrate multiplet were fixed such that the frequency difference between the outer peaks and the inner peaks was 15 Hz and the frequency difference between the inner doublet peaks was 2.54 Hz;
- the amplitudes of the outer lobes of citrate were equal, as well as the amplitudes of the inner doublet peaks;
- dampings of all peaks except polyamines were set to be equal.

The presence of polyamines in the model spectra caused a large error in the estimation of damping and amplitude for choline, creatine, and citrate, due to their overlap with both choline and creatine, and the lack of a priori knowledge of the linewidth. This was confirmed by calculating the Cramér-Rao lower bounds (CRB) on the parameter estimates for a 6 and 7 peak model. The CRB indicates the best possible accuracy of an estimate for any unbiased estimator (see also under section 1.3.3). The CRB on the relative RMSE of the CCP/C ratio increased with 11% (normal) or 81% (phantom) when polyamines were included in the model. Based on the results of the CRB analysis, the simulated signals were processed using a 6 peak model, including choline, creatine, and

4 citrate peaks. The choline and creatine were modeled more accurately using the six peak model, leaving the polyamines behind in the residue. Only the first 256 points were used in the minimization problem. A stopband FIR filter was applied to the signals prior to fitting in order to eliminate the effect of the residual water resonances.

The influence of fast T_2 decaying resonances, like polyamines, in the signal can be lowered by deleting the first data points of the time domain signal, beyond which they are largely damped out. Polyamines were present in the simulation of the normal case, so the first few points of the time signal were deleted to improve the quantification. It was found that deleting 9 points resulted in the most accurate estimate of the CCP/C ratio. The number of points that resulted in the minimum error was found by balancing two counteracting mechanisms, the reduction of the bias due to decreasing the influence of polyamines, and the increase in the relative standard deviation due to dismissing the points with the most energy.

Model functions for the Phantom

For the phantom containing only choline, creatine and citrate metabolites, the spectra were initially modeled using only 4 peaks. The outer peaks of the citrate were not included in the model because they should have been nearly invisible due to the spectral modulations of citrate at the given echo time [69, 86]. However, the time domain method systematically overestimated the (choline+creatine)/citrate (CC/C) ratio in that case, due to lower amplitudes of citrate. CC/C ratio was estimated more accurately when the outer peaks of citrate were included in the model function. The results presented and compared below are based on modeling the signal with a 6 peak model function that included the outer peaks of citrate. The total citrate amplitude was calculated as a sum of the four citrate peaks. A stopband FIR filter was included in the fitting procedure order to improve water suppression.

Model functions for the *in vivo* Data

A four peak model, including only choline, creatine and the inner citrate doublet peaks, was also used for *in vivo* processing for the following reasons. First, including polyamines and the outer wings of the citrate degraded the robustness of the method. This was mostly due to the fact that the polyamines were highly overlapping with choline and creatine, and that they had a damping which could not be linked to the other peaks by means of a priori knowledge. Additionally, polyamines and the outer wings of citrate were very small for the *in vivo* case. This was confirmed by the fact there was no residue present from outer wings of the citrate or polyamines in the residual signal for the time domain modeling with 4 peaks. A passband filter that coincided with the metabolite region was also chosen for filtering the *in vivo* data. The filter passband was 1.9 ppm wide

and was positioned to eliminate the residual water and lipid resonances outside the metabolite region at the same time.

2.2.5 Frequency Domain Analysis

The frequency domain analysis method (FDA)[71] used in this comparison was an automated procedure composed of routines for reconstruction and correction of the spectral data for frequency, phase and baseline distortions, and final estimation of the parameters for the peaks of interest. Amplitudes of the different resonances were estimated by integrating defined areas of the spectrum. The analysis was initiated by apodizing the FIDs in the time domain with a Gaussian filter of 1 Hz, followed by fast Fourier transformation (FFT) from the time to the frequency domain. Data acquisition parameters were extracted from the header of the reference MR images for accurate registration of the spectra to the anatomical images and for correct interpretation. Discrete Fourier transformation (DFT) was applied to the data to generate a 3D array of spectra on a rectangular grid based on the coordinate system of the reference anatomical images. The center of the grid was spatially shifted to reduce the partial voluming effects around the edges of the excited region and to maximize the full tissue voxels.

Frequency shifts were corrected for each spectrum based on a peak descriptor file, which included the expected locations and linewidths of water, choline, creatine, and citrate peaks. Separate peak descriptor files for the phantom and *in vivo* cases were established by inspecting several empirical phantom and human prostate spectra, respectively. The peak file that was used for the simulated data was generated to match the peak locations of the simulations. A statistical peak finding routine was applied to the magnitude data [71] to locate the frequencies of each peak of the spectrum. The frequency shift for each peak was estimated as the difference between the peak location found by the algorithm and the location given in the peak descriptor file. The mean of the frequency shifts of all the peaks was applied to the spectrum as the estimated frequency correction. The automatic phase correction algorithm was used to find the value that maximized the area of the real part, while minimizing the area of the imaginary part of the spectrum. Baseline removal routines assumed that the spectra were a sum of the peaks, baseline, residual water, and random noise, and iteratively separated these components. The algorithm isolated the data points that corresponded to the spectral peak regions by using the locations and linewidths given in the peak descriptor file at the first iteration. Variations of the peak parameters for the given data were inspected, and used for further iterations.

After the baseline correction, peak locations and heights were determined by searching for a maximum in each of the peak regions. Peak areas were calculated by integrating over the peak regions given in the peak descriptor file in the

real part of the spectrum. Choline, creatine, and polyamines were not resolvable due to spectral overlap, and their area sum was calculated by integrating over their combined region.

2.3 Results

2.3.1 Simulations

Relative RMSE, and bias calculations were used to compare the accuracy of time and frequency domain methods for the CCP/C ratio estimations of the simulated signals. The FDA method was unable to estimate separate levels of choline, creatine, and polyamines due to the overlap of these three peaks, whereas the TDF method required the exclusion of polyamines to reduce the error as described in the Methods section. Although the two methods did not effectively estimate the same ratio, the comparison was still possible within their limitations. The relative RMSE and biases for the five different simulation signals are presented in Table 2.2.

It should be noted that the standard deviation of the different noises did not increase linearly over the four different noise levels. Both FDA and TDF methods resulted in stable ratio estimates for the mixed, normal, phantom, and tumor cases. The maximum relative RMSE increase was 7.79% for TDF, and 12.35% for FDA as the SNR decreased for these four cases. Small amounts of citrate were present in the aggressive tumor spectrum simulation, leading to almost zero estimates for citrate and forcing the ratios to extremely large numbers. Ratios were withheld if their absolute values were larger than 150 to prevent the distortion of the RMSE and bias calculations. The TDF algorithm did not converge for a few voxels, resulting in zero amplitude estimates for all of the peaks, and undefined ratio. Those results were also excluded from the analysis. The exclusion of results was only necessary in the aggressive tumor case, and 0, 7, 7, and 15 results out of each of the 200 iterations were withheld from the statistical analysis for the four different noise levels respectively. Table 2.2 shows that the TDF method was more accurate in four of the five simulated signals, specifically, the aggressive tumor, mixed (tumor and normal), phantom, and moderately aggressive tumor cases.

When nine initial data points were deleted (to decrease the influence of polyamines), the relative RMSE of the TDF method for the normal spectrum decreased to 17.7%,18.7%,18.8%, and 20.4% for the four different noise levels respectively, resulting in more accurate estimates at the first, third, and fourth noise levels than the FDA method.

2.3.2 Phantom

Table 2.2: **Relative RMSE and relative bias of Monte Carlo simulations**

		Relative RMSE (%)			
		noise 1	noise 2	noise 3	noise 4
Aggressive Tumor	TDF	7.66	24.14	54.29	303.69
	FDA	44.79	250.27	282.50	225.29
Mixed	TDF	8.77	9.30	10.69	12.53
	FDA	12.15	12.88	13.99	16.33
Normal	TDF	26.58	26.75	27.06	27.43
	FDA	18.31	18.40	21.56	24.22
Phantom	TDF	0.50	2.45	5.38	8.29
	FDA	9.07	9.59	11.30	13.66
Moderate Tumor	TDF	8.90	10.01	12.90	16.67
	FDA	11.49	13.05	16.61	23.84
		Relative bias (%)			
Aggressive Tumor	TDF	6.32	10.33	14.49	2.46
	FDA	-39.80	-52.37	41.22	79.34
Mixed	TDF	8.75	8.96	9.19	9.39
	FDA	12.14	12.49	12.15	12.28
Normal	TDF	26.58	26.71	26.86	26.96
	FDA	18.31	18.32	21.07	23.43
Phantom	TDF	0.11	0.26	0.37	0.33
	FDA	9.05	9.14	9.34	9.42
Moderate Tumor	TDF	8.87	9.13	9.34	9.65
	FDA	11.41	11.77	10.10	8.79

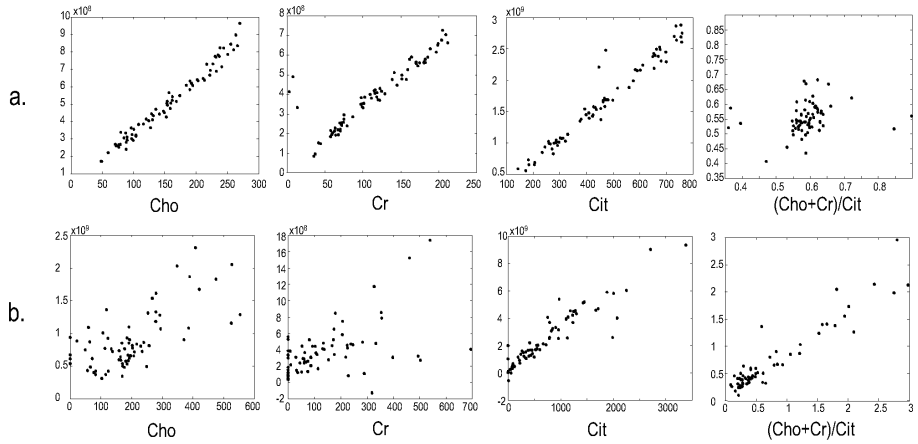

Figure 2.3: (a) Scatter plots of choline, creatine, citrate, and CC/C ratio calculated from TDF versus FDA methods for the 72 phantom voxels. (b) Scatter plots of choline, creatine, citrate, and CCP/C ratio calculated from TDF versus FDA methods for the 72 *in vivo* voxels

The first three plots of Figure 2.3(a) show the choline, creatine and citrate estimates acquired using the TDF method versus the FDA method. The Spearman rank correlation coefficients were calculated to determine the association between the amplitude and area estimates of the time domain fitting and frequency domain analysis methods. The Spearman rank correlation coefficients were 0.99 for choline, 0.89 for creatine, and 0.97 for citrate estimates, each with a p value of < 0.05. The results of the two methods were in good agreement both visually and statistically. If both methods were to estimate the CC/C ratio of 0.5 perfectly for all voxels, the correlation plot would have had only one point at the value of (0.5,0.5). Instead, a cloud of points with center $(0.59 \pm 0.074, 0.55 \pm 0.049)$ that corresponded to the means of the TDF and FDA estimates was observed. The distribution of the estimates for the different voxels is illustrated in Figure 2.4.

Both methods overestimated the CC/C ratio. In 3 voxels the time domain fitting failed to include the creatine peak, resulting in a lower estimate of the ratio (voxels 41 to 43). Two other outliers were due to a phase artifact present in the citrate doublet, leading to an incorrect estimate for the citrate resonance by the TDF method.

The effect of acquisition errors on the overall phantom error estimation was investigated by examining the difference between the error arising from empirical

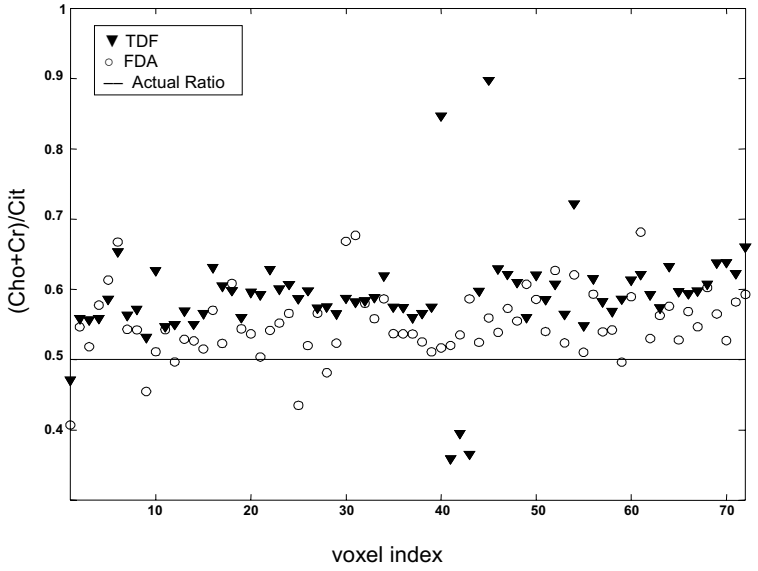

Figure 2.4: CC/C ratio estimates of the two methods for the 72 phantom voxels

phantom data and quantification errors from Monte Carlo simulations of the phantom spectra. Total signal-to-noise ratio (TSNR), which is defined as the ratio of the sum of the peak heights and the standard deviation of the noise, of the phantom spectra had a mean value of 56.35 and a standard deviation of 20.40. To have a consistent set for comparison, 15 phantom spectra were selected having a TSNR between 50 and 60, with a mean of 54.26 and a standard deviation of 2.72. The relative RMSEs were calculated for those 15 spectra with respect to the theoretical value of the ratio of 0.5, giving values of 19.39% for the TDF method and 15.77% for the FDA method. The RMSE results were an estimate of the total acquisition and processing errors. An estimate of the quantification errors was approximated by using the relative RMSE of the phantom Monte Carlo simulations for the given TSNR of 54.26, which was 5.15% for the TDF method and 7.62% for the FDA method. These results are summarized in Table 2.3.

2.3.3 *In vivo* Data

TSNR=54.26	Rel RMSE	
	phantom simulations	phantom data
TDF	5.15%	19.39%
FDA	7.62%	15.77%

Table 2.3: Comparison of relative RMSE for phantom simulations and empirical data

The estimates of the areas and amplitudes of the different metabolites were more difficult to evaluate for *in vivo* voxels due to the lower signal to noise ratio of the data. This was reflected as an increase in the difference of the estimates that were calculated by the two methods, as shown in Figure 2.3(b). The Spearman rank correlation coefficients were smaller for the *in vivo* metabolite estimates than for the phantom case, specifically, 0.59 for choline, 0.51 for creatine, 0.94 for citrate, and the coefficient for the ratio was 0.8. All of the correlations were significant with $p < 0.05$. Figure 2.5 shows the estimated ratios for all of the selected *in vivo* voxels. The time domain fitting failed to converge to a solution in one voxel, yielding zero estimates for all amplitudes. The estimated ratios for both methods for all voxels are shown in Figure 2.5.

Based upon 3D-MRSI data acquired from thousands of patients, various CC/C thresholds have been used clinically to distinguish normal, probable tumor, and definite tumor. Such CC/C thresholds are arbitrary and can be changed to meet different clinical demands of sensitivity and specificity. Typically, a CC/C ratio < 0.5 indicates normal healthy metabolism, a CC/C ratio between 0.5 and 0.86 indicates possible or probable cancer, and a CC/C ratio > 0.86 indicates cancer. For the current analysis, a threshold CC/C ratio of 1 (horizontal dashed line on Figure 2.5) was chosen to select only voxels in the clear-cut cancer range. Both time and frequency domain methods predicted the same voxel condition for 94% of the voxels (68 out of 72). The TDF method estimated the damping (or linewidth in the frequency domain) of each of the peaks, which indicated the quality of the shimming. The mean value of the dampings was 18.8 Hz with a standard deviation of 9.3 Hz.

2.3.4 Case study

Figure 2.6 illustrates frequency domain versus time domain fitting using a two dimensional spectral array (slice) from a 3D-MRSI exam. The T_2 weighted image (a) and corresponding spectral array (b) show a region of mixed cancer and normal peripheral zone tissue on the right side of the gland (left side of image/array), and a region of very aggressive cancer on the left side of the gland (right side of image/array). The results of the time domain fitting for all voxels in one slice of an *in vivo* study are shown in Figure 2.6(c). The residual signals, which are shown in 2.6(d), are the difference of the original signals and

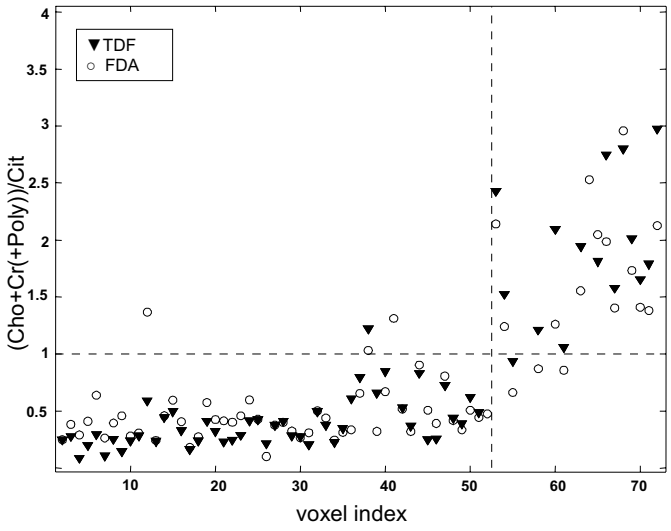

Figure 2.5: CCP/C ratio estimates of the two methods for the 72 *in vivo* voxels. The horizontal line indicates CCP/C=1, which was chosen as the threshold to discriminate between the healthy and tumor spectra. The vertical line divides the voxels coming from a tumor region and those from healthy voxels

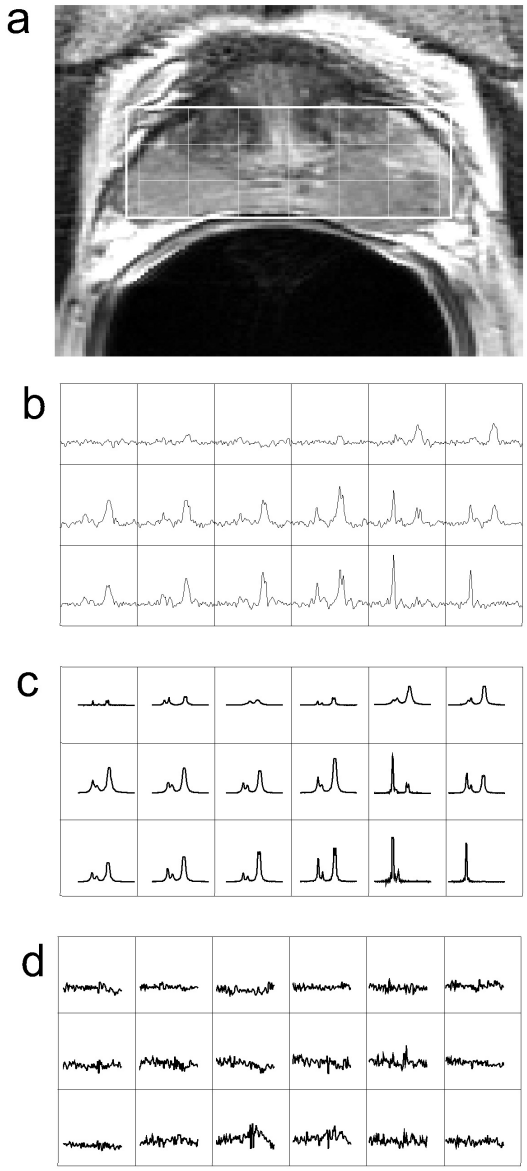

Figure 2.6: (a) Axial T_2 weighted image of the prostate with superimposed position of the voxels within the PRESS box. (b) Spectra from within the PRESS box after FDA method's prepreprocessing. (c) Estimated fits of the spectra produced by the TDF method (d) Residual difference between the original spectra (not shown) and the estimated spectra in (c).

the model signals fitted by the TDF method without any line broadening filter. The spectra shown in 2.6(b) were obtained after the preprocessing FDA steps described in the Methods section, and were also used for the area integration part of the frequency domain analysis.

2.4 Discussion

2.4.1 Simulations

The RMSE of the estimation of the CCP/C ratio for the simulated prostate spectra was mainly due to the bias error in both methods as is shown in Table 2.2. Both methods underestimated the ratio that caused the bias, but for different reasons. Underestimation was caused by leaving the polyamines out of the ratio calculation for the TDF method. The error increased with the amplitude of the polyamines, as indicated by the higher relative RMSE error of the TDF method in tumor or mixed signals compared to the phantom signal, which did not contain polyamines. Even when the polyamines were omitted, the TDF method provided more accurate ratio estimates than the FDA method in all cases except for the normal simulation signal. Underestimation of the ratio for the FDA method can be explained as follows. The FDA method integrated pre-defined areas under the peaks, which might have excluded some of the peak tails. The baseline removal algorithm may also have marked parts of the peak tails as a part of the baseline and reduced their amplitude.

The negative influence of polyamines can be reduced by deleting the initial data points in the TDF quantification process. However, this method is only useful when applied to spectra that contain polyamines; otherwise, the relative RMSE would increase due to the reduction of the overall SNR. The bias and RMSE were relatively high in the aggressive tumor simulations due to the low citrate values in the denominator of the estimated parameter, but were not representative of the method's ability to differentiate tumor spectra. While this would have been of concern if the objective had been to get a precise estimate of the CCP/C ratio, the key to identifying tumor tissue was to know whether the ratio was greater than a given (normal) threshold and the methods used were successful in that regard.

2.4.2 Phantom data

The analysis and quantification were more complicated for the phantom data compared to the simulations. Simulated signals were ideal, with all Lorentzian peaks and Gaussian noise. Acquisition artifacts, such as the lineshape or phase distortions and relaxation time effects, were also absent in the simulated data. The comparison of the two methods using the empirical phantom data gave an

idea of the combined acquisition and quantification errors. The mean values of the CC/C ratio estimates of the TDF and FDA methods were both higher than the actual value, indicating that both methods tended to overestimate the ratio. The variance of the estimates for TDF and FDA methods were 0.074 and 0.049 respectively, which were high due to the acquisition related errors. The relative RMSE of the ratio estimates for the simulated and empirical phantom data are compared in Table 2.3 for the two methods. The RMSE error was greater for the TDF method compared to the FDA method, indicating that the TDF method was more sensitive to the errors induced by the data acquisition.

2.4.3 *In vivo* data

It was noted that the correlation coefficients for the estimates of the metabolites were smaller, while the correlation coefficient for the ratio was larger for the *in vivo* than the phantom case. This was due to the fact that there was a larger variance in the ratios present in the *in vivo* dataset. The type of tissue within the voxel was clearly reflected in the ratios calculated by both methods. A higher ratio was estimated for twenty voxels containing tumor, which are located on the right side of the vertical dashed line in Figure 2.5.

2.4.4 Case Study

A visual interpretation of the fits of the TDF method showed that they represented the original signals well. Some of the residues showed parts of peaks that were not accounted for in the modeled fit. This was due to the modeling errors, coming from the deviations in the spectra from the model function. As described in the previous section, the ratios can be used for discriminating healthy from tumor spectra. Comparing the ratios predicted by the TDF and the FDA, the methods predicted the same spectrum type in 17 out of the 18 voxels (94.4%). Only the voxel in the top left corner was predicted 'healthy' by the TDF method and 'tumor' in the FDA method, and it was difficult to predict the condition of this voxel due to the low signal to noise ratio in that particular voxel.

2.4.5 TDF versus FDA

Simulations showed that the TDF method was able to make more accurate estimates than the FDA method for the ratio when spectral peaks were well resolved and the contribution of the underlying polyamines was relatively small. In this case, the TDF method was able to give individual estimates for different peaks of choline, polyamines and creatine, where the FDA method was only able to estimate the sum of the areas under the three peaks. The TDF method was however sensitive to distortions in the lineshape of the resonances and other

acquisition induced distortions, which can cause errors on estimates as well as to non convergence of the algorithm. The FDA method is less sensitive to data acquisition problems, and will result in a robust estimate for almost any types of spectrum. Both methods were able to deal with frequency shifts, but handle them differently. For the TDF method, starting values were supplied, which were corrected for frequency shifts using the position of the water peak. After that the algorithm automatically searched for the optimal position of the peaks, taking a priori knowledge into account. The FDA method also used a frequency alignment procedure based on the position of the water resonance, but in some cases manual correction of the peak locations were applied needed to achieve more accurate area estimates, because frequency shifts affected the estimates due to the integration of predefined areas. Although both methods estimated the phases automatically, further manual phase corrections were sometimes needed in the FDA based upon manual inspection of the data.

2.5 Clinical Application

The clinical reality of the application of MRS in the prostate is unfortunately more complicated than described above. The examination of a prostate gland harboring cancer is not a clearly defined problem.

Pathologies such as prostatitis, Prostatic Intraepithelial Neoplasia (PIN) can also produce high serum prostate-specific antigen (PSA) concentrations, almost similar abnormalities on T_2-weighted MR-images and MRS. Furthermore, in many patients there is association of different disease processes in the same gland. The ultimate challenge of new techniques as MRS is to distinguish benign from malignant lesions with high predictive value. Unfortunately, with current techniques and metabolites measured, there is spectral overlap in different disease processes. The presence of chronic prostatitis, for example, can show metabolic abnormalities resembling prostate cancer (false-positive diagnosis) [91]. On the other hand, it has become clear from recent studies that the spectrum of well differentiated carcinomas is similar to that of normal glandular tissue of the prostate (false-negative diagnosis).

Theoretically, MRSI could be indicated for the evaluation of prostate cancer in many ways, in particular in diagnosis, therapy-planning, and follow-up after treatment. MRSI-based estimation of the volume of prostate cancer [89], evaluation of the location and size of the cancer for planning external beam radiation therapy [15] or brachytherapy, and evaluation after hormonal therapy or permanent prostate seed implantation [75] were reported recently. At present, most often MRSI is performed as a 'problem-solver' when other diagnostic tools have failed to ascertain the diagnosis in men with high serum-PSA-concentrations and repeatedly negative prostate biopsies. Biopsies cause intraglandular hem-

orrhage which is known to decrease the spectral quality predominantly within the first 8 weeks after biopsy [82].

For MRSI of the prostate to become a more widely applicable diagnostic tool, the possibility of standardization should be investigated. Nowadays, most clinical centers with prostate MRSI know-how are using home-tailored acquisition sequences, which hampers standardization. The knowledge of particular acquisition sequences and the optimal planning of an MRSI experiment are essential prerequisites to produce reliable MRSI data with clinical relevance for diagnosis and further therapeutic management. A single-center study of a standardized evaluation system for prostate MRSI yielded good accuracy and excellent interobserver variability [46]. However, this conclusion should not be extended to a larger scale. Indeed, potential users have MR-equipment of different manufacturers with a wide range of field strengths and sequences. Furthermore, and probably of larger importance, the experience of positioning the endorectal antenna and of planning the measurements is of utmost importance. All these factors influence the interobserver variability and this should be further investigated in large scale multicenter studies.

2.6 A JAVA GUI for prostate CSI processing

The major drawback for MRSI to become of practical use in a clinical environment is that often no means of processing and visualizing the information present in the MRSI data are available. This information should however be easily accessible by radiologists. More and more, MR scanners offer basic tools for the visualization and processing of MRS data. Nevertheless, these tools do not incorporate the latest state of the art preprocessing and quantification algorithms and most CSI processing is therefore done offline on a stand-alone workstation. An MRSI data processing tool should combine advanced signal processing with a clear and easy-to-use visualization of the quantification results.

A graphical user interface was designed to process CSI datasets using the time domain fitting method AMARES. Screenshots of the interface are shown in Figure 2.7. The program reads both anatomical MRI images (mostly T_2 weighted images are used) and CSI data. At this moment the program supports exported GIF (Graphics Interchange Format) images and PHILIPS CSI data format. The array of spectra is displayed on top of the anatomical image to enable localization of possible tumor regions as can be seen in Figure 2.8. Zooming in on spectra and image enables a detailed visual analysis possible. Different preprocessing steps were implemented:

- *Automatic voxel selection*: In prostate CSI often the area in which spectra

are acquired is much larger than the PRESS box which is chosen in such a way to just surround the prostate. Because it is of no use to process the voxels outside the PRESS box and prostate, only spectra from within the PRESS box are selected and processed.

- *HLSVD water filter*: To remove residual water a HLSVD filter was implemented of which the principles were explained in section 1.3.3. Upper and lower bounds of the HLSVD filter can be defined by clicking on the spectrum. The filter can be used to remove residual water and/or lipids.

- *Grid shift*: the positioning of the different spectra from the CSI is encoded during acquisition using different phases added to the spectra of different voxel positions. The space in which the data are recorded is called *k-space*, because the phases are indicated with the variable k traditionally. Let $D_k(\mathbf{k}, t)$ denote the FID in k-space at position $\mathbf{k} = (k_x, k_y)$ and suppose the dimensions of k-space to be $m_1 \times m_2$. To convert the phase encoded data in k-space to the spatially resolved spectra, a Fourier Transformation is applied:

$$D_x(\mathbf{x}, t) = \sum_{1}^{m_1} \sum_{1}^{m_2} D_k(\mathbf{k}, t) e^{(-2\pi i(k_1 x_1 + k_2 x_2))}. \tag{2.3}$$

To simplify the formula, k- and x-space were supposed to be centered around the origin. If however extra phase is added to the data after acquisition in k-space this will correspond to an artificial grid shift in x-space:

$$D_x(\mathbf{x}, t) = \sum_{1}^{m_1} \sum_{1}^{m_2} D_k(\mathbf{k}, t) e^{(-2\pi i(k_1 x_1 + k_2 x_2))} \underbrace{e^{(2\pi i(k_1 x_1^{shift} + k_2 x_2^{shift}))}}_{added\ phase}, \tag{2.4}$$

where $\mathbf{x}^{shift}$ indicates the shift wanted in x-space. This can be useful to optimize the number of voxels covering the prostate, or to position a voxel from the CSI on a focal lesion. The mathematics behind this procedure are described in [71].

Quantification is done automatically by the AMARES algorithm. Results of the quantification can be visualised (see Figure 2.9) by clicking on the CSI. Default starting values for frequencies and dampings and prior knowledge are stored in a template file, so that the program can be run without any user interaction. If however other starting values might be necessary (e.g. in the case of a new acquisition sequence), other starting values can be programmed easily by a spectroscopist. After quantification the values for the amplitudes of the choline, creatine and citrate are visualized as color maps which are

then overlaid on the MR images (see Figure 2.10), which makes an easy and quick analysis of metabolite concentrations possible throughout the prostate. Because the ratio of citrate/choline is a marker for prostate cancer, a color map of that ratio is also generated. This results in an easily interpretable presentation of metabolic information.

The graphical user interface (GUI) was first implemented in the MATLAB environment. The program was however converted to a Java environment, because it was more easy to implement user interaction with the displayed images. This also makes the program platform independent. The program can be run on any platform given that the free Java Virtual Machine is installed. Another advantage is that a lot of libraries for the Java programming language exist. The program was designed to be easily expanded with other types of quantification or preprocessing algorithms.

The GUI consists of two layers. The first layer is a graphical layer that is responsible for presenting the data on the screen. The second layer is the system layer, which is completely independent of the first layer. The system layer contains all the functionalities and uses native methods for the processing algorithms. The choice to use native code is due to the fact that the Fortran and C languages have fast and specialized mathematical libraries.

2.7 Conclusion

Previous studies [74, 104, 103, 47, 33, 70, 25] reported comparisons of various time and frequency domain based spectral processing methods, but there has not been a comprehensive study of the effectiveness of processing methodologies for prostate ^{1}H spectra. This study compared two data processing approaches, time domain based TDF and frequency domain based FDA, for the performance of their spectral parameter estimates on prostate ^{1}H spectra from simulations, and empirical phantom and patient data. Both TDF and FDA methods had the ability to predict cancerous voxels for an artifact free case study using the ratio of choline+creatine+polyamines to citrate. This is suggested as an effective and robust metric for prostate spectral assessment at 1.5T. Spectral overlap in prostate data acquired at 1.5T was a factor reducing the accuracy of quantification for both of the processing techniques. The TDF method had some problems at modeling the spectra with low SNR. Preliminary results from 3T scanners exhibit higher SNR, and improved spectral resolution with visually separable polyamines. This will likely increase the accuracy of quantification for both methods in the future. The most appropriate choice of the data processing method for any specific application depends on the purpose of the quantification and the type of the spectra analyzed. The results of this study support the use of the TDF method for accurate quantification of the spectra

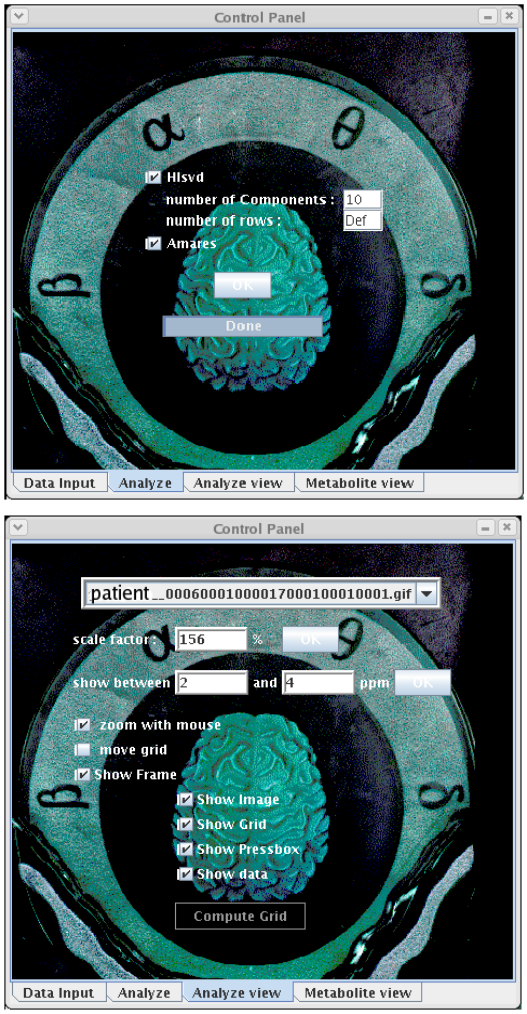

Figure 2.7: Two views of the control panel of the GUI are shown. The first screenshot shows the options for activating the HLSVD filter method and the AMARES quantification. The second screenshot shows the options for visualizing the spectra, MR images and PRESSbox region. The 'Compute Grid' button activates a recalculation of the CSI after it was positioned on its new position relative to the MR image.

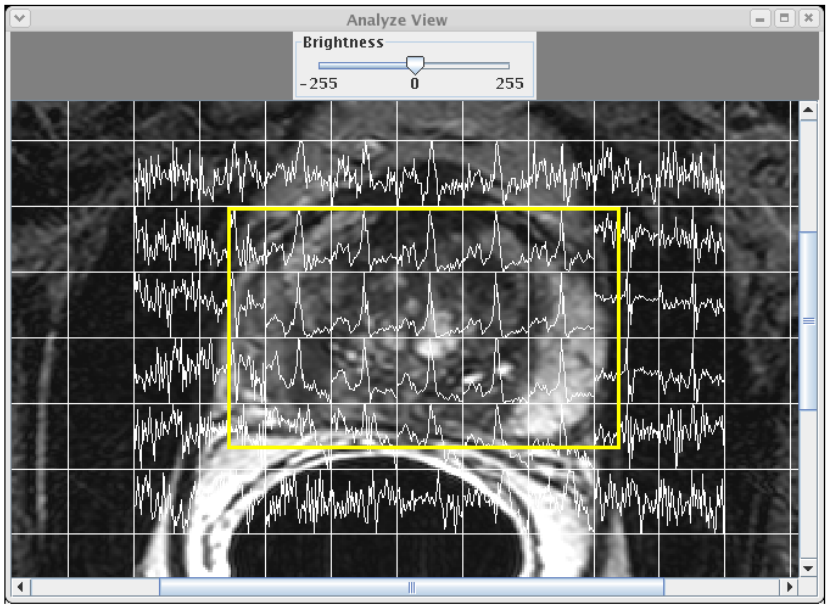

Figure 2.8: An example of the spectral grid superposed on the MR image. Only spectra which will be processed are shown, originating from voxels within the PRESS box region (and one extra row/column). The PRESS box is shown in a thicker line. The image shows clearly the airfilled balloon of the endorectal coil in the lower part of the image and the prostate in the upper part. The spectra are shown in the 2 to 3.5 ppm region, showing choline, creatine and the citrate doublet. Remarkt the slider which controls the brightness of the MR figure.

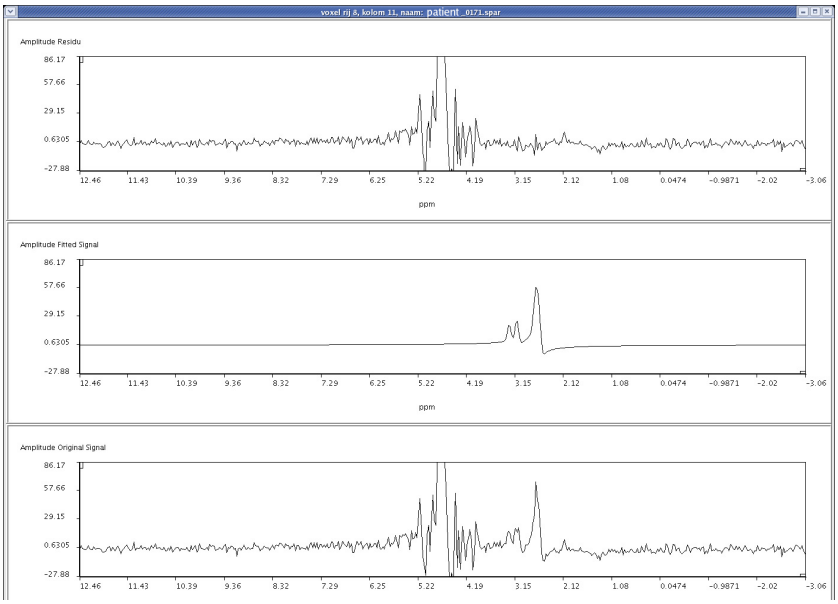

Figure 2.9: Display of the quantification result of the spectrum of a certain voxel. From bottom to top, the original signal, the fit by AMARES and the residue are shown. This quantification result is shown when the user clicks within a certain voxel of the CSI display as is shown in Figure 2.8.

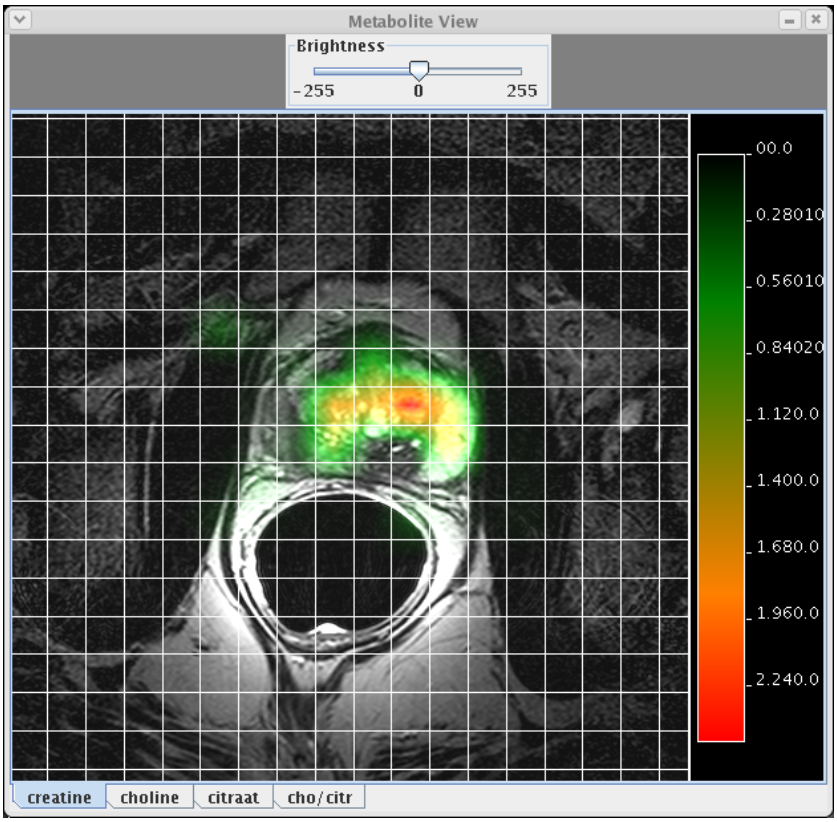

Figure 2.10: Example of a metabolite map of creatine. The estimated amplitudes for creatine throughout the prostate are converted to a color map which scales according to the amplitude. A spot with high creatine can be seen in the left part of the prostate (right on the image).

with good SNR, and its ability to separate sharp resonances from the broader peaks. The FDA method is valuable for robust and fast quantification of the spectra, even when there are acquisition-related distortions in the spectra. Both of these processing methodologies are suitable for routine analysis of prostate spectra for clinical and research purposes.

A graphical user interface was presented for the display and quantification of prostate MRSI data. Features such as a grid shift, solvent filtering and display of metabolite maps after quantification were implemented.

Chapter 3

Multivoxel Time Domain Fitting

This chapter introduces a new combination of FIR filter with multivoxel processing. The concept of multivoxel processing was applied for the first time to MRSI data. The performance of the newly introduced method was analyzed using Monte Carlo simulations, and the possible types of prior knowledge for multivoxel processing are discussed. Because MRSI quantification requires automated processing, the influence of the chosen model order is important. The influence of model order on the parameter estimation accuracy will also be adressed by Monte Carlo simulations. To conclude the chapter, the proposed method is applied to in vivo prostate data.

3.1 Introduction

Processing MRSI datasets requires more complex algorithms than those needed for single voxel spectroscopy, because many more spectra have to be quantified and the processing of all spectra should preferably be done automatically. For MRSI to become a clinical useful tool, it has to be accurate, robust and automated. The quantification has to be accurate in order to improve the reliability of the diagnostic information. Furthermore the quantification should be automated and robust, because the large amount of data does not allow to optimize the quantification process for each spectrum separately.

This idea of processing several spectra simultaneously revealed the possibility of improving robustness and accuracy by implying more prior knowledge [117]. The idea was translated to the processing of MRSI datasets and it was verified

if the available prior knowledge of an MRSI experiment could yield the same benefits. To even further improve the quantification, multivoxel processing was combined with an FIR filter. The combination of multivoxel processing with an FIR filter wasn't presented yet.

When automating batch processing of MRSI datasets, another problem arises: estimation of the model order. The model order determines the number of resonances used to model the spectrum. This choice is not always straightforward, certainly for MRSI measurements, because some resonances are present in one voxel and absent in another, and this information is not known à priori. For example, if a brain MRSI is acquired, lactate will be present in voxels containing tumor tissue and absent in voxels containing healthy tissue. The exact model order changes within the voxels. However, because the quantification should be as automated as possible, the model order cannot be determined separately for each voxel. The chosen model order should be as complete as possible. The question which will be answered in this chapter is: does the accuracy of the estimates of the metabolites present depend on the chosen model order?

Monte Carlo simulations show the influence of multivoxel processing and the influence of the model order on the accuracy of estimates of amplitude and frequency.

3.2 Extension of AMARES$_f$ to multivoxel processing

In Chapter 1 the method AMARES$_f$ was introduced. As was described earlier, processing several spectra simultaneously boils down to minimizing a cost function which includes all spectra. The FIR filtering can also be included in the extended cost function. Suppose there are S signals, each of which can be modeled by Eq. (1.6). The nth sample of the $N-1$ samples of signal s, y_{ns} is then given by

$$\overline{y}_{ns} = \sum_{k=1}^{K_s} a_{ks} e^{j\phi_{ks}} e^{(-d_{ks}+j2\pi f_{ks})t_n} \tag{3.1}$$

The additional parameter index s indicates that the parameter refers to the sth signal of the set and K_s denotes the number of peaks present in the sth signal.

Suppose that signal $\bar{y}_s$ is to be filtered with an FIR filter of length M_s. Following the scheme discussed in the previous Section 1.3.3 (Eq. (1.17)), a similar model function with M_s filter coefficients for signal s can be deduced:

$$\begin{aligned} \overline{y}_{ns}^{fil} &= \sum_{k=1}^{K_s} \bar{h}_s b_{ks} x_{ks}(n) \qquad (3.2) \\ n &= 0, 1, \ldots, N - M_s, M_s \text{ is the filter length of signal } s \end{aligned}$$

where

$$\bar{h_s} = (h_s(M_s - 1) \ldots h_s(0))$$

and

$$b_{ks} = (1 \quad e^{(-d_{ks}+j2\pi f_{ks})t(1)} \quad \ldots \quad e^{(-d_{ks}+j2\pi f_{ks})t(M_s-1)})^T$$

To obtain the estimates for the variables of all the signals we have to minimize the corresponding cost function, which is obtained by summing the cost functions of all signals s over the S signals:

$$\sum_{s=1}^{S} \sum_{n=1}^{N-M_s} \left| y_{ns}^{fil} - \sum_{k=1}^{K_s} \bar{h}_s b_{ks} x_{ks}(n) \right|^2 \qquad (3.3)$$

Remark that this is an extension of the cost function Eq. (1.19) described in the previous section. An index s is added to the filter length M because the length of the filter may vary from signal to signal. For each spectrum s a new filter will be designed. In practice the model order K_s for signal s will be constant over all spectra. Here the algorithm AMARES$_f$ is extended with multivoxel processing and applied to MRSI data and is called AMARES$_{fts}$. This extended method now combines both properties of FIR filtering and multivoxel processing and is used for all following experiments.

The prior knowledge imposed is always a set of linear relations between parameters and as a consequence we obtain a minimisation problem with linear equality constraints which we substitute in the original functional in order to get an unconstrained non linear least squares minimisation problem.

3.3 Cramér-Rao Bounds

The quantification process cannot be made arbitrarily accurate, since for any unbiased estimator a fundamental lower bound on the accuracy of the parameter estimates exists. This lower bound is called the Cramér-Rao bound [99]. To be able to give an expression for this Cramér-Rao lower bound Eq. (3.3) needs to be rewritten as follows:

$$\sum_{n=1}^{N_S} |r_n(\boldsymbol{\alpha})|^2 = \|\mathbf{y}_{Series} - \boldsymbol{\Gamma}_{Series}\mathbf{C}_{Series}\|^2 \tag{3.4}$$

where $\boldsymbol{\alpha}$ denotes the vector containing the m parameters to estimate, $N_S = \sum_{s=1}^{S}(N - M_s)$, and

$$\begin{aligned}
\mathbf{C}_{Series} &= [\mathbf{C}_1^T, \ldots, \mathbf{C}_S^T]^T \\
&= [a_{11}e^{j\phi_{11}}, \ldots, a_{K_1}e^{j\phi_{K_1 1}}, \ldots \\
&\quad , a_{1S}e^{j\phi_{1S}}, \ldots, a_{K_S S}e^{j\phi_{K_S S}}]^T \\
\boldsymbol{\Gamma}_{series} &= \begin{bmatrix} \boldsymbol{\Gamma}_1 & 0 & \ldots & \ldots & 0 \\ 0 & \ddots & & & 0 \\ \vdots & & \boldsymbol{\Gamma}_s & & \vdots \\ \vdots & & & \ddots & \vdots \\ 0 & \ldots & \ldots & & \boldsymbol{\Gamma}_S \end{bmatrix}
\end{aligned} \tag{3.5}$$

with

$$\boldsymbol{\Gamma}_s = \begin{bmatrix} e^{(-d_{1s}+j2\pi f_{1s})t_0} & \ldots & e^{(-d_{K_s s}+j2\pi f_{K_s s})t_0} \\ \vdots & \ddots & \vdots \\ e^{(-d_{1s}+j2\pi f_{1s})t_{N-1}} & \ldots & e^{(-d_{K_s s}+j2\pi f_{K_s s})t_{N-M_s}} \end{bmatrix} \tag{3.6}$$

For noise with a standard deviation σ, the Cramér-Rao lower bound on the jth parameter of the parameter vector $\boldsymbol{\alpha}$ is given by

$$\sqrt{(\sigma^2\mathbf{J}^T\mathbf{J})^{-1}_{jj}} \tag{3.7}$$

where J is the Jacobian matrix, the rows of which are the first derivative vectors of the components of the signal to the model parameters $\boldsymbol{\alpha}$ and σ is the noise standard deviation. It was not necessary to take the influence of the FIR based filter on the CR bounds into account. It was proven that an FIR filter, because it can be interpreted as a prewhitening operation, does not affect the CR bounds [44].

3.3.1 Prior knowledge for multivoxel processing

Because the variables of different spectra are present in the same minimization problem, it is possible to express relations between the parameters of these

spectra. They are imposed in the same way as relations between variables within a spectrum. This is the first time that prior knowledge between spectra of an MRSI experiment is imposed.

However, prior knowledge cannot be applied straightforwardly. To ensure that the applied prior knowledge is based on realistic features of the signal, often preprocessing steps are needed. In this chapter two types of prior knowledge will be used on simulation signals as well as on *in vivo* data. The two types of prior knowledge imposed between different voxels suppose that respectively the frequencies and/or phases of the resonances are constant over the whole CSI set. The preprocessing needed to guarantee a justified use of the two types of prior knowledge will be discussed now.

Prior knowledge on parameters of different voxels originates from the physical properties of the MRSI experiment. For example, the magnetic field can be considered as constant over the MRSI slice due to the shimming. However, the accuracy achieved by the shimming process doesn't allow us to suppose that the frequencies of all the resonances are constant throughout the CSI. To correct for this, the spectra of all voxels need to be aligned in a preprocessing step.

Eddy Current Correction, as was described in [49], corrects for eddy currents by dividing the spectra by the phase component of a reference water signal hereby removing the phase and frequency shifts induced by the eddy currents in the acquired spectrum. This makes it possible to impose the prior knowledge that phases and frequencies are constant over all voxels.

If no Eddy Current Correction is possible (e.g. when no reference signal was acquired) or when the frequency alignment has to be improved a frequency alignment algorithm can be used. Frequency alignment algorithms were proposed in [112, 122]. In [112] the algorithm cCross based on crosscorrelation proved to be a robust frequency aligment algorithm, which will be used in section 3.6 to align the *in vivo* CSI set. Using crosscorrelation, the algorithm calculates the frequency shift of a given peak between two different spectra. The original spectrum is then shifted in the time domain. By applying the frequency alignment preprocessing, the prior knowledge that the frequencies are constant over all voxels can be imposed.

A third example of prior knowledge supposes that dampings are constant throughout the CSI set. This prior knowledge can only be applied when the sample or tissue is very homogeneous as is the case for a phantom. This kind of prior knowledge will not be used here.

In the generated simulation signals (Sections 3.4 and 3.5) the frequencies, and in one case the phases, are set to be constant so that the prior knowledge imposed on those signals is exact.

3.4 Monte Carlo Simulations

Three different Monte Carlo simulations were performed. This section discusses how the different simulated CSI signals are generated.

3.4.1 Monte Carlo simulations of a brain CSI from a healthy volunteer

A Monte Carlo simulation was performed based on a brain MRSI experiment from a healthy volunteer. The MRSI was acquired on a 1.5 T Siemens Sonata Vision scanner operating at 63.61 MHz using a PRESS CSI. The sequence had an echo-time of 135 ms. The axial CSI slice had a matrix of 16 $\times$ 16 in both left-right and posterior-anterior directions, a field of view of 200 mm $\times$ 200 mm and a thickness 13 mm, yielding a voxel size of 12.5 $\times$ 12.5 $\times$ 13 mm^3 or 2.032 cc. 40 voxels were selected within the PRESS box region. Each signal consisted of 512 complex data points, recorded at a sampling rate of 1 kHz. Using the jMRUI program [1] each spectrum was water-filtered and afterwards quantified with a model function containing creatine, choline and NAA. The estimates for amplitudes, phases, frequencies and dampings were then used to generate a noiseless simulation signal for each voxel. Due to the characteristics of the *in vivo* CSI the phase varies from voxel to voxel. To simulate the remaining water residue in each spectrum, the experimental signals were quantified using 15 exponentially damped sinusoids. The exponentials lying between -20 Hz to 40 Hz were used to reconstruct the water region. For each voxel this model for the water region was added to the simulation signal of that voxel. Frequencies of all metabolites were fixed over the voxels. Noise from a Gaussian distribution with different standard deviation σ was then added to the signals. Four different noise standard deviations $\sigma = 3.5, 10, 15, 20$ were used in the Monte Carlo simulation. The corresponding SNR for e.g, NAA, expressed in (dB) and defined as $20\log(a/\sigma)$, ranges from 15.2 to 0.03 dB. The lowest noise level, 15.2 dB, corresponds to the noise level of the original *in vivo* spectra.

The metabolite region of the noiseless simulation signal is shown in Figure 3.1.

The spectra were quantified by means of the AMARES_{fts} algorithm, using three different data processing methods: processing each voxel separately, multivoxel processing with 5 voxels simultaneously and multivoxel processing with 10 voxels simultaneously. This was done using a 3-peak model and using a 5-peak model. The 5-peak model also models a lactate doublet, which is absent in the simulation signals. All three data processing methods are combined with the 3-peak or 5-peak model resulting in 6 different ways in which the dataset is processed.

The number of voxels which are to be processed simultaneously is a compromise between computation time and improved estimation accuracy. Increasing the number of simultaneously processed voxels yields more accurate results but processing more than 10 voxels simultaneously does not improve estimation accuracy much further [117]. Combined with the fact that CPU time increases approximately cubically [117], groups of no more than 10 voxels were processed simultaneously. To assess the gain in estimation accuracy the CR bounds were calculated for increasing number of simultaneously processed voxels. To verify if grouping less voxels could already improve estimation accuracy, also groups of 5 voxels were processed simultaneously in the Monte Carlo simulations.

In the 5-peak model the following prior knowledge within a voxel was used: dampings for all resonances are equal, amplitudes for the lactate doublet are equal. Phases are all set to 0 relative to the overall phase, except for the lactate doublet, which is 180 degrees out of phase. The 3-peak model uses the same prior knowledge but the resonances of the lactate doublet are left out. For multivoxel processing, prior knowledge between voxels was imposed: frequen-

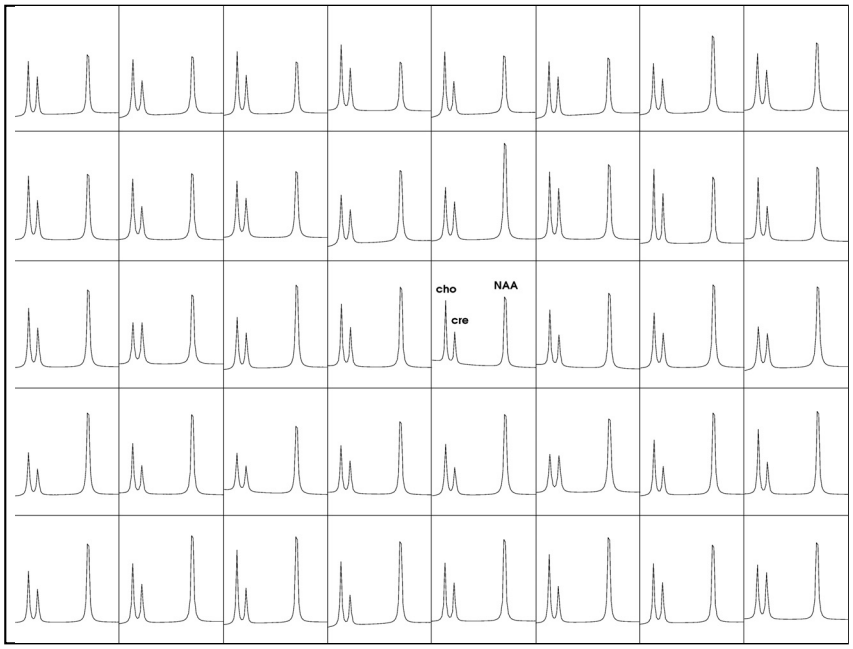

Figure 3.1: HEALTHY BRAIN CSI: The metabolite region of the spectra of the simulated CSI based on a CSI from a healthy volunteer. Creatine, choline and NAA are visible on the spectra. All spectra were plotted with phase zero for presentation, actual phases differ from voxel to voxel.

cies of the different resonances are kept constant in the different voxels. The starting values for frequencies and dampings for AMARES$_{fts}$ are determined by peak picking the first spectrum from the dataset. Those starting values are then used for all the spectra. The results of this Monte Carlo simulation are discussed later in Section 3.5.

3.4.2 Monte Carlo simulations on a CSI from a brain tumour

Simulation signal with variable phase

A Monte Carlo study is performed on 30 simulated signals, derived from a brain CSI region containing tumour tissue. The 16×16 CSI was acquired at 63.61 MHz (1.5T Sonata Siemens),using an echo time of 135 ms. The field of view was 160 mm × 160 mm and the slice thickness 12.5 mm, this yields a voxel resolution of 10 × 10 × 12.5 mm^3 or 1.25 cc. Using PRESS, a brain region with 30 voxels was selected. In this region 10 voxels contained tumor tissue. The same method as previously described was used to generate the simulated signals. After water filtering with the HSVD method, the *in vivo* spectra were quantified using a model containing choline, creatine, NAA, lactate and fat. Fat was modeled using one peak, but with a damping which was independent of the dampings of the other resonances. The simulated fat resonance amplitude is on average smaller than that of the metabolites, as can be seen in Figure 3.2 which shows the metabolite region of the simulated CSI.

To simulate the remaining water the same method was used as described in the previous section. Simulated signals had the same number of points and the same sampling frequency as in the Monte Carlo simulations of a healthy brain CSI. On the simulated signals the following characteristics were imposed: the dampings of all the resonances but fat are equal within a voxel, all resonances have a fixed frequency over all the voxels, the lactate doublet is 180 out of phase and has equal amplitudes. On this simulated CSI dataset, noise from a Gaussian distribution with different noise standard deviations σ was added. Four different noise levels were used: $\sigma = 0.7, 2, 3$ and 4.2. This corresponds with a mean SNR for the NAA resonance of 20.3 to 4.8 dB. For these simulations an extra peak is added to model the fat resonance in the simulation signal.

As in the previous section, the quantification is done using two different models. The first is a 6-peak model which models all peaks present in the simulation signal (choline, creatine, NAA, lactate doublet and fat). A second model does not model the lactate doublet, resulting in a 4-peak model (choline, creatine, NAA and fat). Again the CSI will be processed using different methods: single voxel processing, multivoxel processing with 5 voxels simultaneously and multivoxel processing with 10 voxels simultaneously. Prior knowledge within a spectrum is equal to the one used in the previous example, except that for

fat no relations are imposed with respect to the parameters of the other peaks. Prior knowledge between the spectra is the same as in the previous Monte Carlo study: the frequencies for the resonances are assumed to be equal over all voxels.

Simulation signal with constant phase

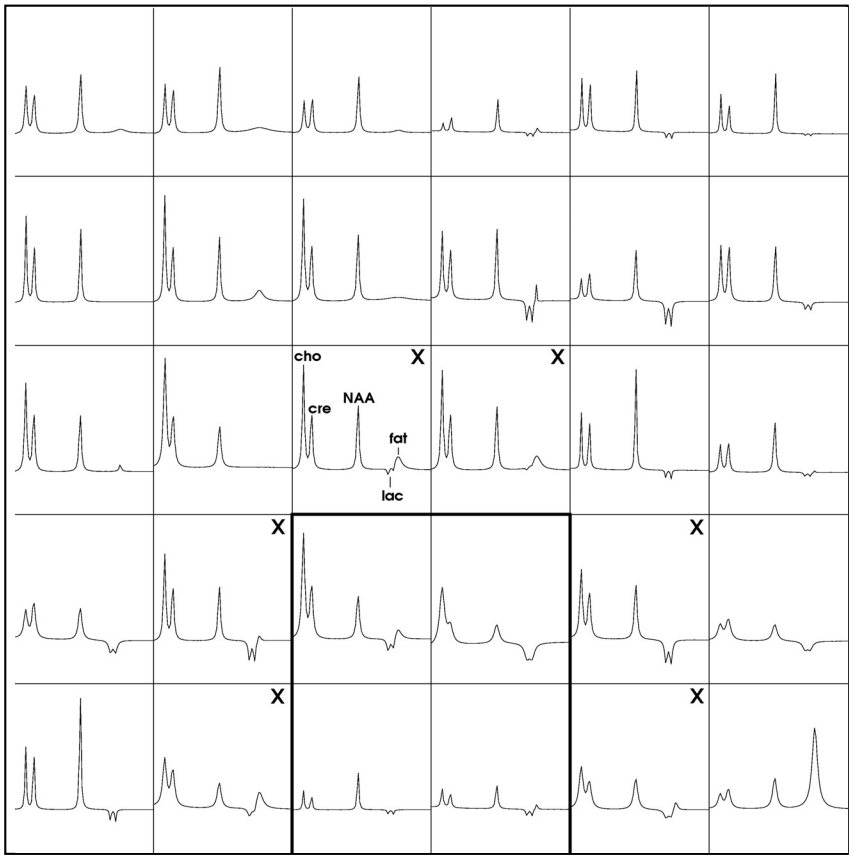

Figure 3.2: TUMOR BRAIN CSI: The metabolite region of the spectra of the simulated CSI based on a CSI containing a brain tumor. Creatine, choline and NAA, lactate and fat are visible on the spectra. Voxels from within the box contain only tumor tissue, voxels marked with an X contain both healthy and tumor tissue. All spectra were plotted with phase zero for presentation, actual phases differ from voxel to voxel. Voxels are arranged from left to right, top to bottom.

To investigate whether the imposition of more prior knowledge could result in a more pronounced difference in accuracy for amplitude estimates between single and multivoxel processing, the simulation signal described in the previous section was slightly modified. The phases of the spectra from all the voxels in the simulation signal were kept constant (-36 degrees). This made it possible to impose this extra prior knowledge to the quantification algorithm AMARES$_{fts}$.

3.5 Results

For each voxel, absolute or relative root mean square errors (ARMSE and RRMSE) of the different peaks and parameters are calculated from the Monte Carlo simulation results. Those results are then averaged over all voxels. Absolute RMSE is used to display errors on the frequency and Relative RMSE is used for errors on the amplitude. Those errors are also compared with the theoretical Cramér-Rao (CR) bounds. The results of all the Monte Carlo simulations described will be grouped in two main items: influence of multivoxel processing and the influence of the model order.

3.5.1 Multivoxel processing

Figure 3.3 shows results of the Monte Carlo simulation for creatine in the normal brain CSI. It can be seen that multivoxel processing improves the accuracy of the frequency estimates. The more spectra are processed simultaneously, the lower the ARMSE. Remark that the theoretical Cramér-Rao lower bound confirms our findings. For the resonances of choline and NAA, the same conclusions hold. However no improvement in the accuracy of the amplitude estimates could be shown for the multivoxel processing. The absence of prior knowledge on the amplitude levels in between different voxels leads to the fact that the amplitude estimation does not increase for multivoxel processing.

In Figure 3.4 the results are shown for the second Monte Carlo simulation, based on a CSI from a brain tumor. The plot is similar to Figure 3.3, but this time results for both model orders are shown (4-peak and 6-peak model). The figure confirms the results described in the previous paragraph: the multivoxel processing approach results in more accurate estimates of the frequency and this for both the 4-peak and 6-peak model. The difference between the two model orders will be discussed in the next subsection.

For the same Monte Carlo simulations no difference in accuracy of amplitude estimates could be detected between single voxel processing and multivoxel processing. This can be seen in Figure 3.5. In this figure also the CR bounds for each method are plotted. They confirm the results from the Monte Carlo simulations: no difference in accuracy of the amplitude estimates can be de-

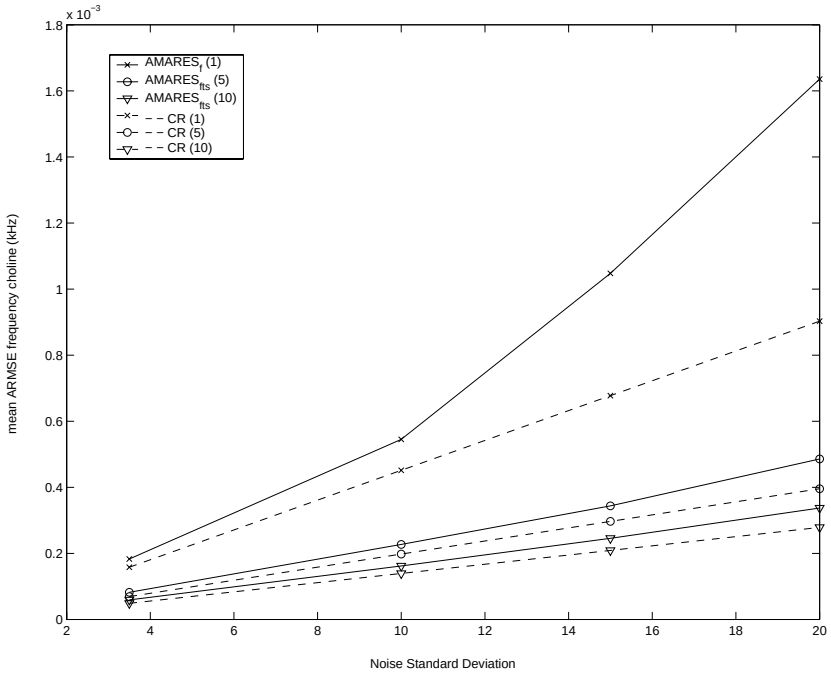

Figure 3.3: NORMAL BRAIN CSI: The averaged ARMSE on the estimated frequency of creatine using a 3-peak model, given for three different methods: single voxel processing (x marks), multivoxel processing using 5 spectra simultaneously (circle marks) and multivoxel processing using 10 spectra simultaneously (triangle marks). The theoretical Cramér Rao bounds for the corresponding methods are shown in dotted lines.

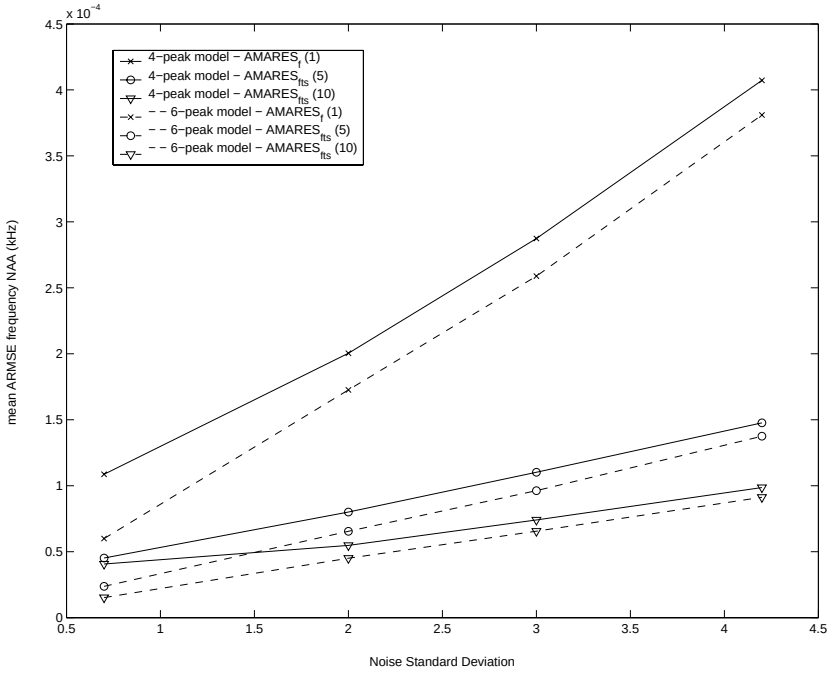

Figure 3.4: TUMOR BRAIN CSI: The ARMSE of the estimated frequency of NAA averaged over all voxels. The ARMSE is given for three different methods : single voxel processing (x marks) , multivoxel processing with 5 voxels (circle marks) and multivoxel processing with 10 voxels (triangle marks) and two models: 4-peak model (solid line) and 6-peak model (dashed line).

tected between the different methods. The reason for this is that no constraints between amplitudes of metabolites in different voxels was used.

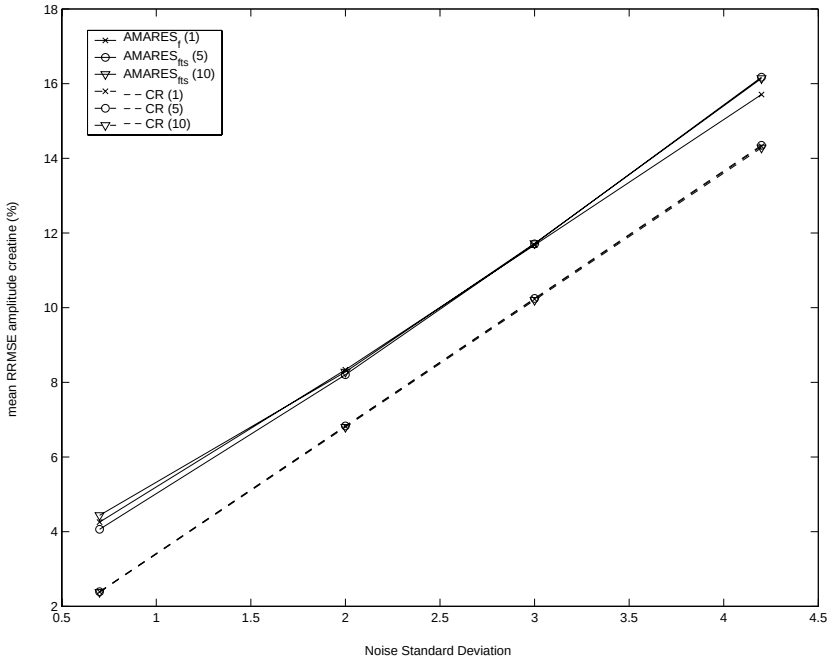

Figure 3.5: TUMOR BRAIN CSI: The mean RRMSE for the amplitude of creatine is shown here for the 4-peak model, and this for the three methods: single voxel processing (x marks), multivoxel processing with 5 voxels (circle marks) and 10 voxels (triangle marks). The theoretical Cramér-Rao lower bounds are shown in dotted lines for all methods. No difference in accuracy can be noticed between the different methods.

The results of the Monte Carlo simulations for creatine in which the phase over the CSI set was set to be constant are shown in Figure 3.6. There is a difference now in accuracy of amplitude estimates. Processing 10 voxels simultaneously is the most accurate method for estimating the amplitude of creatine. The single voxel processing method produced the least accurate amplitude estimates. This difference is present for all peaks as well as in the CR.

3.5.2 Model Order

For the Monte Carlo simulations based on the normal brain CSI, no influence of the model order on the accuracy could be detected neither for frequency nor amplitude estimates. The Monte Carlo simulations based on the brain tumor

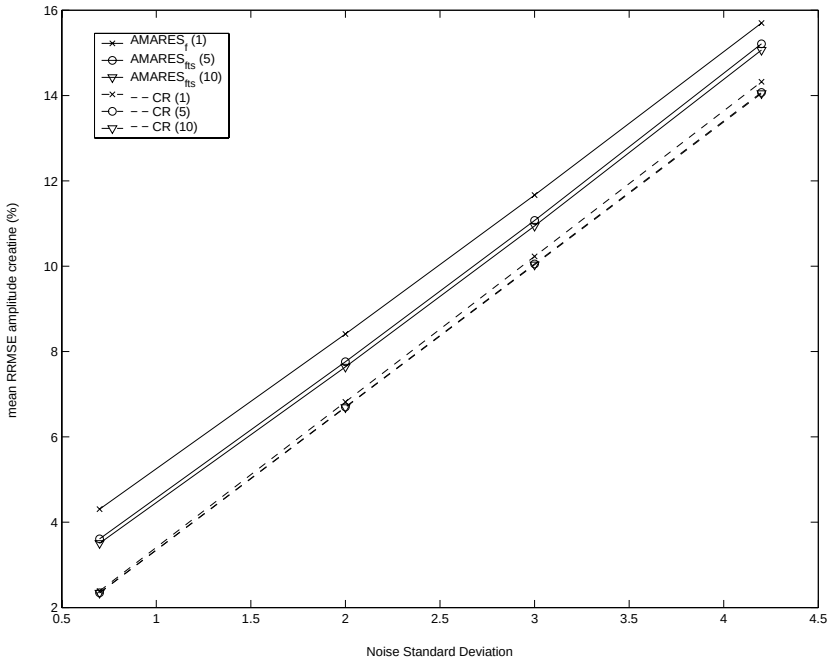

Figure 3.6: TUMOR BRAIN CSI: The mean RRMSE for the amplitude of creatine is shown here for the 4-peak model using the simulation signal with constant phase, and this for the three methods: single voxel processing (x marks), multivoxel processing with 5 voxels (circle marks) and 10 voxels (triangle marks). The theoretical Cramér-Rao lower bounds are shown in dotted lines for all methods. Contrary to figure 3.5, the creatine amplitude accuracy improves by multivoxel processing.

CSI show different results: the ARMSE on the frequency estimates is lower for the 6-peak model for each method, as can be seen in Figure 3.4. The same holds for the other metabolites present in the 4-peak model.

The influence of the model order on the amplitude estimates cannot be seen if the results are averaged over the whole data set. The reason for this is that the spectral content of the spectra changes throughout the CSI which means that another model order of the model function is needed to model the spectra exactly. Voxels containing tumor tissue will contain higher lactate levels than voxels with healthy tissue. Due to this inhomogeneity of the CSI the effect of the model order cannot be deduced from the averaged RRMSE on the amplitudes for the 4-peak and 6-peak model.

To adress the issue of how the model order influences the accuracy of amplitude

estimates, 2 selections of 8 voxels were made in the 30 MRSI simulation signals. The spectra of the first selection (voxels 1, 2, 3, 7, 8, 9, 13 and 14) contain no lactate as can be seen in Figure 3.2. Those spectra can be modeled by a 4-peak model. Selection 2 contains voxels with a high amplitude for the lactate doublet (voxels 10, 11, 19, 20, 22, 23 and 24). The exact model function for selection 2 spectra has a higher model order, i.e. a 6-peak model. The results of the errors on the quantification of creatine for the 2 selections were then averaged over each selection. Figure 3.7 shows that in selection 2, containing spectra with high lactate amplitudes, there is a difference in accuracy between the 4-peak and 6-peak model. Remark that this difference is unobservable in selection 1. The 6-peak model, in this case an 'exact' model, is more accurate than the 4-peak model which in selection 2 undermodels the signal. In contrast to selection 2, selection 1 does not include tumor region, hence the 4-peak model is 'exact' because lactate levels are negligible in this region and the 6-peak model is overmodeling the signal. In this case there is no difference in accuracy. Similar results were found for the other metabolites choline and NAA. No CR bounds are shown on Figure 3.7, because no CR bounds could be derived for the 6-peak model. This is due to the fact that the amplitude of fat is zero in some voxels, leading to singularities in the calculation of the CR lower bound.

3.5.3 Controlled Monte Carlo experiment on the lactate-fat region

Until now, the influence of overmodeling on accuracy was investigated by using a simulation signal derived from an *in vivo* CSI in which the variation of the amplitude of fat and lactate was based on the original CSI. To investigate the influence of overmodeling the lactate/fat region, a more controlled Monte Carlo simulation was performed, in which 9 different ratios of the amplitudes of lactate and fat are used: the amplitudes of choline (18.30), creatine (9.41) and NAA (7.84) are kept constant, but the amplitude of lactate as well as the amplitude of fat are given the values 0, 3 and 6, resulting in 9 combinations of the amplitudes of lactate and fat. Frequencies, dampings and phases were as in voxel 21 of the Monte Carlo simulations on the brain CSI of a tumor. Dampings of choline, creatine, NAA and lactate were equal. The Monte Carlo simulations were performed on 4 different noise levels, but because the same conclusions hold for different noise levels, only the results for $\sigma = 3$ are presented. The signal was processed using the single voxel method and a 6-peak model described earlier for each of the 9 different ratios. The noiseless spectra with the 9 different combinations of amplitudes are shown in Figure 3.8.

The results of the simulations confirm the results described above: overmodeling the signal does not have a significant influence on the ARMSE of the amplitudes of choline, creatine and NAA. Overmodeling occurs for example when the amplitudes of both lactate and fat were put to 0 in the simulation

signal, while the signal was modeled with a 6-peak model. The ARMSE of lactate and fat however show a different behaviour which will be discussed now.

Table 3.1: **ARMSE on the amplitude of lactate**

	lactate		
fat	0	3	6
0	0.398	0.363	0.363
3	0.409	0.473	0.475
6	0.490	0.571	0.515

In Table 3.1 the ARMSE on the amplitude of lactate is shown for the 9 different cases of this Monte Carlo simulation. It can be seen that the amplitude of

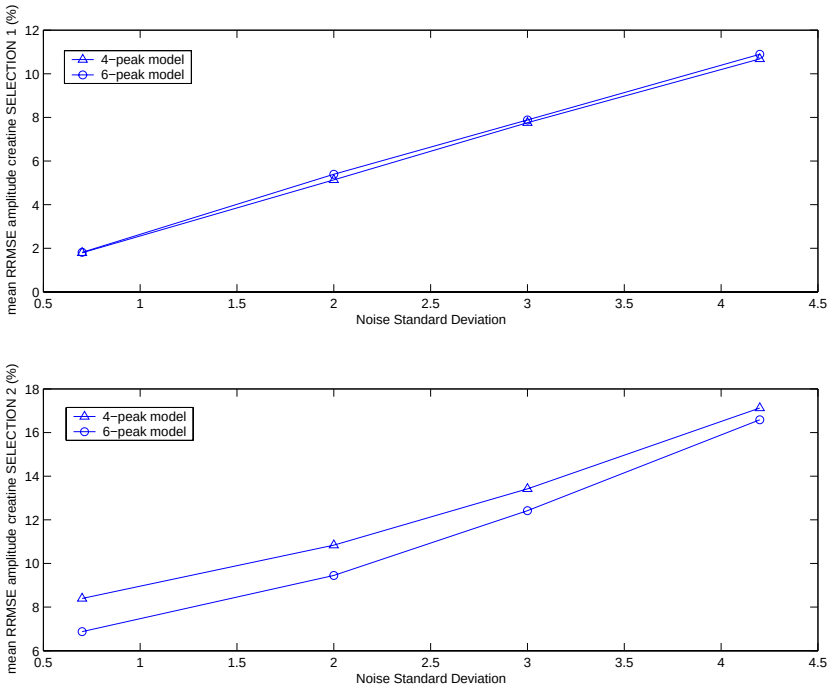

Figure 3.7: TUMOR BRAIN CSI: The figures show the mean RRMSE for the amplitude of creatine using the single voxel method averaged over the ten signals in selection 1 (above) and selection 2 (below). For selection 1 no differences can be observed between the 4-peak and the 6-peak model. In the lower figure, it can be clearly seen that the 6-peak model performs better in estimating the amplitudes of creatine.

lactate is estimated most accurately when the fat resonance is absent (first row in the table). Otherwise stated: the presence of fat hinders the estimation of the lactate amplitude resulting in a lower accuracy for the estimate of the lactate amplitude. Remark that this is the case for all three amplitudes of lactate.

The results shown in Table 3.2 differ from those in Table 3.1. When the results

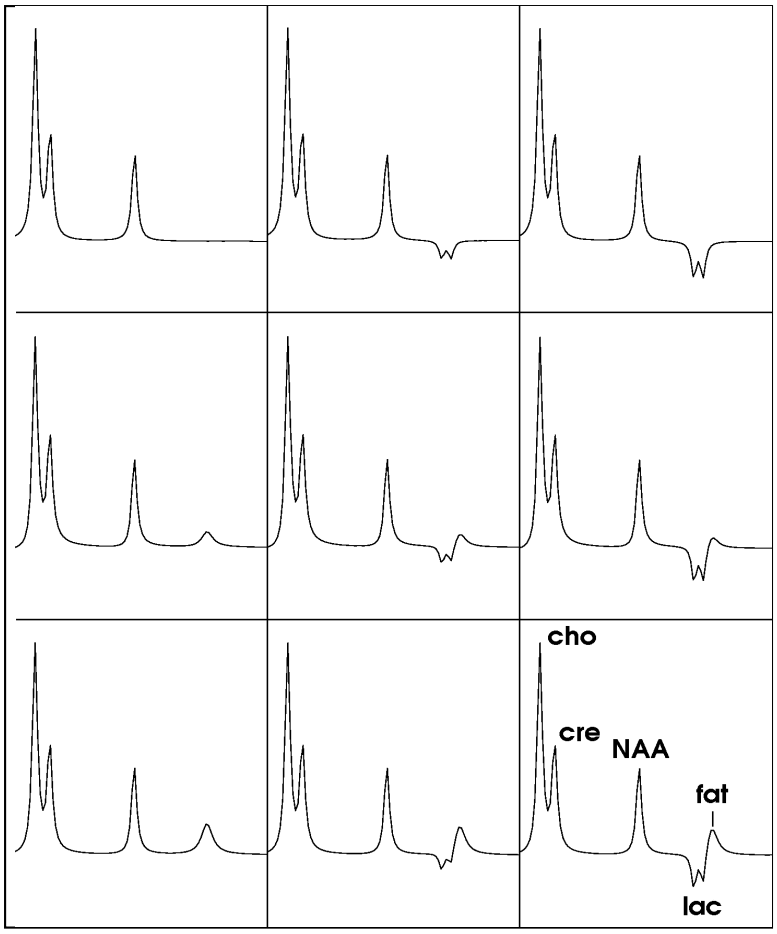

Figure 3.8: The metabolite region of the spectra with the 9 different combinations of amplitudes. Creatine, choline, NAA, lactate and fat are visible on the spectra. The spectra are arranged as in the tables. Due to the larger damping of the fat resonance the fat peak looks smaller than the lactate doublet. All spectra were plotted with phase zero for presentation, the actual phase equals 50.38 degrees.

Table 3.2: **ARMSE on the amplitude of fat**

	lactate		
fat	0	3	6
0	3.05	2.98	1.99
3	2.00	2.28	2.49
6	1.89	1.77	1.81

are read in the vertical direction (for equal values of the lactate amplitude), the ARMSE is smallest for the largest values of the fat resonance, and the errors are larger than for lactate in Table 3.1. Both observations are the result of the same fact: the dampings of fat are not equal to the dampings of the other resonances and therefore no prior knowledge on the dampings of fat could be imposed. This leads to a more difficult estimation of damping and amplitude of the fat peak. The larger the amplitude of the fat peak, the easier the damping will be estimated resulting in a better estimate of the amplitude and thus in a smaller error. This explains why errors are smallest for the third row. The importance of the prior knowledge on the dampings is illustrated in the following paragraph.

The same simulations are repeated with a constant damping for all resonances (including fat) and with corresponding prior knowledge on the dampings. This assumption is purely theoretical and has no meaning in an *in vivo* or *in vitro* experiment but nevertheless the results are interesting. This resulted in an increase of the accuracy of the amplitude estimate of fat by a factor ranging from 2.9 to 5.5 as can be seen in Table 3.3. This indicates that prior knowledge on the damping is important for the accuracy of the amplitude estimates.

Table 3.3: **ARMSE on the amplitude of fat with equal damping for all peaks**

	lactate		
fat	0	3	6
0	0.56	0.54	0.52
3	0.57	0.60	0.57
6	0.58	0.62	0.57

3.6 *In vivo* CSI

Until now the AMARES$_{fts}$ algorithm was used to process simulated brain MRSI signals. Now the algorithm will be applied to *in vivo* prostate MRSI

data. The MRSI data set which will be used was acquired on a 1.5 T Siemens Sonata Vision scanner operating at 63.61 Mhz. Using a PRESS CSI sequence a three-dimensional 16 × 16 × 8 CSI was recorded. The data was acquired with an echo time of 120 ms. The dimensions of the voxels are 5 × 5 × 10 mm^3 or 0.25 cc. No eddy current correction was performed on the data. Thirty voxels from one slice within the PRESS box region were selected. The spectra contain three metabolites: choline, creatine and citrate whose resonance -for the given echo time- can be considered as a doublet. Prior knowledge used for the processing of the spectra was specified as follows:

1. damping of all the peaks are the same within a voxel
2. both peaks of the citrate doublet have equal amplitudes and a fixed frequency splitting of 2.54 Hz, as is known from theoretical calculations.
3. for multivoxel processing: frequencies are constant over all voxels.

Before processing the spectra, they were aligned using the cCross algorithm [112]. On average spectra were shifted -1.23 Hz with a standard deviation of 2.32 Hz.

The 30 spectra were processed with AMARES$_{fts}$ using single voxel processing and with a multivoxel approach, processing 10 voxels simultaneously. The boundaries of the FIR filter of AMARES$_{fts}$ were chosen in such a way that possible residual water and fat resonances were filtered out.

In Figure 3.9 the estimated frequencies for the 4 peaks are shown, for both methods. Due to the prior knowledge imposed, the frequencies remain constant within one block of simultaneously processed voxels (voxels 1 to 10, 11 to 20 and 21 to 30). The values estimated by the multivoxel processing (solid line with + marks) vary slightly over the three blocks, which indicate that the estimated value is close to the actual value. As can be seen in the figure the single voxel method fails to converge to the right frequency in several voxels. This example illustrates another advantage of multivoxel processing: processing several voxels simultaneously increases the robustness of the quantification.

3.7 Discussion and Conclusion

The results show that multivoxel processing allows to increase the accuracy of the estimates of the parameters of an MRSI data set. The application on *in vivo* prostate MRSI data indicates that multivoxel processing also increases the robustness of parameter estimation. Both improvements are due to the possibility to include prior knowledge between different voxels in the multivoxel processing. However, which parameters benefit from the multivoxel approach

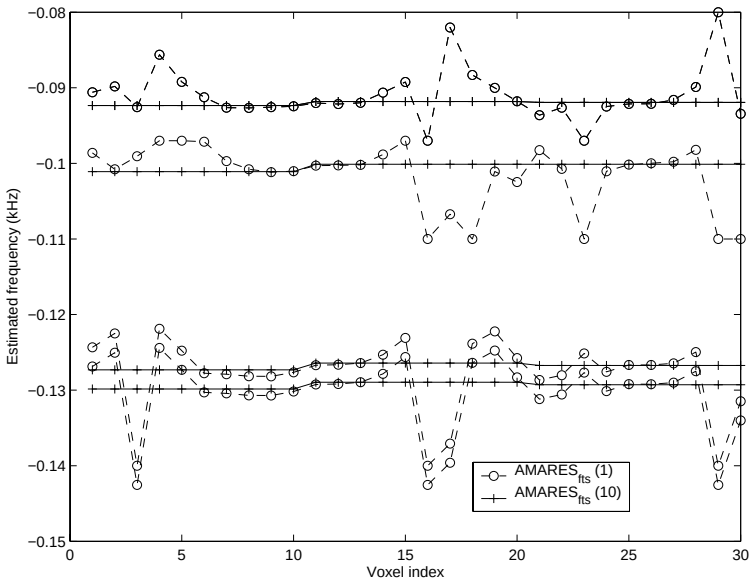

Figure 3.9: The frequency estimates, using single voxel and multivoxel processing, of the frequencies for the 30 voxels are shown here. From bottom to top, the estimates of the citrate doublet, creatine and choline are shown.

depends on the kind of prior knowledge imposed. This was predicted by the calculated theoretical Cramér-Rao lower bounds on parameter estimates and confirmed by the different Monte Carlo simulations. Imposing prior knowledge on the frequencies between voxels results in more accurate estimates of the frequencies. Only when prior knowledge on the phases (Subsection 3.4.2) and/or dampings (Subsection 3.5.3) is added, also amplitudes benefit from multivoxel quantification.

The choice of the model function is often not straightforward in MRSI datasets. Not every voxel contains the same metabolites, and therefore different model orders are needed to correctly model the spectra. Because MRSI processing needs to be automated, one model order is chosen for all spectra. Our simulations show that undermodeling the spectrum has a negative influence on the accuracy of the parameter estimates. On the other hand, overmodeling the spectra with two peaks has no negative influence on the accuracy of amplitude estimates. This indicates that for limited overmodeling with two peaks, a complete model function for all voxels can be chosen when processing MRSI datasets.

Chapter 4

Short Echo Time Quantification: a 2-step approach

This chapter introduces a time domain method for quantifying short echo time spectra, using a database of measured model spectra. The typical difficulties of processing short echo time spectra —baseline and overlapping peaks— are discussed and the proposed method will be outlined. The chapter continues with addressing the influences of the model order on the accuracy of the estimated parameters. This leads to the suggestion of a two-step approach for the modeling of short echo time spectra: in a first step an estimate of the frequency shift of the spectrum is estimated using a limited number of peaks in the model function. This estimate is then used as starting values for a second step in which all metabolites are quantified. To conclude, the method will be applied to a series of in vivo short echo time spectra.

4.1 Introduction

Short echo time spectra (TE $\sim$ 20-30 ms) pose different difficulties to quantification algorithms. Due to the short echo time, metabolites will show more complex spectra and the measured *in vivo* spectra will have many overlapping peaks, which leads to an increased sensitivity to shimming. Additionally, unpredictable underlying broad resonances are present, originating from macromolecules and lipids. Since these resonances can not be described by a Lorentzian or Gaussian lineshape, they are difficult to parametrize.

4.1.1 Metabolite Quantification

Due to their high degree of complexity, short echo time spectra require a more profound analysis than long echo time spectra. The term complexity alludes to the fact that short echo time spectra contain many overlapping peaks and that metabolite spectra often contain multiplets. To tackle this complexity, which is often worsened by low SNR and acquisition artefacts, the use of prior knowledge in quantifying the spectra is mostly exploited. This can be accomplished in several ways. Instead of fitting individual peaks, a set of model spectra is often used to model the spectrum, hence all prior knowledge present within a spectrum of a certain metabolite can be used. By doing so, the complexity of the spectra has become an advantage instead of a drawback: while some metabolite spectra might be overlapping in one region, they can have distinct peaks in another region, making it possible to distinguish nearly identical spectra.

Generating a basis set to model the *in vivo* spectra can be done either in the time or frequency domain. As a basis model set, either the acquired *in vitro* signals can be used or model spectra can be generated. The most frequently used method LCModel [79, 80] combines a fitting in the frequency domain with a database of acquired *in vitro* spectra. The success of the method, which was proposed in 1993, is due to the fact that it was implemented in a commercialized GUI and that it needs very little user interaction. The advantage of using measured *in vitro* spectra is that all effects of the acquisition are incorporated in the model spectra. The effect of the acquisition on multiplets due to coupling is in this way automatically taken into account and full prior knowledge is incorporated. Another method using measured *in vitro* model spectra is the method proposed by Bartha [6, 48]: fitting the spectra is done in the time domain, but the *in vitro* acquired model spectra of the different metabolites are not used. Instead, a basis set is constructed by modeling the measured metabolite spectra, using Voigt lineshapes and extensive prior knowledge. This results in a noiseless basis set, without any disturbing water residual.

A conceptually different approach used in NMR-Scope [37] simulates the basis set, using quantum-mechanics to calculate the model spectra. As input for these calcuations the experimental protocol parameters and prior knowledge obtained by quantum mechanics (number of spins, chemical shifts and J couplings) are used. A time-domain implementation, called QUEST (QUantitation based on QUantum ESTimation), makes use of NMR-Scope [37] and was presented by Ratiney et al.[83]. A similar approach, called PRISMA (PRIor knowledge based modeling of Spectroscopic MAgnetic resonance applications) was presented by Weiland [120] using the GAMMA simulation program [94] to generate the basis set spectra in the time domain. In the same line, the approach followed by Young et al. [124, 95] can be situated, however fitting was performed in the frequency domain after Fourier transforming the basis

set, generated in the time domain, to the frequency domain.

All proposed methods, whether using simulated model spectra or measured *in vitro* spectra seek to incorporate as much prior knowledge in the quantification as possible. So far, using the unaltered *in vitro* measured metabolite signals as basis set for quantification in the time domain was only presented by Lemmerling et al. [59]. This method will be outlined in the next Section and extended to a 2-step algorithm.

4.1.2 Baseline

The disturbing underlying broad resonances of macromolecules and lipids also hamper the quantification. The baseline is difficult to parametrize hence adding it to any parametrized metabolite model is not straightforward. Introducing too few parameters in the estimation of the baseline induces a bias in the metabolite estimates, yet introducing too many parameters might introduce over-fitting. The optimal choice of baseline parametrization can be estimated by the solution of a regularization problem.

To overcome the problem of modeling the baseline, a pure baseline signal can be acquired, for example by means of metabolite nulling [50, 90]. This acquisition sequence makes use of the different T_1 relaxation times of metabolites and macromolecules, which are around 1500 ms for metabolites and 250 ms for macromolecules. After inverting the signals of metabolites and macromolecules during the acquisition, they will relax to the equilibrium position with a time constant T_1. During the relaxation metabolites will cross zero at a certain moment. At that moment, a pure macromolecular baseline can be acquired. This baseline can be added as an extra basis function to the model spectra [90, 43].

Different methods try to approximate the baseline by a mathematical function and include the approximation of the baseline in the nonlinear least-squares fit. Splines and wavelets can be used to model the baseline in the frequency domain [80, 96] or the baseline can be modeled in the time domain as was presented in the PRISMA algorithm [120].

Other approaches take care of the baseline in a preprocessing step. One can make use of the fact that the macromolecular and lipid signals decay quickly. By truncating the initial data points of the FID, their contribution to the signal will be largely reduced [97]. This technique was already used in chapter 2 to reduce the influence of the polyamines. Choosing the right number of samples to truncate can however be difficult because one might also reduce the signal intensity of the metabolites. As a preprocessing step the baseline can also be removed by subtracting either a measured baseline [48] or a splines based model of the baseline [125].

As a last approach to cope with the baseline, HSVD based modeling can be used. HSVD can be used to model any unknown lineshape, as was already done for example to remove residual water [114]. By imposing prior knowledge that the dampings cannot exceed a certain limit, it is prevented that metabolites would be modeled by the HSVD. The baseline model can then be subtracted from the measured spectrum or the baseline can be included in the basis set [16].

4.2 Methods

4.2.1 Short Echo Time Quantification Using AQSES

A method based on the same principle as LCModel, using a basis set of acquired *in vitro* metabolite spectra, but estimating the spectrum in the time-domain, was introduced in [59]. In this work the proposed algorithm, called AQSES (Accurate Quantification of Short echo time Spectra) is extended by introducing a *2-step* algorithm. As the time-domain representation of the signals will be used an additional advantage is that an FIR filter can be used to remove residual water, if present. The method is also similar to LCModel on the part of baseline handling: both methods use splines to model the baseline in the quantification phase.

Although designed for quantification of short echo time spectra, the method can be adapted to quantify long echo time spectra. The principles of this application will be explained in Section 4.2.3.

Substituting the measured basis set in the database by quantum-mechanically simulated spectra (e.g. by use of NMR-SCOPE [37]), can be easily performed, extending the applicability of the suggested *2-step* algorithm.

The basic steps of the algorithm will be outlined first.

4.2.2 Acquisition of model spectra database

The database of model spectra is the building block of the method. Therefore, generating the database of model spectra should be done with ample care. Errors made during the acquisition will hamper any further quantification using the erroneous spectra. The first question to be answered is which metabolites one wishes to quantify. Each metabolite which needs to be quantified should be represented in the database. Most common metabolites as NAA, choline, creatine and glutamine/glutamate need certainly be included in the database, but also less common (usually much smaller) metabolites are usually included in the database (e.g. taurine or aspartate), because they can become prevalent in some pathologies. A complete list of metabolites present in the database is

Metabolite	**Concentration (mM)**
Ethanol (Eth)	200
L-Alanine (Ala)	100
Carnitine (Car)	50
Citrate (Cit)	200
Creatine (Cre)	50
Glucose (Glc)	300
Glutamine (Gln)	100
Glutamate (Glu)	100
Glycine (Gly)	200
myo-Inositol (Ins)	200
L-Lactate (Lac)	100
γ-aminobutyric acid (GABA)	200
NAA	50
Aspartate (Asp)	40
Taurine (Tau)	200
Glycerophosphorylcholine (GPC)	25
Phosphorylcholine (PCh)	27
Lipid 1	n.a.
Lipid 2	n.a.
Acetone (Acn)	*derived*
Acetate (Act)	*derived*
Guanidoacetate (Gua)	*derived*
Pyruvate (Pyr)	*derived*
Succinate (Suc)	*derived*
scyllo-Inositol(Scyllo)	*derived*
NAAG	*derived*

Table 4.1: Model spectra present in the metabolite database. Metabolites in the lower part are deduced from Glycine, except for NAAG which is deduced from NAA.

presented in Table 4.1. Remark that the database includes 2 lipid resonances which can model certain lipid resonances present in the spectrum.

Some spectra present in the model spectra database are not measured as a solution of the pure spectrum, but can be deduced from the single peak spectrum of Glycine. The spectra of acetone, acetate, guanidoacetate, pyruvate, NAAG and succinate all consist of a single peak spectrum and are deduced in that way. No baseline spectrum was present in the model database, however two lipid spectra were acquired.

Two model spectra databases were acquired on a PHILIPS Gyroscan 1.5T clinical scanner, using a PRESS localisation sequence. Databases were acquired

at a TE of 23 and 30 ms. For each model spectrum, the spectrum from a voxel of $20 \times 20 \times 20$ mm^3 was averaged over 512 acquisitions.

During the acquisition several quality issues have to be taken care of. First of all, the model spectra should be acquired with the same acquisition sequence as the one which is used to measure the *in vivo* spectra. In this way model spectra and measured *in vivo* spectra will have the same acquistion related spectral features. The parameters which are required to be equal are:

- the B_0 field strength
- the localization sequence (e.g. STEAM of PRESS)
- echo time.

Some parameters are allowed to vary: repetition time, bandwidth of the acquisition or the number of points acquired from the FID.

The model spectra should have much higher S/N and resolution than the expected *in vivo* spectra. To be able to correct for frequency shifts in the acquired spectrum, each metabolite solution contains an extra compound which serves as frequency reference. After phasing the spectra, they are scaled by use of a concentration marker in the solution, so that every spectrum represents the same concentration. Because a varying pH introduces frequency shifts in metabolite spectra (especially for NAA and Glu), a constant pH of 7.2 has to be ensured.

An overview of the model spectra composing the database can be seen in Figure 4.1. The plotted database was acquired with a PRESS sequence with a TE of 23 ms on a PHILIPS NT Gyroscan 1.5 T clinical scanner. Only the frequency range containing metabolite peaks is shown.

4.2.3 Quantification

The quantification is performed in the time domain. The spectrum which has to be quantified, will be modeled as a linear combination of frequency-, damping- and phase-corrected model spectra. Corrections on phases, frequencies, dampings and amplitudes are obtained by solving the non-linear least squares minimization problem using a Levenberg-Marquardt method [73], which minimizes the cost function. To model the baseline contribution a time domain representation of cubic B splines is added to the model. The model function is given by:

$$\bar{y}(t_n) = \sum_{k=1}^{K} \Delta a_k M_k(t_n) e^{(j\Delta\phi_k)} e^{(-\Delta d_k + j2\pi\Delta f_k)t_n} + \sum_{l=1}^{L} b_l B_l(t_n) \qquad (4.1)$$

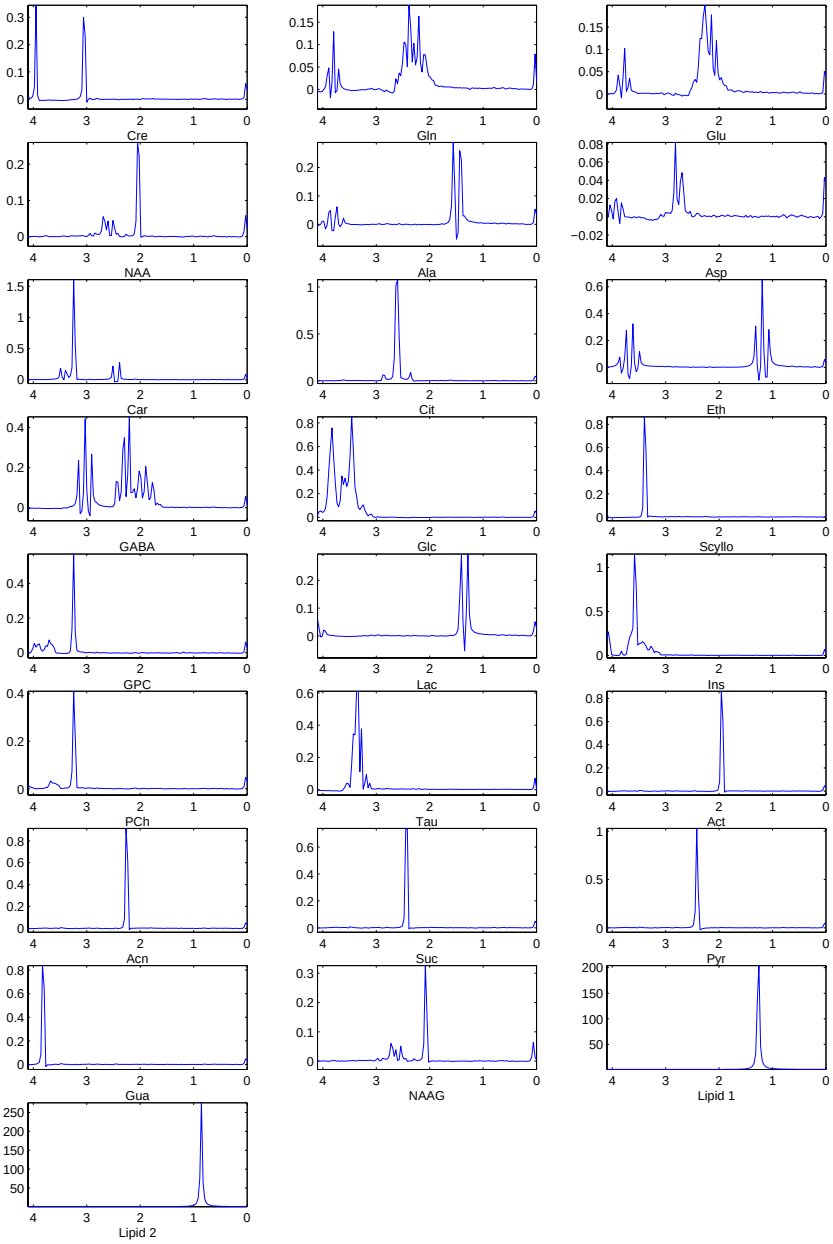

Figure 4.1: Overview of the spectra of the 25 elements in de model spectra database acquired with a PRESS sequence and a TE of 23 ms. The 2 to 4 ppm frequency range is shown.

where M_k denotes the kth measured metabolite model spectrum of the database containing K model spectra. The different correction estimates for model spectrum k are: Δa_k , the amplitude correction; Δd_k, the damping correction; Δf_k, the frequency correction and the phase correction $\Delta\phi_k$. t_n denotes the nth time instant: $t_n = n\Delta t, n = 0, \ldots, N-1$. To model the baseline a linear combination of L cubic B-splines $B_l(t_n)$ is used. The coefficient of spline l is denoted with b_l. The equidistant interval length between inner knots in the frequency domain was set to 3 points, as a trade-off between the complexity of the spline model and the required complexity to model the baseline. Depending on the filter length, a number of points will be truncated from the original signal. Therefore, the number of inner knots will vary. Usually around 150 inner knots are used, which corresponds to approximately 30 splines. For a thorough discussion of B splines the reader is referred to [118, 32].

The cost function which is minimized is the norm of the difference between the measured data and the model function with an added smoothness penalty to make the baseline fit less flexible:

$$\sum_{n=0}^{N-1} |y_n - \bar{y}_n|^2 + \lambda p(b_l), \tag{4.2}$$

where $p(b_l)$ denotes a penalty term defined as $p(b_l) = \|D_p[b_1, \ldots, b_L]^T\|_2^2$ with D_p a discrete approximation of the pth order difference operator (here, $p = 2$ is taken). The penalty function is weighted by a regularization factor λ.

The cost function is minimized using a non-linear least squares optimization based on the Levenberg-Marquardt algorithm. To avoid user interaction, no peak-picking was implemented to provide starting values. Starting values for Δf_k and Δd_k were put to zero and starting values for the amplitudes and phases were obtained by solving the linear least squares problem.

To enable suppression of nuisance resonances, such as residual water, an FIR filter [100] was included in the AQSES method. The use of a maximum-phase FIR filter might also be beneficial for reducing the influence of the baseline for two reasons:

- baseline resonances in the stopband will be suppressed, due to the characteristics of the magnitude response of the filter in that region,
- when using a maximum-phase filter of length M, it is necessary to remove the first $M-1$ data points of the filtered signal because they are distorted by the filter. Even though the maximum-phase filter minimizes the loss of information by introducing a maximum time delay to the filtered signal, information from the first points will be lost. This will lead

to suppressed baseline components because the information of the fastly decaying baseline is mainly present in the initial data points.

The proposed AQSES algorithm also allows the quantification of long echo time spectra by modifying the cost function. Long echo time spectra usually do not contain a baseline, making the splines model redundant in the cost function. To adjust the cost function of AQSES for long echo time quantification, each metabolite model function $M_k(t_n)$ is replaced by a vector $P_k(t_n)$ with the property of being one for all t_n. The spline model is removed, because no baseline needs to be modeled in long echo time spectra. This results in the following cost function:

$$\sum_{n=0}^{N-1} \left| y_n - \sum_{k=1}^{K} \Delta a_k e^{(j\Delta\phi_k)} e^{(-\Delta d_k + j2\pi\Delta f_k)t_n} \right|^2 \tag{4.3}$$

.

This cost function is identical to cost function (1.15) used for long echo time spectra quantification. Therefore, the estimated corrections Δa_k, $\Delta\phi_k$, Δd_k and Δf_k should be interpreted as the amplitudes, phases, dampings and frequencies of the respective Lorentzians.

4.2.4 Applying AQSES to simulated signals

The proposed method AQSES was implemented in MATLAB and tested on simulation spectra. A simulation signal was generated, starting from the analysis of an *in vivo* short echo time spectrum of a healthy volunteer. The *in vivo* spectrum was acquired on a PHILIPS NT Gyroscan 1.5 T clinical scanner, using a PRESS sequence with an echo time of 23 ms. The database used was acquired under the same experimental conditions.

The acquired *in vivo* spectrum was quantified using the AQSES method, resulting in amplitude corrections for the different model spectra. The simulation signal was then generated by taking the linear combination of the model spectra with the computed amplitude corrections. The metabolite region of the simulation signal is shown in Figure 4.2. No baseline was simulated.

To verify the convergence of the method, first small noise levels were applied to the simulated signal. White Gaussian noise with 20 different standard deviations was added to the simulation signal. Standard deviation of the noise was equal to 10^{-k}, with k varying from 1 to 20. This corresponds with signal-to-noise ratios of $1.6 \cdot 10^{-2}$ to $1.6 \cdot 10^{18}$. To verify the convergence of the algorithm, the norm of the residue was measured. The residue is the difference between the simulation signal and the fit by AQSES. The results are plotted in Figure 4.3.

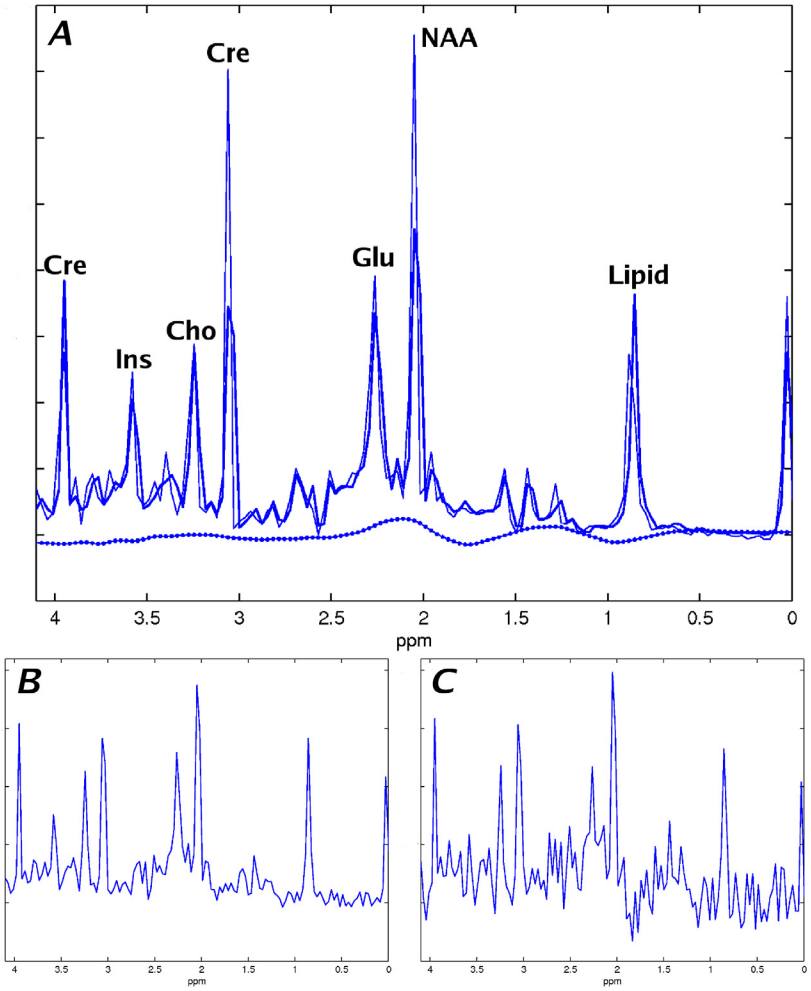

Figure 4.2: (A) Simulation signal deduced from a short echo time spectrum from the brain of a healthy volunteer (thick line) and the simulation with a frequency and damping shift of 1 Hz (thin line). At the bottom the simulated baseline is plotted. (B) Simulation signal used in Monte Carlo simulations of Section 4.3. (noise $\sigma = 2$) (C) Simulation signal used in Monte Carlo simulations of Section 4.3 (noise $\sigma = 8$)

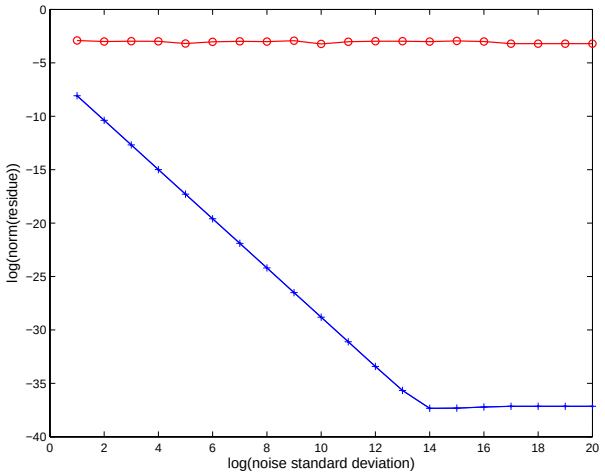

Figure 4.3: Logarithm of the residue plotted versus the logarithm of the standard deviation of the added noise. The line marked with + indicators, shows residue values for the original simulated signal. The line with the circle indicators, shows the residues of a simulated signal with a frequency shift of 1 Hz added to the metabolites.

It is observed that for smaller noise levels, the norm of the residue gets smaller. The residue is due to the noise which is left over in the residue. The norm of the residue becomes approximately constant for noise standard deviation of 10^{-14} or lower. This is due to the fact that the minimization algorithm iterates until the residue is below a certain accuracy threshold.

The same convergence test was repeated after adding a frequency shift of 1 Hz and a line broadening of 1 Hz to the simulation signal. In this case, the residue is much larger, which indicates that the algorithm is sensitive to frequency and damping shifts. This observation will be confirmed by Monte Carlo simulations in the next Section.

4.2.5 Applying AQSES to *in vivo* signals

The quantification of *in vivo* spectra is complicated by the presence of a baseline and by other acquisition related artefacts. The performance of AQSES_{2step} using baseline modeling and without baseline modeling method will be verified by applying the algorithm to 50 *in vivo* short echo time tumour spectra.

In the framework of the European INTERPRET project, 205 short echo time spectra from different brain tumours were acquired by 6 different centres. Only spectra collected by the IDI (Institut de Diagnòstic per la Imatge), Barcelona

(Spain) were used. From the collection, 50 short echo time spectra were selected. They were all acquired at 1.5T with a PRESS sequence and an echo time of 30 ms. Different tumour types were represented: glioblastomas (n=11), medulloblastomas (n=6), meningiomas (n=10), meningiothelial meningiomas (n=4), astrocytomas (n=5), metastasis (n=7), abcsesses (n=3), lymphoma (n=2), Schwanoma (n=1) and pituitary adenoma (n=1). For use in the INTERPRET project, all MRS data were preprocessed following the INTERPRET preprocessing protocol: first a frequency and zero order phase correction was applied using Klose's method [49]. Secondly, the residual water peak was filtered out using HSVD, with 15 singular values over the water region of 4.09-5.31 ppm. The initial point of the time-domain signal was removed, because it was often affected by instrumental artefacts. The baseline was unaffected.

The database acquired with an echo time of 30 ms was used to correspond with the echo time of the acquired spectra. The IDI dataset was selected because all spectra were acquired using a PRESS localisation sequence, which corresponded with the available database.

The spectra were quantified using the AQSES_{2step} algorithm with and without a splines model for the baseline. Also two different types of prior knowledge were supplied to AQSES_{2step}: the first limited set of prior knowledge supposed the following dampings to be equal: $\Delta d_{Gln} = \Delta d_{Glu}, \Delta d_{GABA} = \Delta d_{Cr}, \Delta d_{PCh} = \Delta d_{GPC}, \Delta d_{NAA} = \Delta d_{NAAG}, \Delta d_{Lipid1} = \Delta d_{Lipid2}$; the other set of prior knowledge supposed all dampings to be equal except those of the lipids. The combination of both results in 4 different quantifications of the 50 spectra. The reason to constrain all dampings was the observation that when not all dampings were constrained, some metabolites were estimated to have large dampings (or large linewidths) thereby partly modeling the baseline. The regularization parameter was chosen to be $\lambda = 0.04$.

4.3 Results

Short echo time spectra are often characterized by many overlapping peaks. Peaks are often as small as the noise on the signal, making the choice of the model order in (4.1) not straightforward. When the complete database with model spectra is used, the possibility that the model order is too high becomes realistic. The results of the experiments will lead to the suggestion and analysis of a 2-step algorithm.

4.3.1 Monte Carlo simulations I : 4 landmarks

The influence of the model order in this first simulation will be adressed by performing two different types of Monte Carlo simulations. The first type used the

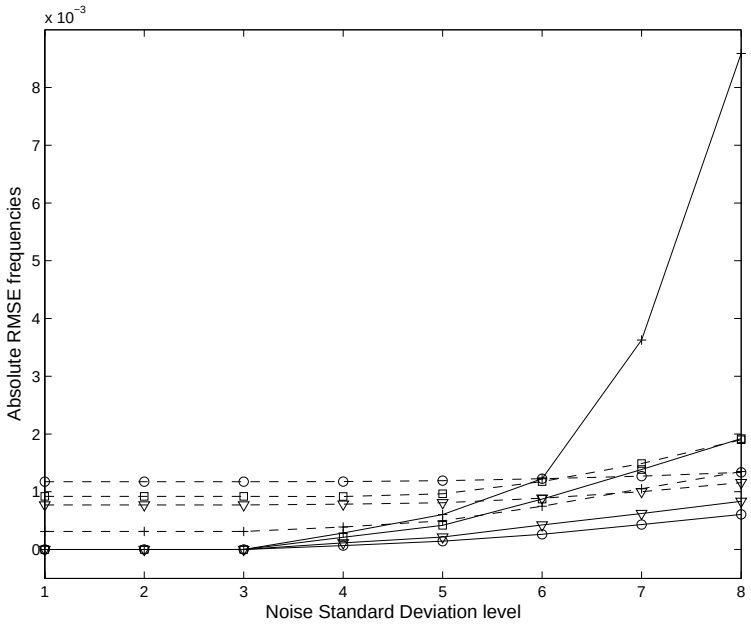

Figure 4.4: The absolute RMSE for the Cre (∘), NAA (▽), Ins (□) and PCh (+) frequency estimates of the two different Monte Carlo simulations: solid lines indicate the results obtained with the complete database, dashed lines indicate a fit using only the 4 landmarks.

complete model spectra database to fit the simulated spectrum. This method will be indicated as AQSES_{25}. A second method used only 4 peaks to model the simulation signal and will be referred to as AQSES_4. The 4 peaks used in the second type of experiments correspond to the most prominent peaks in a healthy brain spectrum [4]: creatine, NAA, myo-Inositol and phosphorylcholine, also referred to as *landmarks*.

Monte Carlo simulations were performed by adding 200 noise realizations with different standard deviations. Spectra were normalized to obtain a maximum real value of the FID to be 100. Noise with 8 different increasing standard deviations were added to the simulation signal: $\sigma = 10^{-15}, 10^{-10}, 10^{-5}, 1, 2, 6, 8$, which corresponds to a signal-to-noise ratio of 340 to 21.9 dB. The absolute RMSE on frequency estimates and the relative RMSE on the amplitudes were calculated.

For high signal-to-noise ratios, the estimates of the frequencies of the metabolites Cre, NAA, Ins and PCh are most accurate using AQSES_{25}. For the first three noise levels, the RMSE of the AQSES_{25} is even zero to within the

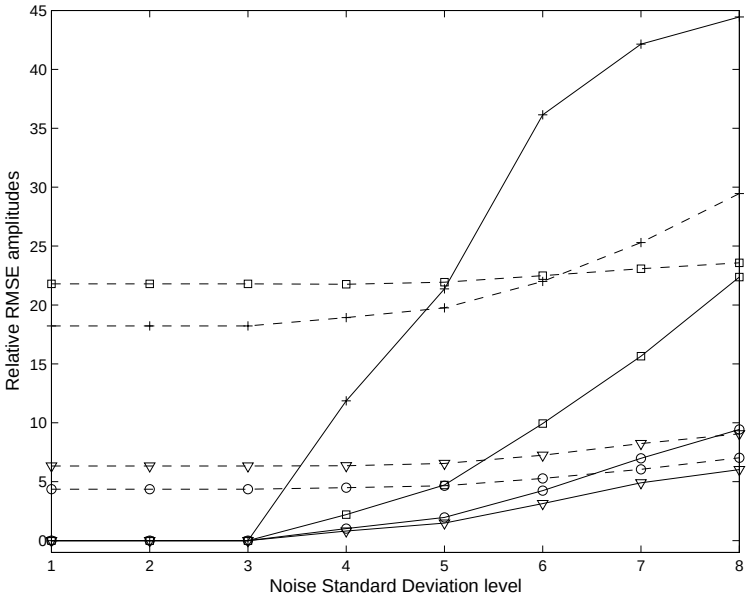

Figure 4.5: The relative RMSE for the Cre (∘), NAA (▽), Ins (□) and PCh (+) amplitude estimates of the two different Monte Carlo simulations: solid lines indicate the results obtained with the complete database, dashed lines indicate a fit using only the 4 landmarks.

accuracy of the used MATLAB environment. However, if the signal-to-noise level decreases, the errors increase. The RMSE on frequencies and amplitudes increases faster for the $AQSES_{25}$ method than for the $AQSES_4$ method. Apparently, the $AQSES_4$ method is less sensitive to the SNR of the spectrum. For the lowest SNR levels, the $AQSES_4$ becomes more accurate in estimating the frequency and amplitudes.

Similar results hold for the relative RMSE on the estimated amplitudes, which are shown in Figure 4.5.

The results suggest that in low SNR spectra, estimating the frequency shift of the spectrum by only using the 4 landmarks while fitting the spectrum can be beneficial. This idea was further confirmed by the following Monte Carlo simulations, in which a frequency shift and linebroadening was added to the simulation signal.

4.3.2 Monte Carlo simulations II: frequency and damping shift

In *in vivo* spectra, frequencies and dampings often differ from the model base spectra. A frequency shift might be introduced by a different pH *in vivo* and a shift of the damping can be caused by a different magnetic field homogeneity. To simulate this, a frequency and damping shift was added to the simulation signal. To do so, the original simulation signal $S(t)$ is multiplied with an appropriate factor:

$$S_{shift}(t_n) = S(t_n)e^{(d_{shift}+j2\pi f_{shift})t_n}. \tag{4.4}$$

The frequency and damping shift was chosen to be 1 Hz. The results of the Monte Carlo Simulations are presented in Figures 4.6 and 4.7. The results show that in this case, with added shifts on frequencies and dampings, AQSES_4 is more accurate than AQSES_{25} for NAA, Cre and Ins. For Cre, AQSES_4 is only more accurate than AQSES_{25} for lower SNR. Remark that noise levels 6 to 8 are most corresponding to *in vivo* noise levels. NAA displays unexpected behaviour: the RRMSE is much larger than the RRMSE of the other metabolites and the RRMSE decreases as the noise level increases. The RMSE on the estimates by the AQSES_4 method are less sensitive to the signal-to-noise ratio.

The unexpected behaviour displayed by the relative RMSE of NAA is due to the fact that the NAA peak modeled the NAAg peak. This can be clearly seen in the amplitude estimates (not shown here). Because the model spectra of both NAA and NAAg are present in the model database and only differ by a small frequency shift (see Section 4.2.2) such an interchange is possible. From the results of the amplitude estimates, it could not be concluded that the NAAg peak modeled the NAA peak in turn, which implies that correcting the error by switching results of both peaks is impossible. This error points to a sensitive part of the method: because of the relatively large database, similar lineshapes will be included, wich can lead to an interchanged modeling of metabolites. This is specifically the case for database entries which are deduced from a single resonance model spectrum as Glu or NAA. This type of error should be avoided as much as possible. Because no NAAg is present in the database when using the AQSES_4 method, NAA is correctly modeled. The error in the amplitude and frequency estimates produced by the exchange of NAA and NAAg becomes smaller as SNR drops, explaining the decrease in RMSE of amplitudes and frequencies for lower SNR.

4.3.3 AQSES_{2step}

Monte Carlo simulations comparing the AQSES_4 and AQSES_{25} showed that especially for lower SNR levels, using only 4 landmarks increases the accuracy of the corresponding frequency estimates compared to when the complete database is used to model the spectra. From this observation, the idea emerged to quantify spectra in two steps.

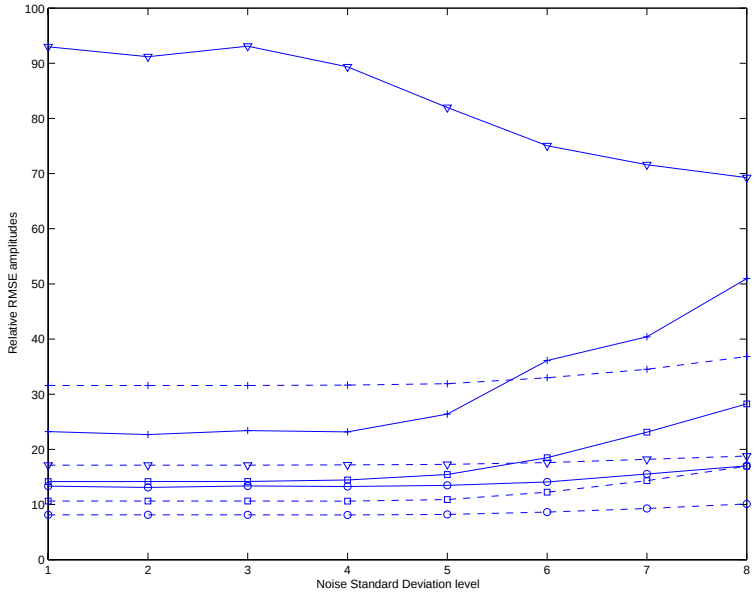

Figure 4.6: The relative RMSE for the Cre (○), NAA (▽), Ins (□) and PCh (+) amplitude estimates of the two different Monte Carlo simulations: solid lines indicate the results obtained with the complete database, dashed lines indicate a fit using only the 4 landmarks. The presented results were obtained on the simulation signal with an added frequency and damping shift of 1 Hz.

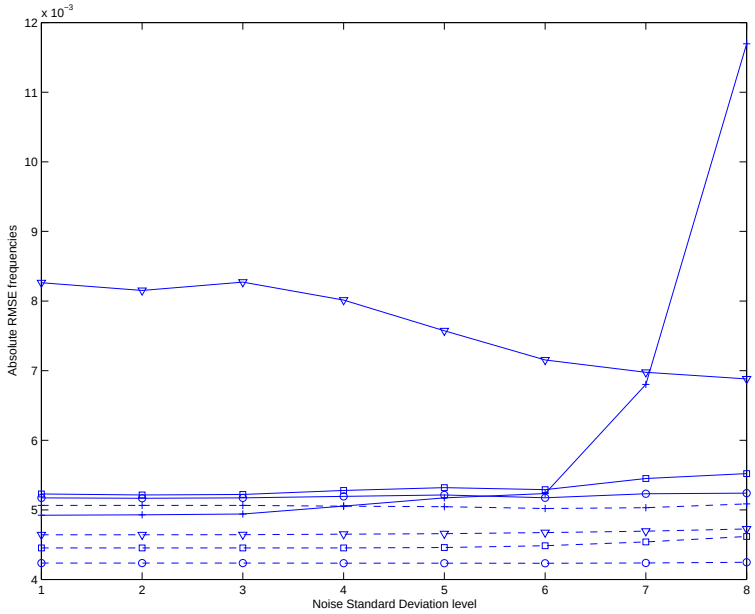

Figure 4.7: The relative RMSE for the Cre (∘), NAA (▽), Ins (□) and PCh (+) amplitude estimates of the two different Monte Carlo simulations: solid lines indicate the results obtained with the complete database, dashed lines indicate a fit using only the 4 landmarks. The presented results were obtained on the simulation signal with added 1 Hz frequency and damping shift.

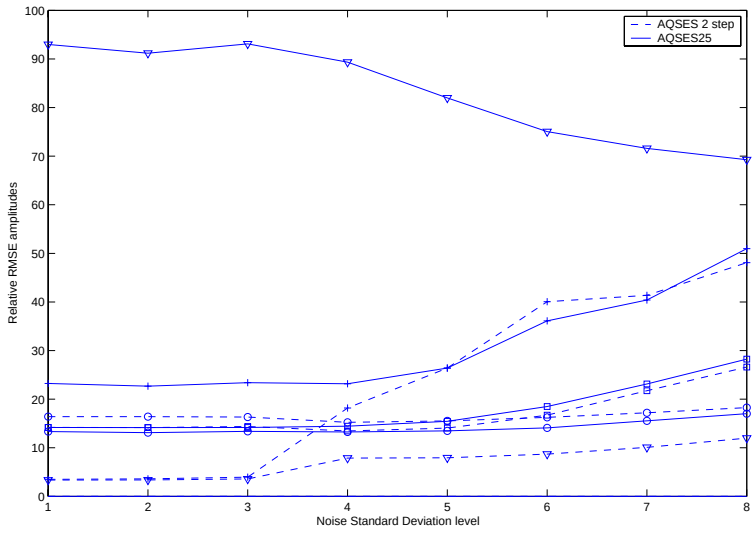

Figure 4.8: The relative RMSE for the Cre ($\circ$), NAA ($\triangledown$), Ins ($\square$) and PCh ($+$) amplitude estimates : solid lines indicate the results obtained with the complete database (AQSES_{25}), dashed lines show results obtained with the 2-step method (AQSES_{2step}). The presented results were obtained on the simulation signal with added 1 Hz frequency and damping shift.

In a first step, the AQSES_4 algorithm is used to quantify the 4 landmarks. The frequency estimates for the 4 landmarks will then be used to provide frequency starting values for AQSES_{25}. Because the 4 landmarks are prominently present in most short echo time spectra, frequency shift estimates for those landmarks tend to be more robust than those based on small metabolites. Frequency shifts are usually not metabolite dependent, but apply to all metabolites. The estimated frequency estimates of the 4 landmarks are therefore averaged to obtain an estimate of the frequency shift. This estimate is then used as frequency starting value for all metabolites in the AQSES_{25} algorithm. This 2-step algorithm will be called AQSES_{2step}.

To verify whether the proposed method is able to provide more accurate and robust estimates the 2-step method was used to perform Monte Carlo simulations using the same simulation signal as before.

First the difference in the accuracy of the quantification with AQSES_{25} and AQSES_{2step} of the 4 landmarks was interpreted. The results obtained for those 4 metabolites, presented in Figure 4.8, display the different possible influences of the 2-step method.

The results don't indicate a uniform increase of estimation accuracy. The

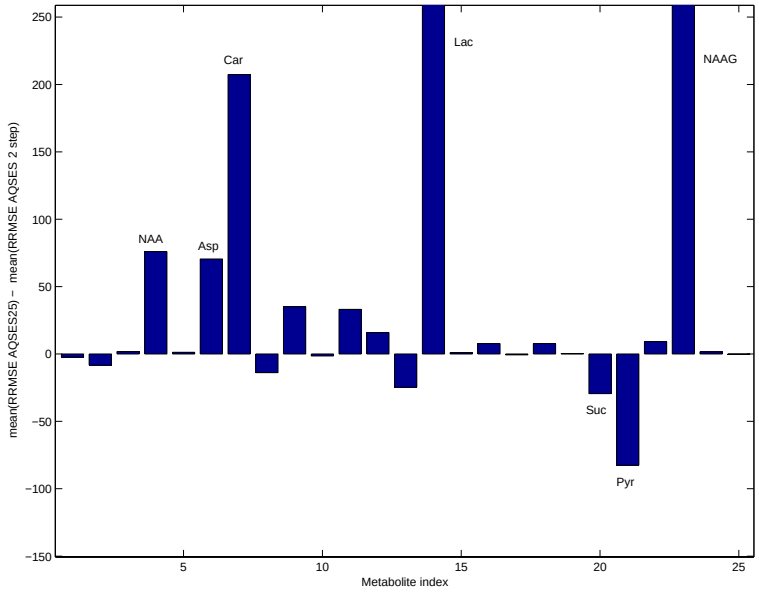

Figure 4.9: The difference in averaged RRMSE for the amplitudes between the $AQSES_{25}$ and $AQSES_{2step}$ method. Large differences were annotated. Positive differences indicate a better performance by the $AQSES_{2step}$ method.

influence of the 2-step method is not the same for the different metabolites in the database. The figure shows that the RRMSE for choline, creatine and myo-inositol doesn't change much by introducing the 2-step method. A slight increase in accuracy can be seen for Ins and PCh, a slight decrease for the RRMSE of Cre. However, the most interesting point is the large increase in accuracy of the estimation of the amplitude of NAA, showing RRMSE which are almost ten times smaller if the 2-step method is used. By using $AQSES_{2step}$, the error of modeling NAA by the NAAg resonance is thus avoided. This indicates that a 2-step approach might be mainly beneficial for the robustness of the quantification by avoiding interchanges in between model spectra. To compare $AQSES_{25}$ with $AQSES_{2step}$ for the other metabolites, the difference of the means of the RRMSE was compared.

To assess the overall changes in estimation accuracy of all metabolites the RRMSE on the amplitudes were averaged over the 8 noise levels and the differences between the $AQSES_{2step}$ and $AQSES_{25}$ averages were calculated. The results are presented in Figure 4.9. A large increase in estimation accuracy for NAA was already displayed in Figure 4.8 and is represented in Figure 4.9 as well. Other metabolites such as Asp, Car, Lac and NAAG also show large increases of estimation accuracy. The increase in accuracy of NAAG (3366 %)

when using AQSES_{2step} shows that the NAAG model spectrum no longer erroneously models the NAA resonance when using AQSES_{25}. Also Lactate shows a major increase (5826 %) in accuracy when using AQSES_{2step}. This increase is also due to the fact that an incorrect fit by AQSES_{25} is avoided. Indeed, when using AQSES_{25}, estimates for frequencies, dampings and amplitudes had a large offset, indicating an incorrect Lactate fit. The increases for Asp and Car are similar. However, AQSES_{2step} also lowers the estimation accuracy for Suc and Pyr: Suc and Pyr had an decreased RRMSE of respectively 21% and 82%.

Generally, by using frequency starting values obtained by AQSES_4, the number of erroneous fits could be reduced, resulting in more robust estimation of amplitudes for AQSES_{2step}. Providing starting values appears to have an important influence on the robustness of the method.

4.3.4 Baseline Modeling: preliminary results

In the previous Monte Carlo simulations a baseline was not included in the analyses. The implemented method of incorporating a baseline model by using cubic B splines, will be tested on its efficiency in dealing with the baseline. For this purpose, a new simulation signal was generated. A short echo time spectrum was obtained from a healthy volunteer, as was described in Section 4.2.4. This spectrum was quantified using the proposed AQSES method, including a baseline fit. To generate the simulation signal, the estimated baseline was added to a simulated metabolites signal, which was generated as in Section 4.2.4. The simulated baseline is plotted in Figure 4.2(A).

The main aim of quantification of short echo time MRS data is to obtain amplitude estimates of the different metabolites, containing information of the concentration of the different metabolites. Handling the baseline during the quantification is aimed to increase the accuracy of the metabolite estimation, which implies that baseline fitting is not a goal as such. Therefore, the Monte Carlo simulations performed on the simulation signal with baseline will focus on the influence of the baseline modeling on the accuracy of parameter estimates.

Monte Carlo simulations were performed on the above described simulation signal, and the same noise levels were used as described in Section 4.2.4. The simulation signal was quantified using the AQSES_{2step} algorithm but with and without baseline modeling with splines. As a first approach, the baseline is not modeled, which corresponds to the regularization factor being set to $\lambda = 0$ in the cost function (4.2). In the second approach, the baseline is modeled with the splines function, with a regularization factor set to 0.04. Remark that λ was not optimized, using e.g. generalized cross validation, but was chosen heuristically.

	(RRMSE (%))		
Metabolite	**No Baseline**	**Splines**	**Difference**
Cre	15.00	18.37	+3.37
Gln	36.57	43.73	+7.16
Glu	28.69	24.26	-4.43
NAA	14.78	16.32	+1.54
Ala	26.03	21.79	-4.24
Asp	46.44	47.80	+1.35
Car	146.33	181.09	+34.76
Cit	69.45	89.84	+20.39
Eth	75.08	63.29	-11.79
GABA	21.43	22.90	+1.46
Glc	112.03	178.31	+66.28
Scyllo	78.43	99.77	+21.34
GPC	55.27	72.37	+17.10
Lac	3791.53	3100.61	-690.92
Ins	14.88	19.12	+4.24
PCh	20.99	30.38	+9.39
Tau	36.47	34.41	-2.06
Act	33.27	36.72	+3.45
Acn	10.26	13.79	+3.53
Suc	60.01	81.03	+21.02
Pyr	71.66	99.58	+27.92
Gua	56.06	60.51	+4.45
NAAG	78.43	158.34	+79.92
Lipid 1	162.96	82.54	-80.42
Lipid 2	7.88	13.60	+5.72

Table 4.2: RRMSE of amplitudes averaged over the 8 different noise levels. Results for fit without baseline fit and with a spline model.

The results were averaged over the 8 different noise levels and are presented in Table 4.2.

The spline model shows for 19 metabolites an increase of averaged RRMSE when a spline baseline model was included in the model function. However, this increase is not uniformly spread over all noise levels. When noise levels are higher, more metabolites have an increased RRMSE. For the 8 different noise levels, the number of metabolites which had an increased RRMSE when splines were included was: 11, 11, 12, 12, 18, 20, 24, 24. This poor performance of the baseline model can be explained by different reasons.

The baseline in the used simulation signal is relatively small, certainly in the region of 2,5 to 4 ppm (see Figure 4.2). This could induce problems in estimat-

Table 4.3: **Average Correlations for *in vivo* quantification** (mean ± Standard Deviation)

		Baseline	
		No Modeling	Spline model
limited prior knowledge	*correlation*	0.91 ± 0.06	0.95 ± 0.07
	residue	1056 ± 712	820 ± 880
all dampings equal	*correlation*	0.85 ± 0.11	0.92 ± 0.07
	residue	1352 ± 1106	908 ± 637

ing the small baseline, and hence introduce errors in the parameter estimation. However, simulations were repeated with a large simulated baseline and similar results were found which rejects this hypothesis. For these experiments, the baseline was simulated by two Lorentzian lineshapes with a broad linewidth. Another possible explanation is that the regularization parameter λ was not optimized by using e.g. Generalized Cross Validation [19]. The FIR filter could also have an influence on the parameter estimation, because it influences the information content of the first data points as was discussed in section 4.2.3. It is clear that baseline modeling using splines has to be optimized and that both the influence of the baseline shape and the FIR filter should be investigated. This will be the subject of further research.

4.3.5 *In vivo* metabolite quantification

To assess the robustness and accuracy of the method on the *in vivo* signals, two parameters were calculated based on the fitted spectrum. The correlation coefficient between the FIR filtered, Fourier transformed original signal and the fitted signal and the norm of the residue was calculated.

The results of the analysis: the average correlations and residues for the four analyses were summarized in Table 4.3.

The correlation measure is in good agreement with the residue measure: when the correlation increases, the residue drops, which suggests that the use of both measures is justified. An increase in correlation and a decrease in residue can be seen when the baseline was modeled during quantification, indicating a better fit. This is to be expected because more variables are introduced to model the spectrum. This is however no guarantee of a more accurate estimate of metabolite parameters.

When all dampings are set to be equal as prior knowledge for the AQSES_{2step} algorithm, the correlation decreases both for the method with and without a baseline model. The prior knowledge that all dampings are equal will prevent dampings to become too large, leading to broad linewidths who partly modeled

baseline components.

When no baseline modeling was used, the correlations between the fit and the original spectrum ranged between 0.71 and 0.98. To illustrate this visually, the spectra corresponding with the highest and lowest correlation are shown in Figure 4.10.

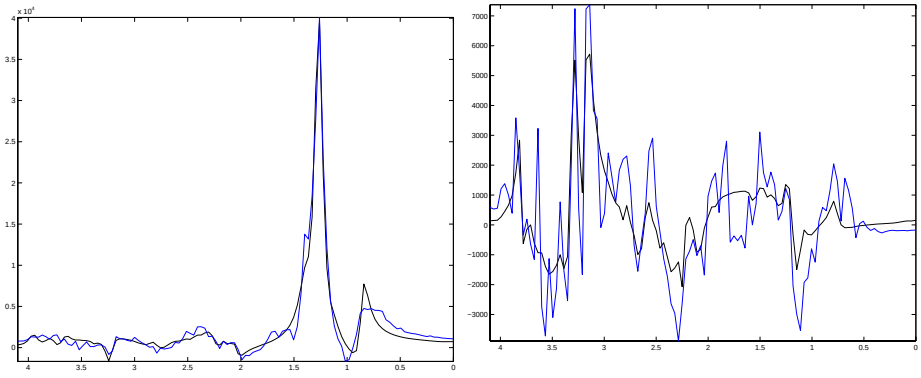

Figure 4.10: Spectrum (thin line) and fit results (thick line) with the highest (left) and the lowest (right) correlation, obtained by AQSES_{2step}.

In Figure 4.11, residues of all 50 spectra are plotted for the fit without baseline and with limited prior knowledge on the dampings. Some peaks have a residue above the average value. The majority of those peaks correspond to spectra coming from metastasis and abscess lesions which are predominantly characterized by a prominent lipid presence in the spectrum. In these spectra, AQSES_{2step} failed to fit the present lipid peaks with the lipid model spectra in the database, which leads to the large values in the residue.

To conclude, an example illustrates the importance of including a baseline in the model function. Figure 4.12 shows the spectrum and fit of a medulloblastoma. It can be seen that the baseline is necessary to obtain a good fit in the 1 to 2.5 ppm region.

These results suggest that a baseline model has to be included in the model function of AQSES.

The inferior performance of the quantification of metabolites in the presence of a baseline, combined with the high correlation between original signal and fit in the *in vivo* cases indicates that the choice of the regularization parameter λ, which was not dealt with in this thesis, is of utmost importance. Being able to provide a fit similar to the original signal (high correlation), does not automatically imply accurate metabolite parameter estimates.

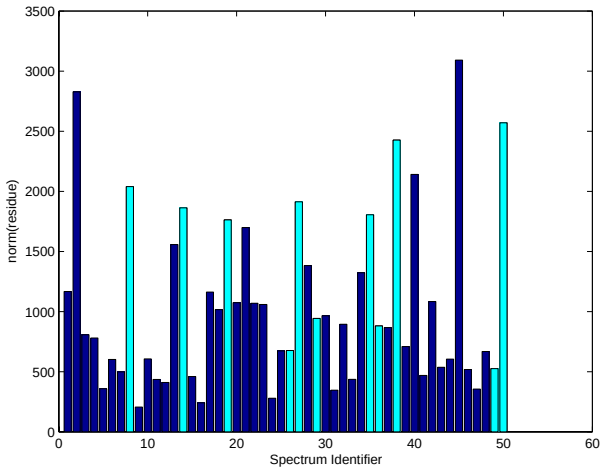

Figure 4.11: Norm of the residues for the 50 spectra. Spectra belonging to metastasis,abscess or Schwanoma lesions are shaded lighter.

4.4 Conclusion

A 2-step time domain approach to short echo time quantification is presented. The 2-step approach increases robustness of quantification by providing frequency starting values based on the fit of 4 landmarks in a first step to a second quantification step. The improved performance of AQSES_{2step} in comparison with AQSES was shown by using Monte Carlo simulations. The baseline was modeled by cubic B splines which were incorporated in the model function. Preliminary results including the spline model suggest that a correct choice of regularization parameter λ is mandatory to increase parameter estimation accuracy.

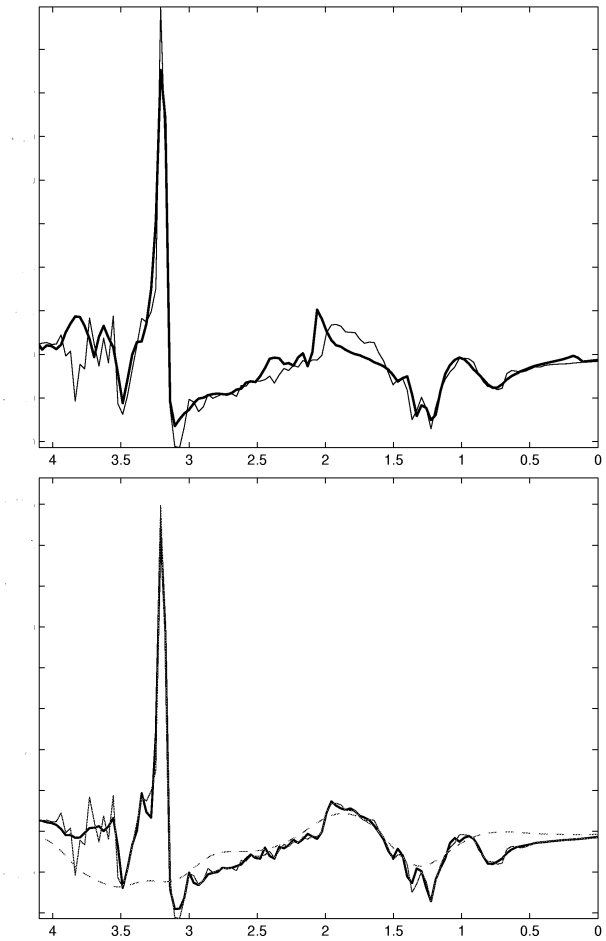

Figure 4.12: Fit of the spectrum of a medulloblastoma without (top) and with (bottom) baseline. Original spectrum (thin line), fitted spectrum (including baseline if modeled) and the estimated baseline (dashed line) are shown.

Chapter 5

Conclusions and Further Research

In this last chapter, findings and conclusions of the presented work are summarized. As research is a never ending story, some directions for further research are outlined.

5.1 Conclusions

This thesis treats different aspects involved in the quantification of long and short echo time spectra. In the following the main conclusions and original contributions are presented.

- The MRS technique was presented as an application of MR. The basic principles of MR and MRS techniques were outlined, together with a description of the acquired MRS spectra. A brief overview was given of the existing methods of preprocessing the data. Different frequency and time domain quantification algorithms are introduced. Time domain methods are usually divided in black-box methods and interactive methods. Interactive methods fit a model function to the data and minimize a cost function. Linear prediction and state-space methods are two variants of the black-box methods which do not involve the minimization of a cost function. The concept of prior knowledge was illustrated and the relevance of MRS in a clinical environment was demonstrated for prostate and brain pathologies.
- A comparison between the quantification accuracy of a Time Domain

Fitting (TDF) method and a Frequency Domain Analysis (FDA) method in the processing of prostate MRSI data was performed. Both TDF and FDA methods had the ability to predict cancerous voxels for an artifact free case study using the ratio of choline+creatine+polyamines to citrate, which is suggested as an effective and robust metric for prostate spectral assessment at 1.5T. Spectral overlap in prostate data acquired at 1.5T was a factor reducing the accuracy of quantification for both of the processing techniques. The TDF method had some problems at modeling the spectra with low SNR. Preliminary results from 3T scanners exhibit higher SNR, and improved spectral resolution with visually separable polyamines. This will likely increase the accuracy of quantification for both methods in the future. The most appropriate choice of the data processing method for any specific application depends on the purpose of the quantification and the type of the spectra analyzed. The use of the TDF method is advised for accurate quantification of the spectra with good SNR, and its ability to separate sharp resonances from the broader peaks. The FDA method is valuable for robust and fast quantification of the spectra, even when there are acquisition-related distortions in the spectra. Both of these processing methodologies are suitable for routine analysis of prostate spectra for clinical and research purposes. A graphical user interface was presented for the display and quantification of prostate MRSI data. Features as a grid shift, solvent filtering and display of metabolite maps after quantification were implemented.

- Multivoxel processing was for the first time applied to MRSI data. It was shown that multivoxel processing increases the accuracy of the estimates of the parameters of a brain MRSI data set. The application on *in vivo* prostate MRSI data showed that multivoxel processing also increases the robustness of parameter estimation. Both improvements are due to the possibility to include prior knowledge between different voxels in the multivoxel processing. However, which parameters benefit from the multivoxel approach depends on the kind of prior knowledge imposed. Imposing prior knowledge on the frequencies between voxels results in more accurate estimates of the frequencies. Only when prior knowledge on the phases and/or dampings is added, also amplitudes benefit from multivoxel quantification. Simulations showed that slight undermodeling of a spectrum has a negative influence on the accuracy of the parameter estimates. On the other hand, slight overmodeling the spectra has no negative influence on the accuracy of amplitude estimates. This indicates that for limited overmodeling, a complete model function for all voxels can be chosen when processing MRSI datasets.

- An improved 2-step time domain approach to short echo time quantification is presented. The 2-step approach increases robustness of quantification by providing frequency starting values based on the fit of 4 landmarks to a second quantification step. The improved performance

of $AQSES_{2step}$ in comparison with AQSES was shown by using Monte Carlo simulations. The baseline was modeled by cubic B splines which were incorporated in the model function. Preliminary results including the spline model suggest that a correct choice of regularization parameter λ is necessary to increase parameter estimation accuracy.

5.2 Further Research

- The study in Chapter 2 investigated the accuracy of the TDF and FDA methods in determining the CCP/C ratio. This ratio is used as a marker for the malignancy of the investigated tissue. In this thesis, a threshold was used to classify spectra. However, in a clinical setting, different types of information sources are consulted and combined in order to classify the spectrum. A visual interpretation of the spectrum is combined with MR images of the prostate, dynamic contrast-enhanced images and with the calculated CCP/C ratio. It should be investigated whether both methods contribute differently in such a more general situation, involving a study on a group of patients.

- Recently, clinical 3 Tesla MR scanners started to emerge in hospitals worldwide. Typically, MRS data acquired at 3T have different characteristics than data acquired at 1.5T. Because of the improved SNR ratio and the improved spectral resolution at 3T, a new comparison between the TDF and the FDA method on 3T data could reveal new differences between both methods.

- From a more clinical point of view, the following question should be answered:"Can MRS of the prostate become a routinely used tool for diagnosing prostate cancer?". Up till now, the results seem to depend on the researcher and the support from an experienced research lab. The answer to this question will not only depend on the evolution of prostate MRS techniques, but also on the evolutions in other diagnostic tools: e.g. TRUS or the significance of PSA levels. Because MRS is a rather expensive technique, the economic aspect should be taken into account as well to answer the question posed above.

- Chapter 3 concluded that slight overmodeling did not have a negative influence on the parameter estimation. However this conclusion can not be extrapolated to the case where the model function has a much higher model order than the spectrum under investigation. Especially for short echo time spectra and high resolution MR spectra, who contain many more peaks than long echo time spectra, this problem can become prevalent. Suggested research comprises the investigation of extensive over- and undermodeling, and even more challenging, the benefits of adding

regularization versus designing an automatic model order selection algorithm.

- The method AQSES$_{2step}$ provides a way of quantifying short echo time spectra by combining a database of measured model spectra and a spline baseline model. The most important research problem is how to tackle the regularization problem, which determines the contribution of the baseline model in the cost function. Other baseline model functions and the influence of the FIR filter should be taken into consideration. Instead of quantifying 4 landmarks in the first step, it should be investigated if an automatic selection procedure could be implemented to increase robustness of AQSES$_{2step}$.

- To transfer AQSES$_{2step}$ from a prototype to clinical practice, two aspects should be elaborated: firstly, a Graphical User Interface is needed to enable fluent user interaction with the algorithm. Such an algorithm is currently under development as part of a general MRS processing toolbox [29]. Secondly, an estimation of error bounds has to be provided, quantifying the uncertainty on the computed parameter estimates. To provide accurate error bound estimates, the baseline model and regularization factor λ has to be taken into account. First results on the error bound estimation can already be found in [92].

Bibliography

[1] http://www.mrui.uab.es/mrui/mruihomepage.html.

[2] E.O. Aboagye and Z.M. Bhujwalla. Malignant transformation alters membrane choline phospholipid metabolism of human mammary epithelial cells. *Cancer Res*, 59(1):80–84, Jan 1999.

[3] A.R.Tate, J.R. Griffiths, I. Martinez-Perez, A. Moreno, I. Barba, M.E. Cabanas, D. Watson, J. Alonso, F. Bartumeus, F. Isamat, I. Ferrer, F. Vila, E. Ferrer, A. Capdevila, and C. Arus. Towards a method for automated classification of ^{1}H MRS spectra from brain tumours. *NMR Biomed*, 11(4-5):177–191, Jun-Aug 1998.

[4] H. Bachelard and Badar-Goffer R. NMR spectroscopy in neurochemistry. *J Neurochem*, 61(2):412–429, Aug 1993.

[5] H. Barkhuysen, R. de Beer, and D. van Ormondt. Improved algorithm for noniterative time-domain model fitting to exponentially damped magnetic resonance signals. *J Magn Reson*, 73:553–557, 1987.

[6] R. Bartha, D.J. Drost, and P.C. Williamson. Factors affecting the quantification of short echo in-vivo ^{1}H MR spectra: prior knowledge, peak elimination, and filtering. *NMR Biomed*, 12(4):205–216, Jun 1999.

[7] F. Bloch, W.W. Hansen, and M. Packard. The nuclear induction experiment. *Phys Rev*, 70:474–485, 1946.

[8] P.A. Bottomly. Spatial localization in NMR spectroscopy in vivo. *Ann N Y Acad Sci*, 508:333–348, 1987.

[9] T.R. Brown, B.M. Kincaid, and K. Ugurbil. NMR chemical shift imaging in three dimensions. *Proc Natl Acad Sci USA*, 1982.

[10] T.R. Brown and R. Stoyanova. NMR spectral quantitation by principal component analysis. II. determination of frequency and phase shifts. *J Magn Reson B*, 112(1):32–43, Jul 1996.

[11] E.B. Cady, A.M. de L. Costello, M.J. Dawson D.T. Delpy, P.L. Hope, E.O. Reynolds, P.S. Tofts, and D.R. Wilkie. Non-invasive investigation of cerebral metabolism in newborn infants by phosphorus nuclear magnetic resonance spectroscopy. *Lancet*, 1:1059–1062, May 1983.

[12] H. Chen, S. Van Huffel, and J. Vandewalle. Improved methods for exponential parameter estimation in the presence of known poles and noise. *IEEE Trans Signal Processing*, 45(5):1390–1393, 1997.

[13] S.C. Chen, T.J. Schaewe, R.S. Teichman, M.I. Miller, S.N. Nadel, and A.S. Greene. Parallel algorithms for maximum-likelihood nuclear magnetic resonance spectroscopy. *J Magn Reson Series A*, 102:16–23, 1993.

[14] P. Christiansen, P.B. Toft, P. Gideon, E.R. Danielsen, P. Ring, and O. Henriksen. MR-visible water content in human brain: a proton MRS study. *Magn reson Imaging*, 12(8):1237–1244, 1994.

[15] F.V. Coakley, H.S. Teh, A. Qayyum, M.G. Swanson, Y. Lu, M. Roach, B. Pickett, K. Shinohara, D.B. Vigneron, and J. Kurhanewicz. Endorectal MR imaging and MR spectroscopic imaging for locally recurrent prostate cancer after external beam radiation therapy: preliminary experience. *Radiology*, 233(2):441–448, Nov 2004.

[16] Y. Coenradie, R. de Beer, D. van Ormondt, S. Cavassila, and H. Ratiney. Background-signal parametrization in in vivo MR spectroscopy. *MAGMA*, 15:369, 2002.

[17] P. Comon and G.H. Golub. Tracking a few extreme singular values and vectors in signal processing. *IEEE Proceedings*, 78:1327–1343, Aug 1990.

[18] L.C. Costello, R.B. Franklin, and P. Narayan. Citrate in the diagnosis of prostate cancer. *The Prostate*, 38:237–245, 1999.

[19] P. Craven and G. Wahba. Smoothing noisy data with spline functions: estimating the correct degree of smoothing by the method of generalized cross-validation. *Numerische Mathematik*, 31:377–403, 1979.

[20] K. Cross. Improved digital filtering technique for solvent suppression. *J Magn Reson*, 101:220–224, 1993.

[21] P.F. Daly, R.C. Lyon, P.J. Faustino, and J.S. Cohen. Phospholipid metabolism in cancer cells monitored by ^{31}P NMR spectroscopy. *J Biol Chem*, 262(31):14875–14878, Nov 1987.

[22] E.R. Danielsen and B.D. Ross. *Magnetic Resonance Spectroscopy Diagnosis of Neurological Diseases*. Marcel Dekker, New York, 1999.

[23] J. Dawson, D.G. Gadian, and D.R. Wilkie. Proceedings: Living muscle studied by ^{31}P nuclear magnetic resonance. *J Physiol*, 258(2):82–83, Jun 1976.

[24] M.J. Dawson, D.G. Gadian, and D.R. Wilkie. Muscular fatigue investigated by phosphorus nuclear magnetic resonance. *Nature*, 274(5674):861–866, Aug 1978.

[25] R. De Beer, A. van den Boogaart, E. Cady, D. Graveron-Demilly, A. Knijn, K.W. Langenberger, J.C. Lindon, A. Ohlhoff, H. Serrai, and M. Wylezinska-Arridge. Absolute metabolite quantification by in vivo NMR spectroscopy: V. multicentre quantitative data analysis trial on the overlapping background problem. *Magn Reson Imaging*, 16(9):1127–1137, Nov 1998.

[26] R. de Beer, A. van den Boogaart, D. van Ormondt, WW. Pijnappel, JA. den Hollander, AJ. Marien, and PR. Luyten. Application of time-domain fitting in the quantification of in vivo ^{1}H spectroscopic imaging data sets. *NMR Biomed*, 5(4):171–178, Jul-Aug 1992.

[27] AA. de Graaf and WM. Bovee. Improved quantification of in vivo ^{1}H NMR spectra by optimization of signal acquisition and processing and by incorporation of prior knowledge into the spectral fitting. *Magn Reson Med*, 15(2):305–319, Aug 1990.

[28] A.A. de Graaf, J.E. van Dijk, and W.M. Bovee. QUALITY: quantification improvement by converting lineshapes to the lorentzian type. *Magn Reson Med*, 13(3):343–357, Mar 1990.

[29] B. De Neuter, L. Vanhamme, P. Lemmerling, and S. Van Huffel. A JAVA-based framework for processing and displaying short echo time magnetic resonance spectroscopy signals. Internal Report, SCD/ESAT, Nov 2004.

[30] A. Devos, L. Lukas, J.A. Suykens, L. Vanhamme, A.R. Tate, F.A. Howe, C. Majos, A. Moreno-Torres, M. van der Graaf, C. Arus, and S. Van Huffel. Classification of brain tumours using short echo time ^{1}H MR spectra. *J Magn Reson*, 170(1):164–175, Sep 2004.

[31] J.H. Duijn, G.B. Matson, A.A. Maudsley, J.W. Hugg, and M.W. Weiner. Human brain infarction: proton MR spectroscopy. *Radiology*, 183(3):711–718, Jun 1992.

[32] P.H.C. Eilers and B.D. Marx. Flexible smoothing with B-splines and penalties. *Statist Sci*, 11(2):89–121, 1996.

[33] C. Elster, A. Link, F. Schubert, F. Seifert, M. Walzel, and H. Rinneberg. Quantitative MRS: comparison of time domain and time domain frequency domain methods using a novel test procedure. *Magn Reson Imaging*, 18(5):597–606, Jun 2000.

[34] C.L. Florian, N.E. Preece, K.K. Bhakoo, S.R. Williams, and M. Noble. Characteristic metabolic profiles revealed by ^{1}H NMR spectroscopy for

three types of human brain and nervous system tumours. *NMR Biomed*, 8(6):253–264, Sep 1995.

[35] J. Frahm, K.D. Merboldt, and W. Hanicke. Localized proton spectroscopy using stimulated echoes. *J Magn Res*, 72:502–508, 1987.

[36] G.H. Golub and V. Pereyra. The differentiation of pseudo-inverses and nonlinear least squares problems whose variables separate. *SIAM J. Numer. Anal.*, 10(2):413–432, 1973.

[37] D. Graveron-Demilly, A. Diop, A. Briguet, and B. Fenet. Product-operator algebra for strongly coupled spin systems. *J Magn Reson ser A*, 101(3):233–239, Feb 2002.

[38] J.-P. Grivet. Accurate numerical approximation to the Gauss-Lorentz lineshape. *J Magn Reson*, 125(1):102–106, 1997.

[39] R. Gruetter, I. Magnusson, D.L. Rothman, M.J. Avison, R.G. Shulman, and G.I. Shulman. Validation of ^{13}C NMR measurements of liver glycogen in vivo. *Magn Reson Med*, 31(6):583–588, Jun 1994.

[40] T. Hammen, H. Stefan, I. Schafer, W. Huk, and B. Tomandl. ^{1}H-MR spectroscopy: a promising method in distinguishing subgroups in temporal lobe epilepsy? *J Neurol Sci*, 215(1-2):21–25, Nov 2003.

[41] R.H. Hashemi, W.G. Bradley, and C.J. Lisanti. *MRI: The Basics*. Lippincott Williams & Wilkins, 2nd edition edition, 2003.

[42] A. Heerschap, G.J. Jager, M. van der Graaf, J.O. Barentsz, J.J. de la Rosette, G.O. Oosterhof, E.T. Ruijter, and S.H. Ruijs. In vivo proton MR spectroscopy reveals altered metabolite content in malignant prostate tissue. *Anticancer Res*, 17(3A):1455–1460, May-Jun 1997.

[43] L. Hofmann, J. Slotboom, B. Jung, P. Maloca, C. Boesch, and R. Kreis. Quantitative ^{1}H-magnetic resonance spectroscopy of human brain: Influence of composition and parameterization of the basis set in linear combination model-fitting. *Magn Reson Med*, 48(3):440–453, Sep 2002.

[44] C. Huegen. De invloed van voorkennis op de cramer-rao ondergrens. Master's thesis, Technische Universiteit Delft, 1993.

[45] R.A. Iles, I.J. Cox, L.M. Dubowitz, F. Cowan, and D.J. Bryant. ^{31}P magnetic resonance spectroscopy of the human paediatric liver. *NMR Biomed*, 3(2):90–94, Apr 1990.

[46] J.A. Jung, F.V. Coakley, D.B. Vigneron, M.G. Swanson, A. Qayyum, V. Weinberg, K.D. Jones, P.R. Carroll, and J. Kurhanewicz. Prostate depiction at endorectal MR spectroscopic imaging: investigation of a standardized evaluation system. *Radiology*, 233(3):701–708, Dec 2004.

[47] M. Kanowski, J. Kaufman, J. Braun, J. Bernarding, and C. Tempelmann. Quantitation of simulated short echo time ^{1}H human brain spectra by LCModel and AMARES. *Magn Reson Med*, 51(5):904–912, May 2004.

[48] M.N. Kassem and R. Bartha. Quantitative proton short-echo-time LASER spectroscopy of normal human white matter and hippocampus at 4 Tesla incorporating macromolecule subtraction. *Magn Reson Med*, 49(5):918–927, May 2003.

[49] U. Klose. In vivo proton spectroscopy in presence of eddy currents. *Magn Reson Med*, 14(1):26–30, Apr 1990.

[50] J. Knight-Scott. Application of multiple inversion recovery for suppression of macromolecule resonances in short echo time ^{1}H NMR spectroscopy of human brain. *J Magn Reson*, 140(1):228–234, Sep 1999.

[51] P. Koehl. Linear prediction spectral analysis of NMR data. *Prog in NMR Spectrosc*, 34:257–299, 1999.

[52] H. Kugel, W. Heindel, R.I. Ernestus, J. Bunke, R. du Mesnil, and G. Friedmann. Human brain tumors: spectral patterns detected with localized ^{1}H MR spectroscopy. *Radiology*, 183(3):701–709, Jun 1992.

[53] S.Y. Kung, K.S. Arun, and D.V. Bhaskar Rao. State-space and singular-value decomposition-based approximation methods for the harmonic retrieval problem. *J Opt Soc Am*, 73(12):1799–1811, 1983.

[54] J. Kurhanewicz, M.G. Swanson, S.J. Nelson, and D.B. Vigneron. Combined magnetic resonance imaging and spectroscopic imaging approach to molecular imaging of prostate cancer. *J Magn Reson Imaging*, 16(4):451–463, Oct 2002.

[55] J. Kurhanewicz, A. Thomas, P. Jajodia, M.W. Weiner, T.L. James, D.B. Vigneron, and P. Narayan. ^{31}P spectroscopy of the human prostate gland in vivo using a transrectal probe. *Magn Reson Med*, 22(2):404–413, Dec 1991.

[56] J. Kurhanewicz, D.B. Vigneron, S.J. Nelson, H. Hricak, J.M. MacDonald, B. Konety, and P. Narayan. Citrate as an in vivo marker to discriminate prostate cancer from benign prostatic hyperplasia and normal prostate peripheral zone: detection via localized proton spectroscopy. *Urology*, 45(3):459–466, Mar 1995.

[57] H. Lanfermann, H. Kugel, W. Heindel, K. Herholz, W.D. Heiss, and K. Lackner. Metabolic changes in acute and subacute cerebral infarctions: findings at proton MR spectroscopic imaging. *Radiology*, 196(1):203–210, Jul 1995.

[58] P.C. Lauterbur. Image formation by induced local interactions: examples employing nuclear magnetic resonance. *Nature*, 242:190–191, 1973.

[59] P. Lemmerling, L. Vanhamme, R. in't Zandt, S. Van Huffel, and P. Van Hecke. Time-domain quantification of short echo time in vivo proton MRS. In *Proceedings of the 19th Meeting of the ESMRMB, Cannes*. ESMRMB, 2002.

[60] A. Lin, S. Biumi, and A.N. Mamelak. Efficacy of proton magnetic resonance spectroscopy in clinical decision making for patients with suspected malignant brain tumors. *J Neurooncol*, 45(1):69–81, 1999.

[61] G.P. Liney, L.W. Turnbull, M. Lowry, L.S. Turnbull, A.J. Knowles, and A. Horsman. In vivo quantification of citrate concentration and water T2 relaxation time of the pathologic prostate gland using ^{1}H MRS and MRI. *Magn Reson Imaging*, 15(10):1177–1186, 1997.

[62] L. Lukas, A. Devos, J.A. Suykens, L. Vanhamme, F.A. Howe, C. Majos, A. Moreno-Torres, M. van der Graaf, A.R. Tate, C. Arus, and S. Van Huffel. Brain tumor classification based on long echo proton MRS signals. *Artif Intell Med*, 31(1):73–89, May 2004.

[63] P. Mansfield and A.A. Maudsley. Planar and line-scan spin imaging by NMR. *Proc. XIXth Congress Amperen, Heidelberg*, pages 247–252, 1976.

[64] D.J. Manton, M. Lowry, S.J. Blackband, and A. Horsman. Determination of proton metabolite concentrations and relaxation parameters in normal human brain and intracranial tumours. *NMR Biomed*, 8(3):104–112, May 1995.

[65] D. Marion, M. Ikura, and A. Bax. Improved solvent suppression to one- and two-dimensional NMR spectra by convolution of time-domain data. *J Magn Reson*, 84:425–430, 1989.

[66] A.A. Maudsley, A.K. Hilal, W.H. Perman, and H.E. Simon. Spatially resolved high-resolution spectroscopy by 'four dimensional' NMR. *J Magn Reson*, 51:147–152, 1983.

[67] M.I. Miller and A.S. Greene. Maximum-likelihood estimation for nuclear magnetic resonance spectroscopy. *J Magn Reson*, 83:525–548, 1989.

[68] G.L. Millhauser, A.A. Carter, D.J. Schneider, J.H. Freed, and R.E. Oswald. Rapid singular value decomposition for time-domain analysis of magnetic resonance signals by use of the lanczos algorithm. *J Magn Reson*, 82:150–155, 1989.

[69] R.V. Mulkern and J.L. Bowers. Calculating spectral modulations of AB systems during PRESS acquisitions. *Magn Reson Med*, 30(4):518, Oct 1993.

[70] P.G. Mullins, L. Rowland, J. Bustillo, E.J. Bedrick, J. Lauriello, and W.M. Brooks. Reproducibility of ^{1}H-MRS measurements in schizophrenic patients. *Magn Reson Med*, 50(4):704–707, Oct 2003.

[71] S.J. Nelson. Analysis of volume MRI and MR spectroscopic imaging data for the evaluation of patients with brain tumors. *Magn Reson Med*, 46(2):228–239, Aug 2001.

[72] S. Neubauer. High-energy phosphate metabolism in normal, hypertrophied and failing human myocardium. *Heart Failure Rev*, 4(3):269–280, Oct 1999.

[73] M.R. Osborne. *Numerical methods for non-linear optimization*, chapter Some aspects of non-linear least squares calculations. Academic Press,London, 1972.

[74] K. Overloop, P. Van Hecke, F. Vanstapel, H. Chen, S. Van Huffel, A. Knijn, and D. van Ormondt. Evaluation of signal processing methods for the quantification of a multi-exponential signal: the glycogen ^{13}C-1 NMR signal. *NMR Biomed*, 9(7):315–321, Oct 1996.

[75] B. Pickett, J. Kurhanewicz, F. Coakley, K. Shinohara, B. Fein, and M. Roach. Use of MRI and spectroscopy in evaluation of external beam radiotherapy for prostate cancer. *Int J Radiat Oncol Biol Phys*, 60(4):1047–1055, Nov 2004.

[76] H. Poptani, J. Kaartinen, R.K. Gupta, M. Niemitz, Y. Hiltunen, and R.A. Kauppinen. Diagnostic assessment of brain tumours and non-neoplastic brain disorders in vivo using proton nuclear magnetic resonance spectroscopy and artificial neural networks. *J Cancer Res Clin Oncol*, 125(6):343–349, 1999.

[77] J.J. Potwarka, D.J. Drost, and P.C. Williamson. Quantifying ^{1}H decoupled in vivo ^{31}P brain spectra. *NMR Biomed*, 12(1):8–14, Feb 1999.

[78] M.C. Preul, Z. Caramanos, R. Leblanc, J.G. Villemure, and D.L. Arnold. Using pattern analysis of in vivo proton MRSI data to improve the diagnosis and surgical management of patients with brain tumors. *NMR Biomed*, 11(4-5):192–200, Jun-Aug 1998.

[79] S.W. Provencher. Estimation of metabolite concentrations from localized in vivo proton NMR spectra. *Magn Reson Med*, 30(6):672–679, Dec 1993.

[80] S.W. Provencher. Automatic quantitation of localized in vivo ^{1}H spectra with LCModel. *NMR Biomed*, 14(4):260–264, Jun 2001.

[81] E.M. Purcell, H.C. Torrey, and R.V. Pound. Resonance absorption by nuclear magnetic moments in a solid. *Phys Rev*, 69:37–38, 1946.

[82] A. Quyyum, F.V. Coakley, Y. Lu, J.D. Olpin, L. Wu, B.M. Yeh, P.R. Carroll, and J. Kurhanewicz. Organ-confined prostate cancer: effect of prior transrectal biopsy on endorectal MRI and MR spectroscopic imaging. *AJR Am J Roentgenol*, 183(4):1079–1083, Oct 2004.

[83] H. Ratiney, Y. Coenradie, S. Cavassila, D. van Ormondt, and D. Graveron-Demilly. Time-domain quantitation of ^{1}H short echo-time signals: background accommodation. *MAGMA*, 16(6):284–296, May 2004.

[84] B.R. Rosen, V.J. Wedeen, and T.J. Brady. Selective saturation NMR imaging. *J Comput Assist Tomogr*, 8(5):813–818, Oct 1984.

[85] B.D. Ross, G.K. Radda, D.G. Gadian, G. Rocker, M. Esiri, and J. Falconer-Smith. Examination of a case of suspected McArdle's syndrome by ^{31}P nuclear magnetic resonance. *New Eng J Med*, 304:1338–1342, 1981.

[86] F. Schick, H. Bongers, S. Kurz, W.I. Jung, M. Pfeffer, and O. Lutz. Localized proton MR spectroscopy of citrate in vitro and of the human prostate in vivo at 1.5 T. *Magn Reson Med*, 29(1):38–43, Jan 1993.

[87] M.L. Schiebler, K.K. Miyamoto, M. White, S.J. Maygarden, and J.L. Mohler. In vitro high resolution ^{1}H-spectroscopy of the human prostate: benign prostatic hyperplasia, normal peripheral zone and adenocarcinoma. *Magn Reson Med*, 29(3):285–291, Mar 1993.

[88] M.L. Schiebler, J.E. Tomaszewski, M. Bezzi, H.M. Pollack, H.Y. Kressel, and E.K. Cohen. Prostatic carcinoma and benign prostatic hyperplasia: correlation of high-resolution MR and histopathologic findings. *Radiology*, 172(1):131–137, Jul 1989.

[89] H.P. Schlemmer and S. Corvin. Methods for volume assessment of prostate cancer. *Eur Radiol*, 14(4):597–606, Apr 2004.

[90] U. Seeger, I. Mader, T. Nagele, W. Grodd, O. Lutz, and U. Klose. Reliable detection of macromolecules in single-volume ^{1}H NMR spectra of the human brain. *Magn Reson Med*, 45(6):948–954, Jun 2001.

[91] A. Shukla-Dave, H. Hricak, S.C. Eberhardt, S. Olgac, M. Muruganandham, P.T. Scardino, V.E. Reuter, J.A. Koutcher, and K.L. Zakian. Chronic prostatitis: MR imaging and ^{1}H MR spectroscopic imaging findings–initial observations. *Radiology*, 231(3):717–724, Jun 2004.

[92] D.M. Sima and S. Van Huffel. Regularized semiparametric model identification with application to NMR signal quantification with unknown macromolecular baseline. Internal Report TR-04-229, SCD/ESAT, Submitted to *Journal of the Royal Statistical Society: Series B*, Nov 2004.

[93] J. Slotboom, C. Boesch, and R. Kreis. Versatile frequency domain fitting using time domain models and prior knowledge. *Magn Reson Med*, 39(6):899–911, Jun 1998.

[94] S.A. Smith, T.O. Levante, B.H. Meier, and R.R. Ernst. Computer simulations in magnetic resonance. an object-oriented programming approach. *J Magn Reson Ser A*, 106(1):75–105, Jan 1994.

[95] B.J. Soher, K. Young, V. Govindaraju, and A.A. Maudsley. Automated spectral analysis III: application to in vivo proton MR spectroscopy and spectroscopic imaging. *Magn Reson Med*, 40(6):822–831, Dec 1998.

[96] B.J. Soher, K. Young, and A.A. Maudsley. Representation of strong baseline contributions in ^{1}H MR spectra. *Magn Reson Med*, 45(6):966–972, Jun 2001.

[97] J.A. Stanley and J.W. Pettegrew. Postprocessing method to segregate and quantify the broad components underlying the phosphodiester spectral region of in vivo ^{31}P brain spectra. *Magn Reson Med*, 45(3):390–396, Mar 2001.

[98] J. Star-Lack, S.J. Nelson, J. Kurhanewicz, L.R. Huang, and D.B. Vigneron. Improved water and lipid suppression for 3D PRESS CSI using RF band selective inversion with gradient dephasing (BASING). *Magn Reson Med*, 38(2):311–321, Aug 1997.

[99] P. Stoica and R. Moses. *Introduction to spectral analysis*. Prentice Hall, Uppers Saddle River, New Jersey, 1997.

[100] T. Sundin, L. Vanhamme, P. Van Hecke, I. Dologlou, and S. Van Huffel. Accurate quantification of ^{1}H spectra: from finite impulse response filter design for solvent suppression to parameter estimation. *J Magn Reson*, 139(2):189–204, Aug 1999.

[101] Thomas Sundin. *Spectral Analysis and Magnetic Resonance Spectroscopy*. PhD thesis, Uppsala University, 2001.

[102] R.B. Thompson and P.S. Allen. Sources of variability in the response of coupled spins to the press sequence and their potential impact on metabolite quantification. *Magn Reson Med*, 41:1162–1169, 1999.

[103] A. van den Boogaart, M. Ala-Korpela, J. Jokisaari, and J.R. Griffiths. Time and frequency domain analysis of NMR data compared: an application to 1D ^{1}H spectra of lipoproteins. *Magn Reson Med*, 31(4):347–358, Apr 1994.

[104] A. van den Boogaart, F.A. Howe, L.M. Rodrigues, M. Stubbs, and J.R. Griffiths. In vivo ^{31}P MRS: absolute concentrations, signal-to-noise and prior knowledge. *NMR Biomed*, 8(2):87–93, Apr 1995.

[105] A. van den Boogaart, D. van Ormondt, W. Pijnappel, R. de Beer, and M. Ala-Korpela. Removal of the water resonance from ^{1}P magnetic resonance spectra. *J Magn Reson*, 1:175–195, 1991.

[106] M. van der Graaf and A. Heerschap. Effect of cation binding on the proton chemical shifts and the spin-spin coupling constant of citrate. *J Magn Reson*, 112(1):58–62, Jul 1996.

[107] M. van der Graaf, G.J. Jager, and A. Heerschap. Removal of the outer lines of the citrate multiplet in proton magnetic resonance spectra of the prostatic gland by accurate timing of a point-resolved spectroscopy pulse sequence. *MAGMA*, 5(1):65–69, Mar 1997.

[108] M. van der Graaf, G.J. Jager, and A. Heerschap. Removal of the outer lines of the citrate multiplet in proton magnetic resonance spectra of the prostatic gland by accurate timing of a point-resolved spectroscopy pulse sequence. *MAGMA*, 5(1):65–69, Mar 1997.

[109] M. van der Graaf, H.J. van den Boogert, G.J. Jager, J.O. Barentsz, and A. Heerschap. Human prostate: multisection proton MR spectroscopic imaging with a single spin-echo sequence–preliminary experience. *Radiology*, 213(3):919–925, Dec 1999.

[110] J.W. van der Veen, R. de Beer, P.R. Luyten, and D. van Ormondt. Accurate quantification of in vivo ^{31}P NMR signals using the variable projection method and prior knowledge. *Magn Reson Med*, 6(1):92–98, Jan 1988.

[111] S. Van Huffel, H. Chen, C. Decanniere, and P. Van Hecke. Algorithm for time-domain NMR data fitting based on total least squares. *J Magn Reson Series A*, 110:228–237, 1994.

[112] S. Van Huffel, Y. Wang, L. Vanhamme, and P. Van Hecke. Automatic frequency alignment and quantitation of single resonances in multiple magnetic resonance spectra via complex principal component analysis. *J Magn Reson*, 158(1-2):1–14, Sept-Oct 2002.

[113] L. Vanhamme. *Advanced time-domain methods for nuclear magnetic resonance spectroscopy data analysis*. PhD thesis, Katholieke Universiteit Leuven, November 1999.

[114] L. Vanhamme, R.D. Fierro, S. Van Huffel, and R. de Beer. Fast removal of residual water in proton spectra. *J Magn Reson*, 132(2):197–203, Jun 1998.

[115] L. Vanhamme, A. van den Boogaart, and S. Van Huffel. Improved method for accurate and efficient quantification of MRS data with use of prior knowledge. *J Magn Reson*, 129(1):35–43, Nov 1997.

[116] L. Vanhamme and S. Van Huffel. Multichannel quantification of biomedical magnetic resonance spectroscopic signals. In *Conference on Advanced Signal Processing: Algorithms, Architectures and Implementations VIII, San Diego, CA*, pages 237–248. SPIE, Jul 1998.

[117] L. Vanhamme, S. Van Huffel, P. Van Hecke, and D. van Ormondt. Time-domain quantification of series of biomedical magnetic resonance spectroscopy signals. *J Magn Reson*, 140(1):120–130, Sep 1999.

[118] G. Wahba. *Spline Models for Observational Data*. Soc for Industrial & Applied Math, 1990.

[119] A.E. Wefer, H. Hricak, D.B. Vigneron, F.V. Coakley, Y. Lu, J. Wefer, U. Mueller-Lise, P.R. Carroll, and J. Kurhanewicz. Sextant localization of prostate cancer: comparison of sextant biopsy, magnetic resonance imaging and magnetic resonance spectroscopic imaging with step section histology. *J Urol*, 164(2):400–404, Aug 2000.

[120] E. Weiland. *Automatische Quantifizierung von Metabolitenkonzentrationen in in vivo Spektren*. PhD thesis, Universität Bremen, 2004.

[121] A.H. Wilman and P.S. Allen. The response of the strongly coupled AB system of citrate to typical ^{1}H MRS localization sequences. *J Magn Reson B*, 107(1):25–33, Apr 1995.

[122] H. Witjes, WJ. Melssen, HJ. in 't Zandt, M. van der Graaf, A. Heerschap, and LM. Buydens. Automatic correction for phase shifts, frequency shifts, and lineshape distortions across a series of single resonance lines in large spectral data sets. *J Magn Reson*, 144(1):35–44, May 2000.

[123] T. Yabe, K. Mitsunami, T. Inubushi, and M. Kinoshita. Quantitative measurements of cardiac phosphorus metabolites in coronary artery disease by ^{31}P magnetic resonance spectroscopy. *Circulation*, 92(1):15–23, Jul 1995.

[124] K. Young, V. Govindaraju, B.J. Soher, and A.A. Maudsley. Automated spectral analysis I: formation of a priori information by spectral simulation. *Magn Reson Med*, 40:812–815, 1998.

[125] K. Young, B.J. Soher, and A.A. Maudsley. Automated spectral analysis II: application of wavelet shrinkage for characterization of non-parameterized signals. *Magn Reson Med*, 40(6):816–821, Dec 1998.

[126] D.P. Younkin, M. Delivora-Papadopoulos, J.C. Leonard, V.H. Eleff, J.S.Jr Leigh, and B. Chance. Unique aspects of human newborn cerebral metabolism evaluated with phosphorus nuclear magnetic resonance spectroscopy. *Ann Neurol*, 16(5):581–586, 1984.

List of publications

Publications in International Journals

- P. Pels, E. Ozturk, L. Vanhamme, S. Van Huffel and S.J. Nelson, "Model-based time-domain fitting versus frequency-domain analysis applied to prostate MRSI", Internal Report 04-180, ESAT-SCD, Katholieke Universiteit Leuven, Leuven, Belgium, 2004.*(Submitted to NMR in Biomedicine)*

Publications on International Conferences
(fully refereed)

- B. De Neuter, P. Pels, L. Vanhamme, S. Van Huffel and P. Van Hecke, "A JAVA-based graphical user interface for the displaying and processing of Magnetic Resonance Spectroscopy data of the prostate", *IFMBE Proceedings*, (Proceedings of the Second European Medical & Biological Engineering Conference), Vol. 3, p. 384-385, Vienna, Austria, December 4-8, 2002.

- P. Pels, L. Vanhamme, P. Van Hecke and S. Van Huffel, "Influence of multivoxel processing and model order for time-domain MRSI quantitation", *Proceedings of MTNS 2004*, (Proceedings Sixteenth International Symposium on: Mathematical Theory of Networks and Systems), (CD-ROM paper No. 485, ISBN 90-5682-517-8), Leuven, Belgium, July 5-9, 2004.

Presentations on (Inter)National Conferences
(refereed,only abstracts)

- L. Vanhamme, P. Pels, P. Van Hecke and S. Van Huffel, "Automated time-domain quantitation of MRSI datasets using spatial information", *ESMRMB 2002*, (19th Annual Scientific Meeting of European Society of

Magnetic Resonance in Medicine and Biology), Cannes, France, August 22-25, 2002.

- P. Pels, E. Ozturk, L. Vanhamme, S. Van Huffel and S.J. Nelson, "Model-based time-domain fitting versus frequency-domain analysis applied to prostate MRSI", *ESMRMB 2004*, (21th Annual Scientific Meeting of European Society of Magnetic Resonance in Medicine and Biology), Copenhagen, Denmark, September 9-12, 2004.
- P. Pels, L. Vanhamme, P. Van Hecke and S. Van Huffel, "Automated time-domain quantitation of MRSI datasets using spatial information", *National Day on Biomedical Engineering*, (Meeting of the Belgian Society for Medical and Biological Engineering and Computing), Brussels, Belgium, October 18, 2002.

Other presentations
(only abstracts)

- P. Pels and L. Vanhamme, "Parameter estimation of Prostate CSI data", Lecture given at the Magnetic Resonance Science Center, University of California, San Francisco (UCSF), CA, U.S.A., May, 2002.
- P. Pels and E. Ozturk, "Comparison of MR Spectroscopy Quantitation Using Time Domain Fitting and Frequency Domain Analysis for Prostate Cancer", Lecture given at the Magnetic Resonance Science Center, University of California, San Francisco (UCSF), CA, U.S.A., April, 2004.
- P. Pels, L. Vanhamme, P. Van Hecke and S. Van Huffel, "Influence of multivoxel processing and model order for time-domain MRSI quantitation", *MTNS 2004*, Leuven, Belgium, July 5-9, 2004.
- P. Pels, B. De Neuter, L. Vanhamme, S. Van Huffel and P. Van Hecke, "A JAVA-based graphical user interface for the displaying and processing of Magnetic Resonance Spectroscopy data of the prostate", presented at the Study Day of the IUAP network, Louvain-la-neuve, Belgium, May, 2002.
- B. De Neuter, A. Devos, T. Laudadio, P. Lemmerling, P. Pels, L. Vanhamme and S. Van Huffel, "NMR Data Processing", presented at the Study Day of the IUAP network, Gent, Belgium, June, 2004.

Internal Reports

- P. Pels, L. Vanhamme, S. Van Huffel and P. Van Hecke, "Time-domain MRSI quantitation combining multivoxel processing, FIR based solvent

suppression and prior knowledge", Internal Report 03-164, ESAT-SCD, Katholieke Universiteit Leuven, Leuven, Belgium, 2003.

Curriculum Vitae

Pieter Pels was born in Eeklo on April 16, 1978. He received the M.Sc. degree in Physics from the Katholieke Universiteit Leuven in 2000. His main topic was Acoustics and his Master's thesis under supervision of prof. W. Lauriks was devoted to '*Engine Sound: Evaluation and Modification*'. This work was realized in collaboration with the KUL spin-off LMS International.

In August 2000 he started working as a researcher at the Electrical Engineering Department ESAT in the Lab of Signals, Identification, System Theory and Automation (SCD/SISTA) at the Katholieke Universiteit Leuven. During this period, he was supported by a grant of the Instituut voor de aanmoediging van Innovatie door Wetenschap en Technologie in Vlaanderen (IWT). During his research, Pieter Pels spent two months at the Magnetic Resonance Science Center (MRSC) of the University of California, San Francisco (UCSF) as part of a collaboration.